

AL A09, 723

① LEVEL II
SC

. ITEM A002

ATAC AUTOCUER MODELING ANALYSIS

JANUARY 1981

DTIC
ELECTE
S D
APR 14 1981
B

AEROSPACE GROUPS ✓

HUGHES

HUGHES AIRCRAFT COMPANY
CULVER CITY, CALIFORNIA

FILE COPY

DISTRIBUTION STATEMENT A

Approved for public release;
Distribution Unlimited

81 4 14 .41

UNCLASSIFIED

SECURITY CLASSIFICATION OF THIS PAGE (When Data Entered)

REPORT DOCUMENTATION PAGE		READ INSTRUCTIONS BEFORE COMPLETING FORM
1. REPORT NUMBER HAC -FR-80-70-1325 ✓	2. GOVT ACCESSION NO. AD-HC 77 733	3. RECIPIENT'S CATALOG NUMBER
4. TITLE (and Subtitle) ATAC AUTOCUER MODELING ANALYSIS - 1	5. TYPE OF REPORT & PERIOD COVERED FINAL REPT.	6. PERFORMING ORG. REPORT NUMBER
7. AUTHOR(s) R. L. FREY, C. D. NEALY, L. M. RUBIN, B. M. WILKOK	8. CONTRACT (or GRANT) NUMBER(s) DAAK70-77-C-0232	9. PROGRAM ELEMENT, PROJECT, TASK AREA & WORK UNIT NUMBERS
10. CONTROLLING OFFICE NAME AND ADDRESS U. S. ARMY NIGHT VISION AND ELECTRO-OPTICS LABORATORY FORT BELVOIR, VIRGINIA 22060	11. REPORT DATE JANUARY 1981	12. NUMBER OF PAGES 127
13. MONITORING AGENCY NAME & ADDRESS (if different from Controlling Office) 12 130	14. SECURITY CLASS. (of this report) UNCLASSIFIED	15. DECLASSIFICATION/DOWNGRADING SCHEDULE
16. DISTRIBUTION STATEMENT (of this Report) DISTRIBUTION UNLIMITED DISTRIBUTION STATEMENT A Approved for public release; Distribution Unlimited		
17. DISTRIBUTION STATEMENT (of the abstract entered in Block 20, if different from Report)		
18. SUPPLEMENTARY NOTES		
19. KEY WORDS (Continue on reverse side if necessary and identify by block number) IMAGE PROCESSING, FLIR AUTOCUER ANALYSIS, SEGMENTATION PERFORMANCE, TARGET SHAPE DESCRIPTION, DETECTION, AND ESTIMATION.		
20. ABSTRACT (Continue on reverse side if necessary and identify by block number) AN ANALYTIC MODELING APPROACH FOR IMAGE PROCESSING ALGORITHMS HAS BEEN DEVELOPED AND APPLIED TO THE COMPLEX OBJECT SEGMENTATION OPERATION USED FOR TARGET CLASSIFICATION/RECOGNITION IN FLIR IMAGES.		

DD FORM 1 JAN 73 1473

EDITION OF 1 NOV 65 IS OBSOLETE

UNCLASSIFIED

SECURITY CLASSIFICATION OF THIS PAGE (When Data Entered)

412 85

10

ATAC AUTOCUER MODELING ANALYSIS

January 1981

CDRL ITEM A002
ATAC ADD-ON FINAL REPORT

R. L. Frey
C. D. Nealy
L. M. Rubin
R. M. Wilcox

Hughes Aircraft Company • Culver City, California

CONTENTS

1.0	INTRODUCTION	1-1
2.0	IMAGE PROCESSING MODELING PHILOSOPHY	2-1
3.0	BASIC ANALYTIC TECHNIQUES	3-1
3.1	Estimation Theory	3-2
3.2	Probability of Anomaly	3-5
4.0	TARGET MODELS	4-1
4.1	Approaches Examined	4-1
	2-D Legendre Polynomial Representation	4-1
	Composite Rectangle Model	4-2
	Composite Equal-Angled Triangular Model	4-3
	General Polygonal Model	4-4
4.2	Significance of These Results	4-7
5.0	CLUTTER MODELING	5-1
5.1	Clutter Model I	5-1
5.2	Clutter Model II	5-5
5.3	Effects of Clutter on Target Segmentation	5-9
5.4	Verification of Probability of Anomaly Bounds	5-10
5.5	Textured Clutter	5-11
6.0	SENSOR MODEL	6-1
7.0	ANALYSIS OF ATAC SEGMENTATION	7-1
7.1	Introduction	7-1
7.2	Edge Analysis	7-4
7.3	Interior Points	7-15
	Case 1 - Point on the Outer Boundary of Object	7-17
	Case 2 - Point Outside the Outer Boundary but Closer than m Pixels to the Object	7-17

CONTENTS (Continued)

	Case 3 - Point Far Removed from Outer Boundary	7-19
	Intensity Assignment	7-20
7.4	Summary and Conclusions	7-23
8.0	CONCLUSIONS AND RECOMMENDATIONS	8-i
APPENDICES		
	APPENDIX A - NEW APPROACH TO FLIR SEGMENTATION.	A-1
	APPENDIX B - SOBEL OPERATOR PROBABILITY DENSITY.	B-1
	APPENDIX C - AVERAGE VALUE AND VARIANCE OF SOBEL EDGE OPERATOR	C-1
	APPENDIX D - PROBABILITY OF NON-DETECTION FOR A PARALLEL-TO-THE BOUNDARY PAIR.	D-1
	APPENDIX E - PROBABILITY OF PAIR GAP PERPENDICULAR TO BOUNDARY.	E-1
	APPENDIX F - NEXT-NEAREST-NEIGHBOR CORRELATION	F-1
	APPENDIX G - DERIVATION OF FISHER INFORMATION MATRIX FOR GENERAL POLYGON	G-1
	APPENDIX H - EFFECT OF CLUTTER ON TARGET SEGMENTATION PROBABILITY OF ANOMALY.	H-1
	REFERENCES.	R-1

Accession For	
NTIS GRA&I	<input checked="checked" type="checkbox"/>
DTIC TAB	<input type="checkbox"/>
Unannounced	<input type="checkbox"/>
Justification	
By _____	
Distribution/	
Availability Codes	
Dist	Avail and/or Special
A	

S DTIC ELECTE D

APR 14 1981

B

LIST OF ILLUSTRATIONS

Figure		Page
2-1	General Model Diagram	2-2
4-1	Reconstruction Using Legendre Moments	4-3
4-2	Composite Rectangles	4-3
4-3	Composite Equal-Angled Triangular Model	4-4
4-4	General Polygon Model	4-5
5-1	One Target, Three Clutter Objects and White Noise	5-2
5-2	Effects of Clutter on Probability of Anomaly	5-10
5-3	Example of Markov Random Field	5-12
6-1	Effects of Spatial Quantization	6-11
7-1	Distribution of Background and Object Edges	7-8
7-2	Plot of Edge Detection Probability vs. SNR for Different Target Sizes	7-9
7-3	Cases of Interest for Gap Analysis	7-10
7-4	Simplified Model for Object in Noisy Background	7-17
7-5	Probability of Correct Labeling of Interior Point as a Function of Edge Detection Probability	7-18
7-6	Cases of Interest for Interior Point Analysis	7-19
7-7	Probability of Correct Assignment of Object Points (P_{co}) and Probability of Correct Assignment of Back Background Points (P_{cb}) as a Function of Signal Noise Ratio (SNR)	7-22

LIST OF TABLES

Table		Page
5-1	Comparison of Analytic Bound on Probability of Anomaly with Monte Carlo Simulation	5-11
7-1	Theoretical and Experimental Values for SNR = 4. Experimental Values are Results of 10 Monte Carlo Simulations Run for Each Target Size	7-14
7-2	Table Illustrating Calculation of Probabilities Based Upon Figure 7-3	7-16
7-3	Experimental and Theoretical Results for PD(n), The Probability of Detecting a Square Containing No Nth- Order Gap, for SNR = 4 and $M/N^2 = 1/36$ (Experimental Values Based Upon 10 Monte Carlo Simulations.)	7-16

1.0 INTRODUCTION

Modern image processing systems use pattern recognition techniques to automatically process imagery generated by Forward Looking Infra-Red (FLIR) and other sensors. The ATAC FLIR Autocuer is an example of such a system that employs an automatic target classifier. The initial stage in autocuers is the extraction of shapes from the scene called (object) segmentation. These shapes are measured and the resulting features, characteristic of targets, are input to a classifier for automatic target classification/recognition. A variety of algorithms have been developed to perform this shape extraction function. These algorithms usually employ edge detection and intensity thresholding techniques, and some type of connectivity criteria which are heuristic in nature.

The performance of these algorithms has been judged subjectively, usually on limited data bases of FLIR imagery. For example, segmentation algorithms have been termed "good" if, when applied to a few images, the extracted objects look good to the algorithm developers. Factors such as noise sensitivity, presence of clutter, or pixel quantization are usually not a part of the evaluation of these techniques, even though these effects can have a profound effect on the performance of these processes. Quite often, the result of this approach is a set of algorithms or a hardware system that performs well on one set of FLIR images, but badly on another set. Then there is no way to ascertain qualitatively the reason for the poor performance or just what should be done to improve performance. For example, it is not always apparent that the problems are: fundamental to the algorithms; due to noisy or cluttered data; failure of the hardware or software implementation; or just a statistical accident.

Useful quantitative (analytic) results relating to these algorithms are difficult to obtain, due to the difficulty in modeling realistic scenes, the intractability of the algorithms themselves, and the difficulty in defining relevant and meaningful performance parameters. This report presents the beginnings of a more formal analysis of image processing systems such as the ATAC autocuer and in particular, the segmentation process. Since the autocuer is basically designed to find targets in a FLIR scene, the application of these results must be considered in relation to the following definitions.

- | | |
|-------------------|--|
| 1. Detection | Target or clutter |
| 2. Classification | Class of target, e.g., tracked or wheeled. |
| 3. Recognition | Type of vehicle, e.g., tank, APC, truck. |
| 4. Identification | Type of tank |

The goal of this report is the analysis of the classification of targets, with some application to recognition. In particular, many of the current results require a minimum of 3 pixels per dimension. The results will apply to recognition to the extent that recognition does not use internal structural detail, that is, recognition is performed by shape analysis alone.

The models generated also allow for simple clutter, where clutter is meant to be anything in the scene that is not a target or part of a uniform background. Two types of clutter were considered in terms of their effect on segmentation of a nearby target. The first type can be termed object clutter, such as a rock or tree that exhibits definite shape. The second type of clutter considered could be termed texture in that it does not exhibit a definite shape but rather a variation in the background intensity in the vicinity of a target. An example of this type of clutter is the variation in emissivity due to soil conditions.

The principal results of this analysis can be summarized as follows. First there is now an objective qualitative means of evaluating shape extraction algorithms in terms of specific performance parameters for arbitrary target shapes in the presence of noise and/or clutter, along with performance bounds on what an optimal process would be. Second, there is a means to show that for optimum target shape extraction, the algorithms must account for the presence of clutter, or adapt to it.

An overall modeling approach for image processing is presented in Section 2. This represents the approach used for this report where analytic results were obtained for a simple scene and model as in reference 1, and then extended by increasing the complexity of the model while maintaining tractability of the analysis.

Section 3 provides a brief background of the techniques used from detection/estimation theory and a definition of concepts used in defining performance of, e.g., an object segmentor.

Sections 4-6 follow the modeling philosophy of Section 2 by extending the basic technique of computing performance bounds to more complex models. The emphasis is on improving the realism of the model while maintaining the tractability of the analysis, in this case, the tractability of the Fisher information matrix, which is the key element in computing analytic performance bounds. In Section 4, a more complex target model is developed and expression for the elements of the Fisher information matrix derived for the recommended approach. In Section 5, the complexity of the scene model is increased by introducing clutter. Two types of clutter models are described and some complex derivations are presented to show that analytic results can be obtained. A verification of the results for the first model is presented by showing satisfactory agreement with results from a Monte Carlo computer simulation. In Section 6, the complexity of the model is increased by introducing a sensor model that exhibits detector quantization and analytic results of this development are presented.

Section 7 contains an analysis of the principal features of the ATAC segmentor. Included is an analysis of the Sobel edge operator with an analytic procedure for finding the probability of gaps in edges and an experimental verification; and an analysis of the selection of interior points to define the segmented object.

Recommendations for further development of analytic techniques in image processing are presented in Section 8.

The appendices contain some of the more detailed and complex derivations including some of the mathematical and statistical manipulations and concepts that have been found useful in the development of the various analytic results.

2.0 IMAGE PROCESSING MODELING PHILOSOPHY

The general problem of modeling an image processing system is illustrated in Figure 2-1 as four interrelated tasks. A scene is sensed by a sensor such as a FLIR, an algorithmic process is applied to the sensed data to obtain some reduced and meaningful data and an objective qualitative measure of the performance is obtained. The main difficulties in generating the performance model are the extreme complexity of the possible scenes and algorithms, and defining appropriate and meaningful performance parameters. In order to obtain a tractable performance analysis, the models of the three principal components (scene, sensor, process) need be simplified to account for the particular performance parameters. These depend on the very process being modeled, which in turn depends on the scenes to be recognized.

The philosophy for modeling the ATAC autocuer used in this effort was to start with a simple scene model, in this case a rectangular target imbedded in noise. Then the algorithmic processor, or portions thereof, are examined to determine its basic objective and which known analytic techniques (e.g. detection/estimation theory) were suitable for describing its performance. This results in both a tractable analysis for a simple case and the definition of appropriate performance parameters. Then, using those performance parameters, the complexity of the scene, sensor and process models are increased, while maintaining the tractability of the analysis. This modeling approach and philosophy does not result in attempting to model all possible real world scenes, but models the basic scene characteristics that have a recognizable effect on performance of the algorithm process.

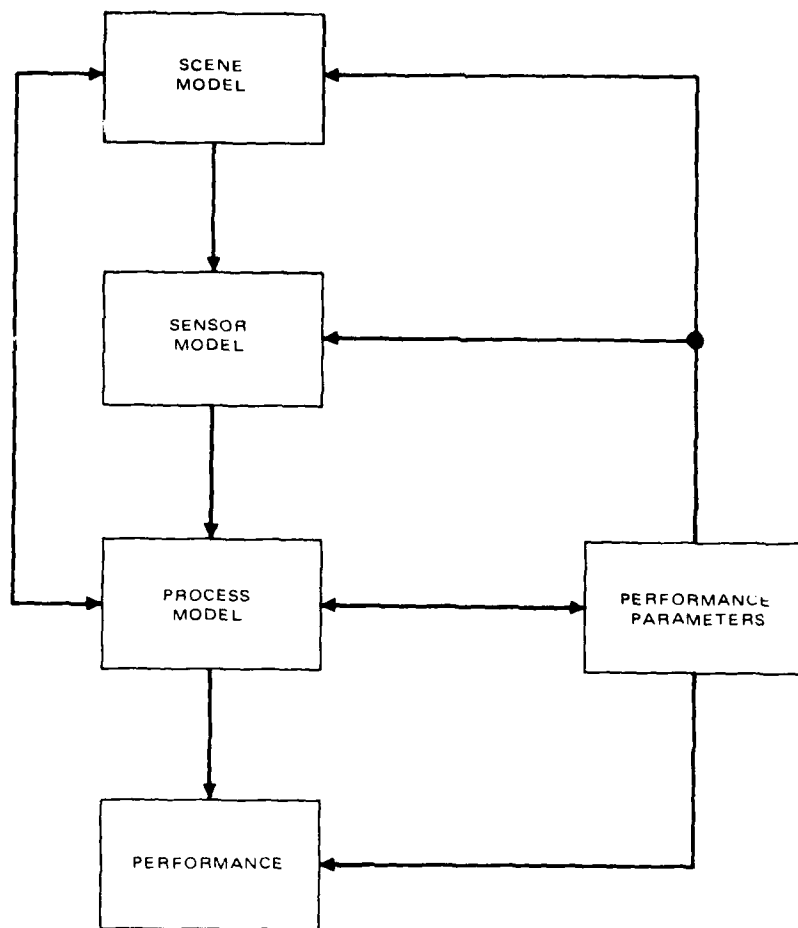


Figure 2-1. General Model Diagram.

This process is iterated into more complex models where the basic characteristics are modeled with the fewest possible parameters and in a functional form that maintains a tractable performance analysis.

3.0 BASIC ANALYTIC TECHNIQUES

The basic analytic technique used in the analysis of the simple rectangular segmentation (1) is based on detection and estimation theory (2). This approach uses the concept of maximum likelihood estimation to derive performance bounds on the optimum segmentation of a rectangle imbedded in white noise and defines the best possible performance against which any segmentation algorithm can be compared. This section provides a basic technical summary of the technique for both sampled and continuous wave forms.

In order to develop the principles of maximum likelihood, it is convenient to develop the principles for the "classical" estimation problem where the signals presented to the estimator are discrete samples. After developing the necessary results for the "classical" estimation problem these principles are extended to the case where the observation presented to the estimator is a continuous waveform. In addition, the development will be for the case where the observed signals are one dimensional, since the two dimensional case follows easily from this.

The use of the concept of maximum likelihood is significant in that it provides the optimum performance of the detection/estimation problem. With a knowledge of optimum performance, comparisons with specific algorithms can be made to determine if significant improvements can be made and possibly show where or in which direction to look for those improvements. In addition, there are powerful results in detection/estimation theory that permit computation of performance bounds for these optimum processes.

3.1 ESTIMATION THEORY

For the sampled signal case, the estimator observes the N discrete samples

$$r(t_i) = S(t_i, \underline{A}) + n(t_i) \quad (i = 1, 2, 3, \dots, N) \quad (3-1)$$

where \underline{A} is the feature vector representing the parameters to be estimated; the functional form of $S(t_i, \underline{A})$ is known but the $K \times 1$ vector \underline{A} is unknown; $n(t_i)$ is a white Gaussian process of zero mean and variance $N_0/2$. The estimator is required to use the N samples to estimate the parameter \underline{A} .

An estimator of \underline{A} is typically denoted by $\hat{\underline{A}}(r(t_1), r(t_2), \dots, r(t_N) | \underline{A})$. It is important to note that the estimator is a function of the observed samples, although we might write the estimator simply as $\hat{\underline{A}}$.

Noting the dependence of $\hat{\underline{A}}$ on the N observations, which are random, it is clear that $\hat{\underline{A}}$ is a random variable with an expected value. If this expectation is denoted

$$E(\hat{\underline{A}}(r(t_1), \dots, r(t_N) | \underline{A})) = \underline{A} \quad (3-2)$$

\underline{A} is said to be unbiased when this equality holds.

Clearly, it is reasonable to seek an estimator which will give estimates which are close to the true parameter value. Hence, (whenever possible) an estimator is used whose expected squared error around any element of \underline{A} is small; that is (if possible) an estimator is used such that

$$E(a_i - \hat{a}_i) \text{ is small for each } i (i = 1, 2, \dots, K) \quad (3-3)$$

where

$$\underline{A} = (a_1, a_2, \dots, a_K)^T, \quad \hat{\underline{A}} = (\hat{a}_1, \hat{a}_2, \hat{a}_3, \dots, \hat{a}_K)^T.$$

If an unbiased estimator is used, the well known Cramer-Rao (Ref. 2) inequality can be used to give an idea of how much squared error there will be in using the "best" unbiased estimator.

In order to apply the Cramer-Rao inequality, first define the Fisher information matrix, J , which has elements

$$J_{ij} = E \left(\frac{\partial \ln P(r(t_1), \dots, r(t_N))}{\partial a_i} \cdot \frac{\partial \ln P(r(t_1), \dots, r(t_N))}{\partial a_j} \right) \quad (3-4)$$

where $P(r(t_1), r(t_2), \dots, r(t_N))$ is the probability density or likelihood of the N observations. The Cramer-Rao inequality is then seen to be (2)

$$E \left((a_i - \hat{a}_i)^2 \right) = \text{Var} (\hat{a}_i - a_i) \geq J^{ii} \quad (3-5)$$

where J^{ii} is the ii^{th} element of the KKK matrix J^{-1} . An unbiased estimator, \hat{A} , is said to be efficient if equality holds in (3-5). Because of the value of the Cramer-Rao inequality in determining performance bounds, the Fisher information matrix becomes an important concept in the analysis of the remaining sections.

It must be pointed out that there is no reason to assume that an efficient estimator will always exist, and in fact, it is easy to find examples for which an efficient estimator does not exist. However, if an efficient estimator A exists, then (with probability of one) it will be given by the solution to

$$l(\hat{A}) = \max_{\underline{A}} P(r(t_1), r(t_2), \dots, r(t_N)), \quad (3-6)$$

which is the maximum likelihood estimate.

Since maximum likelihood estimators maximizes the likelihood of the observed samples, it is desirable to use them whether an efficient estimator exists or not. Then, the estimates will in general be quite good since for certain general conditions it has been shown that maximum likelihood estimates

- (1) converge to the correct parameter values as $N \rightarrow \infty$
- (2) become efficient as $N \rightarrow \infty$

Using (3-1), (3-6) and the assumptions about $M(t_i)$ the likelihood is seen to be

$$\ell(\underline{A}) = P(r(t_1), \dots, r(t_N)) = \prod_{j=1}^N P_j(r(t_j) | \underline{A}) \quad (3-7)$$

where the $P_j(r(t_j) | \underline{A})$'s are the probability densities of the $r(t_j)$'s. Then

$$\ell(\underline{A}) = \left(\frac{1}{\pi N_0} \right)^{N/2} \exp \left(- \frac{1}{N_0} \sum_{i=1}^N (r(t_i) - S(t_i, \underline{A}))^2 \right) \quad (3-8)$$

where N_0 is the noise spectral power. It is usually easier to find the value of \underline{A} which maximizes $\ln \ell(\underline{A})$ rather than $\ell(\underline{A})$. Therefore, it is usually best to work with the log-likelihood.

$$\Lambda_1(\underline{A}) = \ln(\underline{A}), \quad (3-9)$$

which reduces to

$$\Lambda_1(\underline{A}) = -\frac{N}{2} \ln(\pi N_0) - \frac{1}{N_0} \sum_{i=1}^N r^2(t_i) + \frac{2}{N_0} \sum_{i=1}^N \left(r(t_i) S(t_i, \underline{A}) - \frac{S^2(t_i, \underline{A})}{2} \right) \quad (3-10)$$

Note that in (3-10) the first two terms do not depend on the parameters to be estimated. Consequently, the first two terms would typically be dropped, and the log-likelihood would be redefined to be

$$\Lambda_2(\underline{A}) = \frac{2}{N_0} \sum_{i=1}^N S(t_i, \underline{A}) \left(r(t_i) - \frac{S(t_i, \underline{A})}{2} \right) \quad (3-11)$$

Equation (3-11) is the form of the log-likelihood that would typically be used in estimating A and in computing the Fisher information matrix. For the continuous wave form case, this equation converges to

$$\Lambda' = \frac{2}{N_0} \int_0^T r(t) S(t, \underline{A}) dt - \frac{1}{N_0} \int_0^T S^2(t, \underline{A}) dt \quad (3-12)$$

This is the form of the log-likelihood which would be used to compute the maximum likelihood estimator, the Fisher information matrix, or any other quantity associated with maximum likelihood estimation in the continuous case.

3.2 PROBABILITY OF ANOMALY

The developments in Section 3.1 provide the basic means for developing tight performance bounds when the process results in output near the true results. For example, in the problem of segmenting an object from the background those developments can be used to obtain good performance bounds when that object is segmented, but not exactly. To describe complete performance it is necessary to define an additional criterion, termed the probability of anomaly. This is the probability of detecting falsely. In the segmentation example, it is the probability that the true object is not formed, but rather the segmentor "finds" something in another part of the scene due, e.g., to noise. This situation occurs when the likelihood function in an area containing only noise exceeds the likelihood function of the area containing the object itself.

The computation of this probability of anomaly uses the same basic concepts as the performance bounds, that is, the likelihood equation provides the key parameters used in the analytic computations. Examples of this process are given in later sections.

4.0 TARGET MODELS

The first problem in the analysis of target classification algorithms using the techniques of maximum likelihood estimation is to obtain simple target models that are tractable analytically. By this it is meant that the Fisher information matrix (Section 3)

$$J_{ij} = \frac{2}{N_0} \iint \frac{\partial I(x, y, \underline{f})}{\partial f_i} \frac{\partial I(x, y, \underline{f})}{\partial f_j} dx dy \quad (4-1)$$

can be easily inverted where $I(x, y, \underline{f})$ is the intensity function of the target model, and that the feature vector \underline{f} describing the target has the smallest dimension possible.

4.1 APPROACHES EXAMINED

In this section a number of possible representations of $I(x, y, \underline{f})$ are described.

2-D Legendre Polynomial Representation

These polynomials, $P(\cdot)$, are orthogonal on a square window and in principal can be used to approximate any continuous shape. If the target intensities are given by $I(x, y)$ then the least square approximation by the polynomials is given by minimizing the expression

$$\iint \left[\sum_i \sum_j a_{ij} P_i(x) P_j(y) - I(x, y) \right]^2 dx dy \quad (4-2)$$

for each i and j . Since these polynomials are orthogonal, the minimum is given by the coefficients a_{ij} defined by

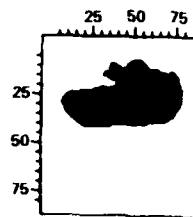
$$a_{ij} = \iint I(x, y) P_i(x) P_j(y) dx dy \quad (4-3)$$

Since the polynomials $P_i(x)$ and $P_j(y)$ are polynomials in x and y of degree i and j , these coefficients are just linear combinations of the various moments of the target intensities. The motivation for this approach was that many target classification approaches, including the ATAC FLIR autocuer use moments as target features in the classification process. In order to determine how well these polynomial moments can approximate the shape of a target, an experiment was performed on a typical tank shape. The polynomial moments a_{ij} were computed using Equation (4-3) and the corresponding shape approximation reconstructed using the summation term in Equation (4-2), for several cases of different orders of moments. The results are shown in Figure 4-1, where it is apparent that a good approximation can require moments to the 20th order. This would require over 200 coefficients for target representation, which is too high to be practical. In addition, the coefficients are not immediately scale and rotation invariant.

The principal advantage of this approach is that due to the orthogonality of the polynomials, the Fisher information matrix (4-1) becomes diagonal and need not be inverted. However, this did not prove sufficiently advantageous to adopt this approach.

Composite Rectangle Model

The second model considered was the composite rectangle model (Figure 4-2). In this approach an arbitrary target shape is approximated by rectangles of various sizes. The advantage of this approach is that any shape can be reasonably approximated. The disadvantage is that it is not tractable mathematically. This is because each rectangle must be adjacent to at least one other, causing many non-diagonal elements in the



SILHOUETTE OF AN M60 TANK

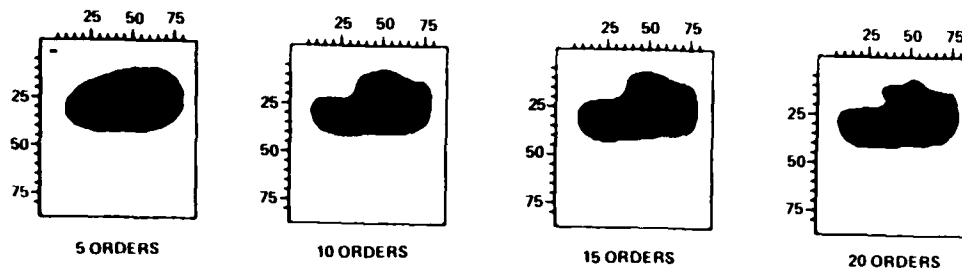


Figure 4-1. Reconstruction using legendre moments.

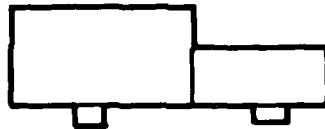


Figure 4-2. Composite rectangles.

Fisher matrix. It also is difficult to model the adjacency of rectangle edges mathematically for arbitrary configurations.

Composite Equal-Angled Triangular Model

This type of model, as illustrated in Figure 4-3, can approximate many shapes and is mathematically more tractable than the composite rectangular model since triangles have a more easily described relationship to each other than do rectangles. The disadvantage is that some shapes, those for which the radius vector is not a single-valued function of angle, cannot be represented with this model.

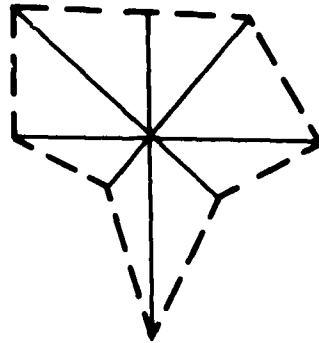


Figure 4-3. Composite equal-angled triangular model.

General Polygonal Model

This approach is to approximate any shape by specifying points on the boundary and attaching them with straight line segments. An example of this approach is shown in Figure 4-4. Any shape can be approximated in this way realistically using relatively few parameters. In addition, this approach exactly describes a rectangle so it is a direct extension of rectangular targets to more complex shapes. These features, as well as the tractability of this representation resulted in the selection of this representation.

The results for the general polygonal case are as follows. Let the Fisher matrix (4-1) be applied to the case of a polygon of N sides whose vertices are specified by coordinates (x_1, y_1) , (x_2, y_2) , ..., (x_N, y_N) , shown in Figure 4-4.

It is assumed that inside the polygon $I(x, y, f) = \Delta T$, while outside the polygon $I = 0$, except at points nearer to the boundary than a small distance $\pm \delta/2$ (assumed to be small compared with any side of the polygon). It is assumed that within this small region of width δ , I varies linearly from its value ΔT inside the boundary to its value zero outside the boundary.

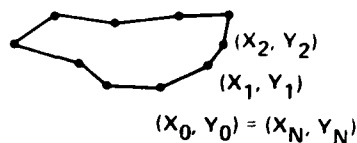


Figure 4-4. General polygon model.

It is further assumed that f_1 , the first shape feature = ΔT , and that for all parameters f_i , f_j , $i, j > 1$, i depends upon f_j only through the vertices (x_n, y_n) $n = 1, 2, \dots, N$. That is

$$\begin{aligned} x_n &= x_n(f_2, f_3, \dots, f_M) \\ y_n &= y_n(f_2, f_3, \dots, f_M) \end{aligned} \quad M \leq 2N + 1$$

Aside from these restrictions, the f_i 's can be chosen arbitrarily so long as they are independent.

For example, two coordinates might specify a centroid, or other fixed point, to which all other rotations or forms are to be referred, one coordinate might specify rotation in the plane, two coordinates could refer to aspect angles of the three dimensional object being projected onto the image plane.

Then, to a good approximation (see Appendix G)

$$J_{11} = \frac{2}{N_0} \cdot (\text{area enclosed by boundary})$$

$$\begin{aligned} J_{1j} &= -\frac{\Delta T}{N_0} \sum_{n=1}^N \left[\Delta x_n \frac{\partial \bar{y}_n}{\partial f_j} - \Delta y_n \frac{\partial \bar{x}_n}{\partial f_j} \right] \\ &= -\frac{\Delta T}{N_0} \sum_{n=1}^N L_n \left[-\sin \theta_n \frac{\partial \bar{x}_n}{\partial f_j} + \cos \theta_n \frac{\partial \bar{y}_n}{\partial f_j} \right] \end{aligned}$$

where (\bar{x}_n, \bar{y}_n) are coordinates of the midpoint of the n th side

$$\bar{x}_n = \frac{x_n + x_{n-1}}{2}$$

$$\bar{y}_n = \frac{y_n + y_{n-1}}{2}$$

$(\Delta x_n, \Delta y_n)$ are the relative coordinates of the n th side, L_n is the length of the n th side,

$$L_n = \left[(\Delta x_n)^2 + (\Delta y_n)^2 \right]^{1/2}$$

θ_n is the angle (with respect to the positive X axis made by the n th side.

$$\theta_n = \tan^{-1} \frac{\Delta y_n}{\Delta x_n}$$

$$\sin \theta_n = \frac{\Delta y_n}{L_n}$$

$$\cos \theta_n = \frac{\Delta x_n}{L_n}$$

For $i, j > 1$, the elements of the Fisher information matrix are

$$J_{ij} = \frac{2(\Delta T)^2}{N_0 \delta} \sum_{n=1}^N L_n \left\{ \left[-\sin \theta_n \frac{\partial \bar{x}_n}{\partial f_i} + \cos \theta_n \frac{\partial \bar{y}_n}{\partial f_i} \right] \right. \\ \left. \cdot \left[-\sin \theta_n \frac{\partial \bar{x}_n}{\partial f_j} + \cos \theta_n \frac{\partial \bar{y}_n}{\partial f_j} \right] + \frac{L_n^2}{12} \frac{\partial \theta_n}{\partial f_i} \frac{\partial \theta_n}{\partial f_j} \right\}$$

The quantities $\frac{\partial \theta_n}{\partial f_i}$ can also be written in the form:

$$\begin{aligned}\frac{\partial \theta_n}{\partial f_i} &= L_n^{-2} \left[\Delta x_n \frac{\partial \Delta y_n}{\partial f_i} - \Delta y_n \frac{\partial \Delta x_n}{\partial f_i} \right] \\ &= L_n^{-1} \left[\cos \theta_n \frac{\partial \Delta y_n}{\partial f_i} - \sin \theta_n \frac{\partial \Delta x_n}{\partial f_i} \right]\end{aligned}$$

It has been verified that these results reduce correctly to those given in reference 1 for the case of a rectangle.

4.2 SIGNIFICANCE OF THESE RESULTS

These results extend the past work to the case of an arbitrary polygon depending upon an arbitrary set of feature parameters. The only requirement is that the vertices of the polygon be known differentiable functions of the feature parameters. The two-dimensional integral defining the Fisher information matrix (FIM) has been converted into a relatively simple one-dimensional sum over the sides and vertices of the polygon.

Algebraic or numerical inversion of the FIM can be obtained for any case of practical interest to obtain bounds on the variances of the feature parameters.

The fact that the model is an arbitrary N-sided polygon makes it applicable to a wide variety of military targets and clutter objects. As long as targets and clutter objects don't overlap, the FIM will be readily separable into corresponding constituent parts. For example, an actual silhouette of a target of interest could be represented by selecting points on the boundary that give an arbitrarily accurate representation of the shape. The performance bounds for optimum segmentation for this representation can then be computed using the results of this section applied to the coordinates of these points. These results can be compared for differing shape approximations to find the simplest representation of the target that does not significantly alter the analytic results, yielding an acceptable target model.

5.0 CLUTTER MODELING

This section presents analysis and results on modeling the effects of simple clutter on target segmentation processes. Sections 5.1 and 5.2 present two clutter models, Section 5.3 shows results of the presence of clutter on target segmentors, Section 5.4 gives results of a Monte Carlo simulation to verify the analytic bounds on probability of anomaly (derived in Appendix H) and Section 5.5 shows an example of what probabilistic textured clutter could look like.

As a basic assumption it is assumed that clutter is any object in the FOV that is not a target or noise. The only restriction placed on the clutter is that it never masks the target although target masking of clutter is allowed, and that if there are multiple clutter objects in the FOV they never overlap. For any arbitrary shaped clutter object in the plane the clutter object's shape can be approximated by the polygon method described in the previous section. That is, one could connect vertices by straight lines to approximate the shape of the clutter object. The vertex locations can be assumed to be unknown or random. More detailed assumptions will be made later, in order to get a realistic but mathematically tractable clutter model.

5.1 CLUTTER MODEL 1

In addition to the target parameters that must be estimated, assume that the vertices of each clutter object are unknown and must be estimated and that the intensity offset of each clutter object is unknown and must also be estimated. The number K of clutter objects is assumed known.

Figure 5-1 illustrates the setup for $K = 3$. This can be represented as:

$$I(x, y) = \Delta T S(x, y) * P(x, y) \quad (5-1)$$

$$+ \left(\sum_{j=1}^K \mu_j (1 - S(x, y)) C_j(x, y) \right) * P(x, y) + n(x, y)$$

where

$I(x, y)$ = observed intensity distribution

$$S(x, y) = \begin{cases} 1 & \text{if } x, y \text{ is on target} \\ 0 & \text{otherwise} \end{cases}$$

and

$$C_j(x, y) = \begin{cases} 1 & \text{if } x, y \text{ is on clutter object } j \\ 0 & \text{otherwise} \end{cases}$$

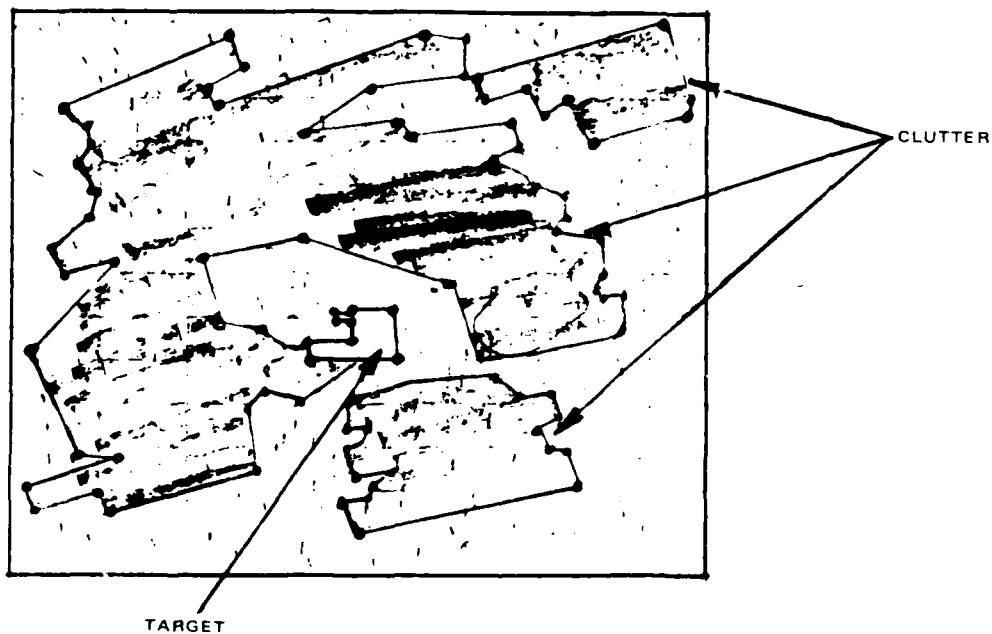


Figure 5-1. One target, three clutter objects and white noise.

ΔT = target intensity offset

μ_j = intensity offset of j^{th} clutter object,

$n(x, y)$ = zero mean Gaussian white noise process,

$$P(x, y) = \begin{cases} \frac{1}{r^2} & \text{for } |x| \leq \frac{r}{2} \text{ and } |y| \leq \frac{r}{2} \text{ (blur function)} \\ 0 & \text{otherwise} \end{cases}$$

and $*$ denotes two dimensional convolution

Let $S(x, y) = S'(x, y) * P(x, y)$ and $C(x, y) = C'(x, y) * P(x, y)$, and assume an unbiased estimator for $I(x, y)$

Since

$$\Delta T \cdot S(x, y) + \sum_{j=1}^K (1 - S(x, y)) \mu_j C_j(x, y) \quad (5-2)$$

is non-random, the equation for the likelihood and the Fisher information matrix can be obtained directly (reference 2, Chapt. 4). The log likelihood Λ' , follows from equation (3-12) and is

$$\begin{aligned} \Lambda' = & \frac{2}{N_0} \iint_{\text{FOV}} I(x, y) \left[\Delta T S(x, y) + \sum_{j=1}^K (1 - S(x, y)) \mu_j C_j(x, y) \right] dx dy \\ & - \frac{1}{N_0} \iint_{\text{FOV}} \left[\Delta T S(x, y) + \sum_{j=1}^K (1 - S(x, y)) \mu_j C_j(x, y) \right]^2 dx dy \end{aligned} \quad (5-3)$$

Now assume that γ is much smaller than the target and clutter dimension.

Then in this case $S^2(x, y) \approx S(x, y)$ and $C_j^2(x, y) \approx C_j(x, y)$ and (5-3) reduces to

$$\Lambda' = \frac{2}{N_o} \left[\iint_{\text{FOV}} \Delta T S(x, y) \left(I(x, y) - \frac{\Delta T}{2} \right) dx dy \right] + \frac{2}{N_o} \sum_{j=1}^K \iint_{\text{FOV}} \left(\mu_j (1 - S(x, y)) C_j(x, y) \right) \left(I(x, y) - \frac{\mu_j}{2} \right) dx dy \quad (5-4)$$

Note that this is the sum of $K+1$ matched filters, one matched to the target and K matched to the K clutter objects.

Due to the separability of the log likelihood function into target and clutter components it can be shown that

$$\underline{J} = \langle J_{ij} \rangle = \begin{bmatrix} \underline{J}_1 & \underline{0} \\ \underline{0} & \underline{C} \end{bmatrix} \quad (5-5)$$

where \underline{J}_1 is the $P \times P$ square matrix corresponding to a p parameter target and \underline{C} is a $QK \times QK$ square matrix corresponding to KQ parameter clutter object.

For a rectangle target as in (1) and the target parameters to be estimated are as in (1), it is not hard to show that \underline{J}_1 is the 5×5 Fisher information matrix computed in reference 1, and \underline{C} is the information matrix of the clutter. Since

$$\underline{J}^{-1} = \begin{bmatrix} \underline{J}_1^{-1} & \underline{0} \\ \underline{0} & \underline{C}^{-1} \end{bmatrix} \quad (5-6)$$

the same target estimation bounds apply here as in (1).

5.2 CLUTTER MODEL II

This clutter model is similar to model I. All the assumptions of model I apply; however, model I is extended so that each clutter object's offset intensity is random. That is,

$$I(x, y) = \Delta T S(x, y) + \sum_{j=1}^K (1 - S(x, y)) C_j(x, y) \mu$$

$$+ \sum_{j=1}^K (1 - S(x, y)) C_j(x, y) T_j + n(x, y) \quad (5-7)$$

where all variables are the same as in model I except that T_j 's, which are assumed to be independent Gaussian with

$$\mathcal{E}(T_j) = 0, \text{Var}(T_j) = \sigma^2, j = 1, 2, 3, \dots, K.$$

For this model the total noise is non-white

$$n_c(x, y) = \sum_{j=1}^K (1 - S(x, y)) C_j(x, y) T_j + n(x, y)$$

The autocorrelation of the non-white noise is

$$\mathcal{E}(n_c(x, y) n_c(u, v)) = K_n(x, y, u, v)$$

$$= \sum_{j=1}^K \sigma^2 (1 - S(x, y)) C_j(x, y)$$

$$\cdot (1 - S(u, v)) C_j(u, v) + \frac{N_0}{2} \delta(x - u, y - v) \quad (5-8)$$

Let

$$K_s(x, y, u, v) = \sum_{j=1}^K \sigma^2 (1 - S(x, y)) C_j(x, y) \cdot (1 - S(u, v)) C_j(u, v) \quad (5-9)$$

$K_s(x, y, u, v)$ is a separable kernel as in reference 3 (Section 7.3).

Since

$$\iint_{\text{FOV}} (1 - S(x, y))^2 \frac{C_j(x, y)}{\sqrt{A_j}} \frac{C_i(x, y)}{\sqrt{A_i}} dx dy = \delta_{ij} \quad (5-10a)$$

where A_i is the area of the i^{th} clutter object, set

$$\phi_j(x, y) = (1 - S(x, y)) C_j(x, y) / \sqrt{A_j}, \quad j=1, 2, 3, \dots, K \quad (5-10b)$$

$$\lambda_j = \sigma^2 A_j, \quad j=1, 2, 3, \dots, K \quad (5-10c)$$

$$\lambda_j = 0, \quad j > K \quad (5-10d)$$

and

$$\phi_{K+1}(x, y) = \frac{S(x, y)}{\sqrt{A_s}}, \quad A_s \text{ is area of target.} \quad (5-10e)$$

Let

$$m(x, y) = \left\{ \Delta T S(x, y) + \sum_{j=1}^K \mu (1 - S(x, y)) C_j(x, y) \right\}. \quad (5-11)$$

Then the log-likelihood is (see reference 3, Chapt. 6)

$$\begin{aligned}
 \Lambda_1 = & \frac{1}{N_0} \sum_{i=1}^K \frac{\lambda_i r_i^2}{(\lambda_i + N_0/2)} + \sum_{i=1}^K \frac{m_i r_i}{\lambda_i + N_0/2} \\
 & + \sum_{i=K+1}^{\infty} \frac{1}{N_0/2} m_i r_i - \frac{1}{2} \sum_{i=1}^K \ln \left(1 + \frac{2\lambda_i}{N_0} \right) - \frac{1}{2} \sum_{i=1}^K \frac{m_i^2}{\lambda_i + N_0/2} \\
 & - \frac{1}{2} \sum_{L=K+1}^{\infty} \frac{m_L^2}{N_0/2}
 \end{aligned} \tag{5-12}$$

where

$$r_i = \iint_{\text{FOV}} I(x, y) (1 - S(x, y)) \frac{C_i(x, y)}{\sqrt{A_i}} dx dy \quad i=1, 2, 3, \dots, K$$

and

$$r_{K+1} = \iint_{\text{FOV}} I(x, y) \frac{S(x, y)}{\sqrt{A_s}} dx dy ,$$

$$m_i = \iint_{\text{FOV}} m(x, y) (1 - S(x, y)) \frac{C_i(x, y)}{\sqrt{A_i}} dx dy$$

$$= \mu \sqrt{A_i} \quad i=1, 2, \dots, K$$

Then the log-likelihood (5-12) reduces to

$$\begin{aligned}
 \Lambda_1 = & \frac{1}{N_0} \sum_{j=1}^K \frac{\sigma^2 A_j}{\sigma^2 A_j + N_0/2} r_j^2 + \sum_{j=1}^K \frac{\mu \sqrt{A_j}}{\sigma^2 A_j + N_0/2} r_j \\
 & + \frac{2}{N_0} \Delta T \iint_{\text{FOV}} I(x, y) S(x, y) dx dy \\
 & - \frac{1}{2} \sum_{i=1}^K \ln \left(1 + \frac{2 \sigma^2 A_i}{N_0} \right) - \frac{1}{2} \sum_{j=1}^K \frac{\mu^2 A_j}{\sigma^2 A_j + N_0/2} \\
 & - \frac{\Delta T^2 A_s}{N_0}
 \end{aligned} \tag{5-12b}$$

To compute the Fisher information matrix, set

$$\begin{aligned}
 h(x, y, u, v) = & \sum_{i=1}^K \left(\frac{\sigma^2 A_i}{\frac{N_0}{2} + \sigma^2 A_i} \right) (1 - S(x, y)) C_i(x, y) \\
 & \cdot (1 - S(u, v)) C_i(u, v),
 \end{aligned} \tag{5-13}$$

$$Q_r(x, y, u, v) = \frac{2}{N_0} (\delta(x - u, y - v) - h(x, y, u, v)) \tag{5-14}$$

and

$$K_r(x, y, u, v) = \sum_{i=1}^K \sigma^2 A_i (1 - S(x, y)) C_i(x, y) (1 - S(u, v)) C_i(u, v) \tag{5-15}$$

Then from Reference 3, Chapter 7, the elements of the Fisher information matrix are

$$J_{kf} = \iint_{\text{FOV}} \iint_{\text{FOV}} \left[\frac{\partial m(x, y)}{\partial f_k} \cdot Q_r(x, y, u, v) \cdot \frac{\partial m(u, v)}{\partial f_f} - \frac{1}{2} \frac{\partial k_r(x, y, u, v)}{\partial f_k} \cdot \frac{\partial Q_r(x, y, u, v)}{\partial f_f} \right] dx dy du dv \quad (5-16)$$

In this section it was shown that for this model there is a closed form expression for the likelihood (equation 5-12b), which is needed to compute probability of anomaly. Also, there is an expression for the elements of the Fisher information matrix (5-16). Applications of these formulae to compute the probability of anomaly for scenes with simple clutter can be found in Appendix II.

5.3 EFFECTS OF CLUTTER ON TARGET SEGMENTATION

In order to evaluate the effects of clutter on target segmentation, it will be assumed that there is a target and a clutter object of known shape but unknown size and location. With this assumption it is possible to determine probability of anomaly for three cases of interest. (See Appendix II.)

1. There is a target and a clutter object in the scene, and the segmentor is optimized for this situation.
2. There is a target and a clutter object in the scene, but the segmentor is optimized for a target only in the scene.
3. There is only a target in the scene but the segmentor is optimized for target and clutter object in the scene.

Figure 5-2 shows the probability of anomaly for these cases, where the target is a 5 x 5 square and the clutter is a 5 x 10 rectangle, as a function of signal to noise ratio. These curves show clearly that the segmentor should be constructed to account for the presence of clutter to get the best performance. That is, any segmentation algorithm should specifically

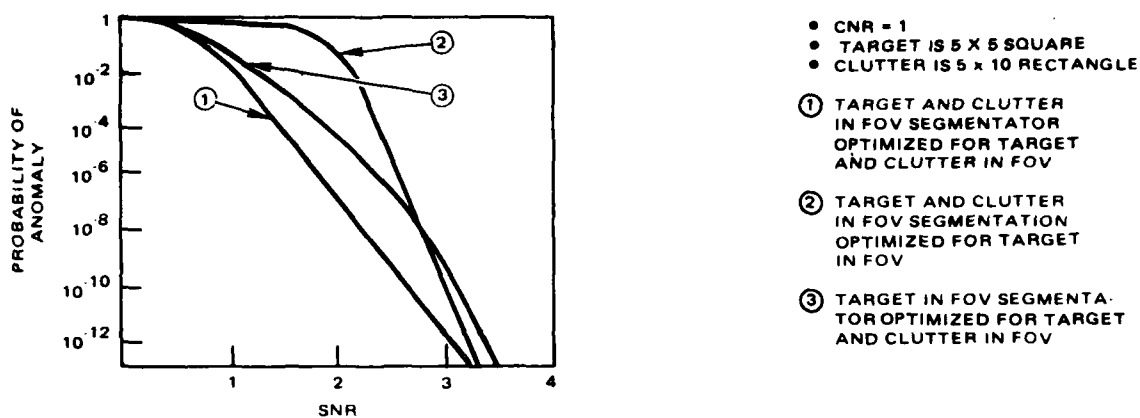


Figure 5-2. Effects of clutter on probability of anomaly.

account for or adopt to the presence of clutter objects in the vicinity of targets in order to achieve good performance. Otherwise, if there is a clutter object, performance will be limited to be no better than the second curve in Figure 5-2.

5.4 VERIFICATION OF PROBABILITY OF ANOMALY BOUNDS

As stated above, the derivation of analytic bounds on probability of anomaly for segmentation of a target in the presence of clutter is given in Appendix H. Some verification of the bounds using Monte Carlo estimation of probability of anomaly is desirable to verify the analytic bounds. Since a general verification of the principal result (Equation H26) was not feasible due to the high dimensionality of the problem and the consequent high computer processing cost, a modified version of the general problem was selected for verification. The basic simplifying assumptions were:

1. The target is known to be a square.
2. The clutter object is known to be a rectangle of width ℓ_c and height $2\ell_c$.
3. The vertical (in the scene) location of the target and clutter is known.

These assumptions reduced the dimensionality of the process, allowing for a reasonable verification to be performed. The results of this

verification are shown in Table 5-1 where it is seen that results from the analytic bound computation and Monte Carlo Simulation are similar.

TABLE 5-1. COMPARISON OF ANALYTIC BOUND ON PROBABILITY OF ANOMALY WITH MONTE CARLO SIMULATION

Signal to Noise Ratio	Analytic Bound*	No. of Anomalies from Simulation	No. of Trials
.1	1	10	10
.2	0.402	6	10
.3	0.35	4	10
.5	0.254	2	10
1	0.013	0	30
2	7×10^{-7}	0	10
4	0	0	10
*CNR = 1 in Eq. (H26)			

5.5 TEXTURED CLUTTER

The results of the previous two sections were for the first type of clutter objects in the target scene; a natural extension of this analysis would include consideration of the textured background type of clutter. An initial approach would be to assume that the textured background can be represented by a wide-sense stationary random field. In this case, the textured background can be represented by the equation,

$$n_{B_g}(x, y) = \alpha_x g(x - 1, y) + \alpha_y g(x, y - 1) - \alpha_x \alpha_y g(x - 1, y - 1) \quad (5-17)$$

where α_x and α_y are the texture features parameters and $g(x, y)$ is given by

$$g(x, y) = T_T S(x, y) + T_C C(x, y) + (1 - C(x, y)) (1 - S(x, y)) m_{B_{\alpha}}(x, y) + n(x, y) \quad (5-18)$$

The remaining terms of the latter equation are as defined in Appendix H.

An example of this type of textured background is shown in Figure 5-3, as generated by computer simulation of the above equations with no target or clutter objects.

An extension of this concept of clutter to verify its realism to real FLIR image effects and a possible extension of the analytic results to this case is a future research task.

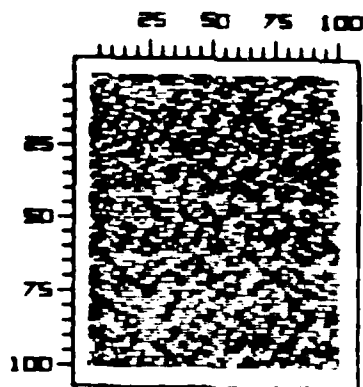


Figure 5-3. Example of Markov random field.

6.0 SENSOR MODEL

The analytic results obtained in the previous sections did not include a realistic sensor model, in particular, the effects of sensor spatial quantization. In this section, the basic analytic techniques for computing performance bounds for an optimum segmentation of a simple scene are extended to account for this improved sensor model.

A natural approach is to compute all pertinent quantities (Fishers information matrix, likelihood equation, performance measures, etc.) in terms of the spatially sampled intensity distribution which is present to the object segmenter. We could then vary the sampling rate and observe the resulting behavior of any performance measures being studied.

In order to apply this method to the model presented in Reference 1, first the statistical characteristics of the sampled intensity distribution is determined; then the likelihood equation is derived, from which Cramer-Rao and probability of anomaly bounds can be determined.

The derivation of the statistical characteristics of the sampled intensity distribution is as follows:

Let $I(x, y)$ be the analog intensity distribution on the image plane, that is,

$$I(x, y) = S(x, y) + n(x, y) \quad (6-1)$$

where

$$S(x, y) = \Delta T \cdot S_1(x) \cdot S_2(y) \quad (6-2)$$

is the target, and

$$S_1(x) = \begin{cases} 1 & |x - c_x| \leq L_x/2 \\ 0 & \text{otherwise} \end{cases} \quad (6-3)$$

$$S_2(y) = \begin{cases} 1 & |y - c_y| \leq L_y/2 \\ 0 & \text{otherwise} \end{cases} \quad (6-4)$$

and $n(x, y)$ is a zero mean Gaussian white noise process with spectrum amplitude $\frac{N_0}{2}$.

Assuming a detector of dimension $r \times r$ and of uniform responsivity, the signal available to the object segmentor from a detector whose center is at (x, y) is proportional to

$$I_1(x, y) = \int_{-r/2}^{r/2} \int_{-r/2}^{r/2} I(x - u, y - v) P(u, v) du dv \quad (6-5)$$

where

$$P(u, v) = \begin{cases} 1/r^2 & |u| \leq r/2, |v| \leq r/2 \\ 0 & \text{otherwise} \end{cases} \quad (6-6)$$

Assuming that the samples are taken at $\Delta X = \Delta + \frac{r}{2}$ and $\Delta Y = \Delta + \frac{r}{2}$ units apart, the sampled image that the object segmentor will process is; for $1 \leq i, j \leq N$: $I_s(x_i, y_j) = I_1(\Delta x(i - 1/2), \Delta y(j - 1/2))$

$$= \int_{-r/2}^{r/2} \int_{-r/2}^{r/2} S(\Delta x(i - 1/2) - u, \Delta y(j - 1/2) - v) \cdot P(u, v) du dv \quad (6-7)$$

$$+ \int_{-r/2}^{r/2} \int_{-r/2}^{r/2} P(u, v) n(\Delta x(i - 1/2) - u, \Delta y(j - 1/2) - v) du dv \quad (6-8)$$

The mean of the sampled image is

$$u_{ij} = \epsilon(I_s(x_i, y_j)) \quad (6-9)$$

which can be reduced to

$$u_{ij} = \frac{\Delta T}{r^2} \text{Area (Pixel (i, j) in } \mathcal{P}) \quad (6-10)$$

where \mathcal{P} is the set of all points that lie on the target. The variance of the sampled image is

$$\begin{aligned} \text{Var } I_s(x_i, y_j) &= \text{Var} \int_{-r/2}^{r/2} \int_{-r/2}^{r/2} (P(u, v) n(\Delta x(i - 1/2) - u, \\ &\quad \Delta y(j - 1/2) - v)) du dv \\ &= \epsilon \left\{ \int_{-r/2}^{r/2} \int_{-r/2}^{r/2} P(u, v) n(\Delta x(i - 1/2) - u, \right. \\ &\quad \left. \Delta y(j - 1/2) - v) du dv \right\}^2 \end{aligned} \quad (6-11)$$

Evaluation of the integrals results in

$$\text{Var } I_s(x_i, y_j) = \frac{N_o}{2r^2} \quad (6-12)$$

Having completely specified the statistical characteristics of the sampled image $I_s(x_i, y_j)$, this segmentation problem can be treated almost exactly as the continuous segmentation problem in Reference 1. The object segmenter observes $I_s(x_i, y_j)$ $i, j = 1, 2, 3, \dots, N$ and is required to estimate C_x, C_y, L_x, L_y and ΔT .

As in Reference 1, the Fisher information matrix is used to obtain estimation error bounds. First, however, the likelihood equation must be determined so that Fisher's information matrix can be obtained.

The likelihood is:

$$\ell = \prod_{i=1}^N \prod_{j=1}^N \frac{1}{\sqrt{2\pi} \frac{N_o}{2r^2}} \exp \left(-\frac{1}{2} \left(\frac{2r^2}{N_o} \right) (I_s(x_i, y_j) - \mu_{ij})^2 \right) \quad (6-13)$$

Taking the log, the log-likelihood is seen to be

$$\begin{aligned} \Lambda = \ln \left(\frac{2}{\pi N_o} \right)^{N^2/2} & - \frac{1}{N_o r^{-2}} \left(\sum_{i=1}^N \sum_{j=1}^N I_s^2(x_i, y_j) \right) \\ & - \frac{1}{r^{-2} N_o} \left(\sum_{i=1}^N \sum_{j=1}^N \mu_{ij}^2 - 2 I_s(x_i, y_j) \mu_{ij} \right) \end{aligned} \quad (6-14)$$

Noting that the first two terms are independent of the parameters to be estimated, we write the log-likelihood as

$$\Lambda_1 = \frac{-1}{r^{-2} N_o} \left(\sum_{i=1}^N \sum_{j=1}^N \mu_{ij}^2 - 2 I_s(x_i, y_j) \mu_{ij} \right) \quad (6-15)$$

$$= \frac{2}{N_o r^{-2}} \left(\sum_{i=1}^N \sum_{j=1}^N I_s(x_i, y_j) \mu_{ij} - \frac{\mu_{ij}^2}{2} \right) \quad (6-16)$$

$$\begin{aligned} &= \frac{2}{N_o r^{-2}} \sum_{i=1}^N \sum_{j=1}^N \frac{\Delta T}{r^2} \text{Area (Pixel (i, j) on } \mathcal{P}) I_s(x_i, y_j) \\ &\quad - \left(\frac{\Delta T}{r^2} \cdot \text{Area (Pixel (i, j) on } \mathcal{P}) \right)^2 \end{aligned} \quad (6-17)$$

Using (6-15) - (6-17) to compute the Fisher information matrix, which by definition is given by

$$\underline{J} = (J_{ij}) = E \left(\frac{\partial \Lambda_1}{\partial f_i} \cdot \frac{\partial \Lambda_1}{\partial f_j} \right) \quad (6-18)$$

where Λ_1 is the log-likelihood and f_i, f_j are parameters to be estimated, results in the expression

$$\frac{\partial \Lambda_1}{\partial f_k} = \frac{2r^2}{N_0} \sum_{i=1}^N \sum_{j=1}^N \left(I_s(x_i, y_j) \frac{\partial \mu_{ij}}{\partial f_k} - \mu_{ij} \frac{\partial \mu_{ij}}{\partial f_k} \right) \quad (6-19)$$

and after some manipulation,

$$E \left\{ \frac{\partial \Lambda_1}{\partial f_k} \cdot \frac{\partial \Lambda_1}{\partial f_\ell} \right\} = \left(\frac{2}{N_0} \right) (r^2) \sum_{i=1}^N \sum_{j=1}^N \left(\frac{\partial \mu_{ij}}{\partial f_k} \right) \left(\frac{\partial \mu_{ij}}{\partial f_\ell} \right) \quad (6-20)$$

or,

$$E \left[\frac{\partial \Lambda_1}{\partial f_k} \cdot \frac{\partial \Lambda_1}{\partial f_\ell} \right] = \left(\frac{2}{N_0} \right) (r^2) \sum_{i=1}^N \sum_{j=1}^N \frac{\partial \left(\frac{\Delta T \cdot \text{Area (Pixel (i,j) on } \mathcal{M})}{r^2} \right)}{\partial f_k} \cdot \frac{\partial \left(\frac{\Delta T \cdot \text{Area (Pixel (i,j) on } \mathcal{M})}{r^2} \right)}{\partial f_\ell} \quad (6-21)$$

In order to obtain closed form results the following assumptions will be made:

$$(i) \quad \frac{\text{Area (Pixel (i,j) on } \mathcal{M})}{r^2} = \frac{1}{2} \quad (6-22)$$

for any pixel which is on the target boundary,

(ii) The number of pixels on the target

$$N_T \approx \frac{L_x L_y}{(r + \Delta)^2}, \quad (6-23)$$

(iii) The number of pixels in the target interior

$$N_I \approx \left(\frac{L_x}{(r + \Delta)} - 2 \right) \left(\frac{L_y}{(r + \Delta)} - 2 \right), \quad (6-24)$$

(iv) The number of pixels on the target boundary

$$N_B = N_T - N_I \quad (6-25)$$

or

$$N_B = \left(\frac{2}{r + \Delta} \right) (L_x + L_y - 2(r + \Delta)) \quad (6-26)$$

(v) The number of pixels on the target boundary parallel to the X-axis

$$N_{B_x} \approx 2L_x/(r + \Delta) \quad (6-27)$$

(vi) The number of pixels on the target boundary parallel to the Y-axis

$$N_{B_y} \approx 2L_y/(r + \Delta)$$

With these assumptions, the Fisher information matrix J has the form

$$J = \frac{1}{N_0} \begin{bmatrix} L_x L_y + 3(r + \Delta) - \frac{3(r + \Delta)}{2} (L_x + L_y) & 0 & 0 & \left(\frac{r}{r + \Delta}\right) \Delta T \cdot L_y / 2 & \left(\frac{r}{r + \Delta}\right) \Delta T \cdot L_x / 2 \\ 0 & 2(\Delta T)^2 L_y / (r + \Delta) & 0 & 0 & 0 \\ 0 & 0 & 2(\Delta T)^2 L_x / (r + \Delta) & 0 & 0 \\ \Delta T \cdot L_y / 2 & 0 & 0 & \frac{1}{2} (\Delta T)^2 L_y / (r + \Delta) & (\Delta T)^2 \\ \Delta T \cdot L_x / 2 & 0 & 0 & (\Delta T)^2 & \frac{1}{2} \frac{(\Delta T)^2}{(r + \Delta)} L_x \end{bmatrix}$$

For the special case where the samples are taken at r units apart ($\Delta = 0$)

$$\text{Var} (\hat{\Delta T} - \Delta T) \geq \frac{N_0}{2} \left(\frac{1}{a} - \frac{2 L_x L_y}{a r} \frac{(L_x + L_y - 4 ar)}{\left(\frac{1}{r^2} 2aL_y - L_y^2 r\right) \left(2aL_x - L_x^2 r\right) - (4a - L_x L_y)^2} \right)$$

$$\text{Var} (\hat{C}_x - C_x) \geq \frac{N_0}{4} \frac{r}{L_y \cdot \Delta T^2}$$

$$\text{Var} (\hat{C}_y - C_y) \geq \frac{N_0}{4} \frac{r}{L_x \cdot \Delta T^2}$$

$$\text{Var} (\hat{L}_x - L_x) \geq 2 \frac{N_0}{\Delta T^2} \frac{(2aL_y - L_y^2 r)}{\left[(2aL_x - L_x^2 r) (2aL_y - L_y^2 r) - (4a - L_x L_y)^2 \right]}$$

$$\text{Var} (\hat{L}_y - L_y) \geq 2 \frac{N_0}{\Delta T^2} \frac{(2aL_x - L_x^2 r)}{\left[(2aL_x - L_x^2 r) (2aL_y - L_y^2 r) \right]}$$

where

$$a = L_x L_y + 3r^2 - \frac{3r}{2} (L_x + L_y)$$

In order to compute probability of anomaly it will be assumed that the estimates of the target's size and location are constrained to be integer multiples of the pixels or detector size, r .

Then the likelihood given by Equation (6-17) reduces to

$$\Lambda = \frac{2r^2}{N_o} \sum_{i,j \in \text{target}} \sum \Delta T \left(I_s(x_i, y_i) - \frac{\Delta T}{2} \right) \quad (6-28)$$

Noting that

$$\widehat{\Delta T} = \frac{\sum_{i,j \in \text{target}} \sum I_s(x_i, y_i)}{N_*^2}$$

where

$$N_*^2 = \text{number of pixels on target}$$

one can then reduce Equation (6-28) to

$$\Lambda = \frac{r^2}{N_o} \left(\sum_{i,j \in \text{target}} \sum I_s(x_i, y_i) \right)^2 / N_*^2 \quad (6-29)$$

When the target detector (Equation (6-29)) is locked on the target, λ is defined to be

$$\lambda = \mathcal{E}(\Lambda)$$

$$= \frac{r^2}{N_o \left(\frac{L_x}{r + \Delta} \right) \left(\frac{L_y}{r + \Delta} \right)} \left[\left(\frac{L_x L_y}{(r + \Delta)^2} \right) \frac{N_o}{2r^2} + \left(\Delta T N_I + \left(\frac{\Delta T}{2} \right) N_B \right) \right] \quad (6-30)$$

which reduces to

$$\lambda = \left[\frac{1}{2} + \frac{\Delta T^2}{N_o} \cdot \frac{r^2 (r + \Delta)^2}{L_x L_y} \left(N_I^2 + N_I N_B + \frac{N_B^2}{4} \right) \right]$$

where N_B and N_I are given by Equation (6-24). For a region of N_*^2 pixels, the probability that this region will result in an anomaly is

$$P \left(\frac{\frac{r^2}{N_o} \left(\sum_{i,j} I_s(x_i, y_i) \right)^2}{N_*^2} \geq \lambda \right) = P(|z| \geq \sqrt{2\lambda})$$

$$= 2 \operatorname{erfc}_* (\sqrt{2\lambda})$$

The probability of anomaly is then obtained by applying the results from reference 1.

$$P(\text{anomaly}) \leq 2 \left(\frac{\text{FOV}}{r} \right)^2 \operatorname{erfc}_* (\sqrt{2\lambda})$$

Plots of error estimation bounds and probability of anomaly are given in Figure 6-1 for the special case of sampling at every r unit ($\Delta = 0$). Also included in the plots are the results obtained in reference 1 for segmentation of a rectangle which has been convolved with a blurring function. The close agreement between the two sets of plots for $\text{SNR} \geq 1.5$ suggest that for $\Delta = 0$, the blurring function previously used can also be used to model the effects of spatial quantization.

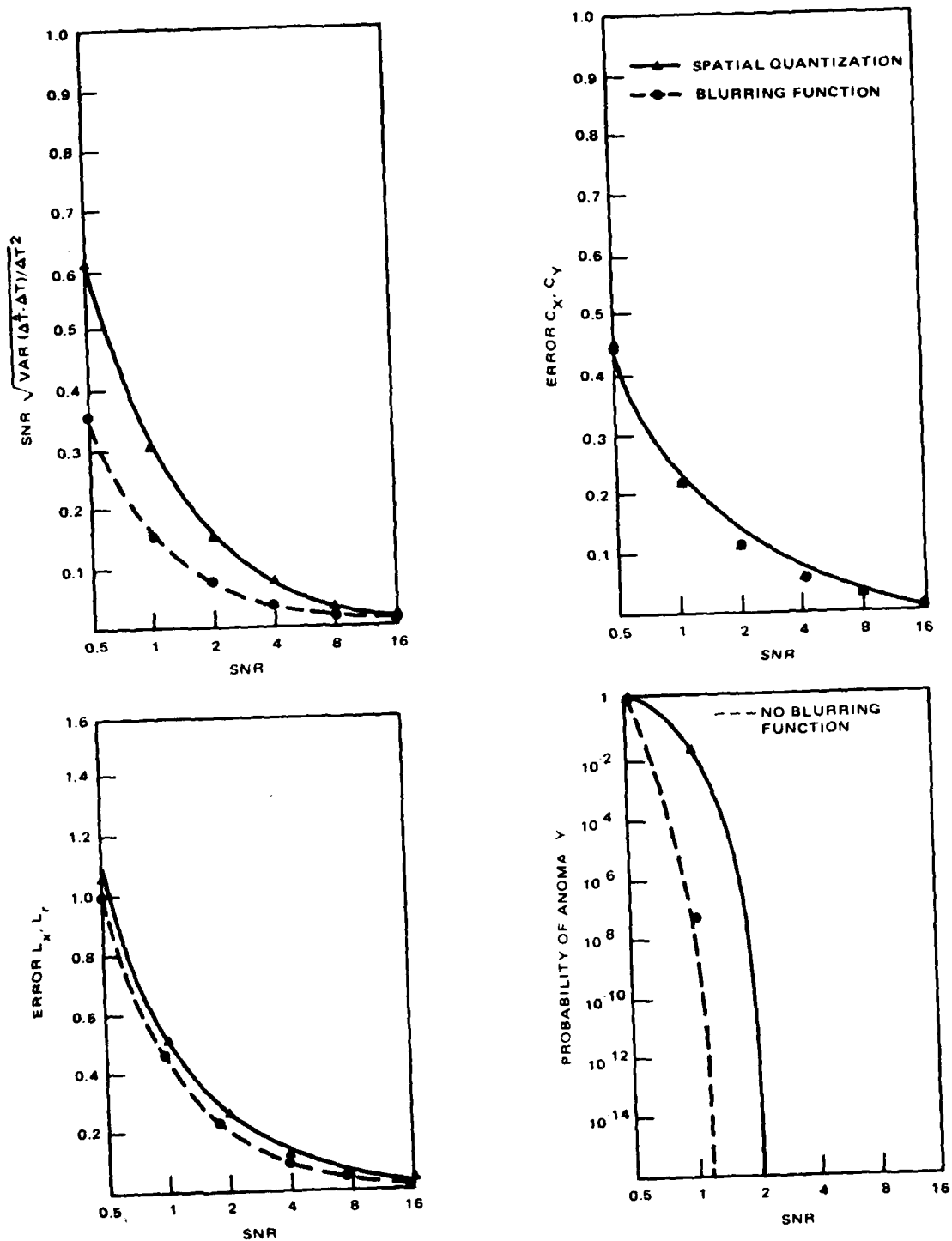


Figure 6-1. Effects of spatial quantization.

7.0 ANALYSIS OF ATAC SEGMENTATION

7.1 INTRODUCTION

The analyses presented in the preceding sections involved finding performance bounds for optimum object segmentation. In this section, analytic techniques are developed for the specific segmentor used in the ATAC Autocuer. There are two main steps in this segmentor: edge detection and interior point assignment.

The initial step in the ATAC segmentation routine is the generation of an edge value map within the window containing a region of interest. For this purpose, a Sobel operator of 3 x 3 pixels in size is used. It is assumed that the (Sobel) edge values corresponding to targets are among the largest edge values in the region of interest. As used in this algorithm, an object of interest is a contiguous area consisting of interior points. An interior point is defined as a pixel that is surrounded in most directions by edge points; and an edge point is defined as a point with an associated edge value which is above some threshold value.

Edge threshold value is determined adaptively using the average of edge values within the region of interest.

The rule is

$$T = K \cdot \bar{S}$$

where

T = the edge threshold

\bar{S} = the average Sobel operator value in the window

K = a constant of proportionality (typically 2.25)

In this manner the extraneous (not defining the boundary between target and background) edges are effectively discriminated against, since these have the greatest contribution to the determination of S. This edge thresholding technique is invariant to brightness and contrast variations in the image and has been shown to give a good target outline over a fairly wide variety of images.

Once the above threshold edge points have been determined, the detection of interior points within the region of interest takes place. The selection of an interior point can be easily visualized. Because an interior point is surrounded in most directions by an edge point, each pixel in the region of interest is tested for boundedness by edge points in eight directions given by:

$$\theta_n = \frac{n360^\circ}{8}, n = 1, \dots, 8 \quad (7-1)$$

If a pixel is bounded in 6 of the 8 directions by edge points, then that pixel is labeled to be interior to some boundary. The resultant image can then be thresholded at 6 (for 6 out of 8 directions) to produce the interior point image. A thinning and filling operation then removes isolated interior points and fills in gaps in the binary interior point image. The thinning and filling operator consists of a 3 x 3 pixel overlapping window, which is slid within the region of interest in both the x and y directions. If 5 out of 9 pixels in the 3 x 3 window are occupied by interior points, then the center element of this window is set to 1; otherwise, it is set to 0.

Because of the coarseness of the 8-direction edge point search, concave and convex portions of objects tend to be filled in, or shadowed; the same is true for regions between two objects which are in close proximity to each other. To overcome this drawback, an intensity assignment of interior versus exterior points is carried out.

To perform this function the mean and standard deviation of interior points (U_I, σ_I) and exterior points (U_E, σ_E) are computed. The assumption

is made that the distribution of interior and exterior intensities are approximately Gaussian. The desired threshold (between U_I and U_E) is then given by

$$T = \frac{U_E \sigma_I + U_I \sigma_E}{\sigma_E + \sigma_I} \quad (7-2)$$

If $U_E : U_I$ points $> T$ are selected, otherwise points $< T$ are selected. This enables both hot and cold targets to be segmented.

Following the intensity assignment, a determination is made (based on object area and standard deviation) whether to select the interior point sketch or the thresholded image as the best outline for the target.

Following this selection a final thinning and filling operation is performed, to eliminate isolated points and to fill in gaps.

Subject to the thinning and filling operation, a connectivity routine is used to identify distinct interior regions that are connected.

Finally, a comparison of the connected interior point regions thus derived is made with the original interior points in the interest window. Those areas having the most coincidence of interior points with edge points are designated as segmented objects, and its corresponding original intensity values are substituted into the segmented objects. Depending on the scenario expected in the images, one or more of the segmented objects within the interest window can be tagged as likely objects. After this stage, a calculation is made (based on area and object center) to see if it is likely that portions of the desired target lie outside the interest window. If so, the window is repositioned and segmentation recomputed. Finally, the segmented objects are passed on to the high level feature extractor for classification.

A statistical model for this operation and its performance was developed for a simple scene corrupted by noise. Then an analytic procedure for finding the probability of gaps occurring within an edge segment was developed and verified experimentally. The occurrence of gaps is important since the interior point assignment depends on finding points surrounded by edges. A model is then presented for interior point assignment, the selection of interior point threshold, and performance results.

7.2 EDGE ANALYSIS

As stated in Section 2, a simple model of the image is used to develop the basic analytic results. Since the ATAC segmentor operates on a window containing an object, the model for the scene is a window $N \times N$ pixels in size with a background level of zero average intensity. The object is presented by an $m \times m$ pixel square with uniform average intensity ΔT , centered in the window. The entire window is assumed corrupted by Gaussian noise of zero mean and variance σ^2 .

The first step is to determine the distribution of edges as determined by the edge operator, in this case the Sobel edge operator, defined by the equations:

$$S(x, y) = |S_H(x, y)| + |S_V(x, y)| \quad (7-3)$$

where

$$\begin{aligned} S_H(x, y) = & I(x-1, y-1) + 2I(x, y-1) + I(x+1, y-1) \\ & - I(x-1, y+1) - 2I(x, y+1) - I(x+1, y+1) \end{aligned} \quad (7-4)$$

and

$$\begin{aligned} S_V(x, y) = & I(x-1, y-1) + 2I(x-1, y) + I(x-1, y+1) \\ & - I(x+1, y-1) - 2I(x+1, y) - I(x+1, y+1) \end{aligned} \quad (7-5)$$

Here $I(x, y)$ represents the intensity of the pixel with coordinates x and y .

The average values for $S_H(x, y)$ and $S_V(x, y)$ are zero for pixels inside or outside the boundary, but not for pixels adjacent to it.

For pixels adjacent to the boundary of the object, either inside or outside,

$$E(S_H(x, y)) = \pm 4 \Delta T \quad (7-6)$$

and

$$\epsilon(S_V(x, y)) = \pm 4 \Delta T \quad (7-7)$$

where ϵ denotes the expectation operator.

If the variation from the mean is defined as

$$\Delta S_H(x, y) = S_H(x, y) - \epsilon(S_H(x, y)) \quad (7-8)$$

it is easy to show that the variance of $S_H(x, y)$ equals $12\sigma^2$. That is,

$$\epsilon \left[\Delta S_H(x, y) \right]^2 = 12\sigma^2 \quad (7-9)$$

A similar result applies to $S_V(x, y)$. Furthermore, $\Delta S_H(x, y)$ and $\Delta S_V(x, y)$ are uncorrelated, i.e.,

$$\epsilon \left[\Delta S_H(x, y) \Delta S_V(x, y) \right] = \sigma^2 - \sigma^2 - \sigma^2 + \sigma^2 = 0 \quad (7-10)$$

For non-boundary pixels, the probability $P_N(T)$ that a pixel intensity does not exceed a given threshold value T is given by

$$P_N(T) \stackrel{d}{=} \int_0^T P_{S(x, y)}(u) du \quad (7-11)$$

where the probability density function $P_{S(x, y)}$ can be shown (using NBS Handbook of Mathematical Functions 7.4.32, P303) to be

$$P_{S(x, y)}(u) = \frac{2}{\sqrt{\pi g}} e^{-\frac{u^2}{4g}} \operatorname{erf} \left(\frac{u}{2g} \right) \quad (7-12)$$

where the error function is defined as

$$\text{erf}(z) \triangleq \frac{2}{\sqrt{\pi}} \int_0^z e^{-u^2} du \quad (7-13)$$

and

$$\underline{\sigma}^2 = 12 \sigma^2$$

Then

$$P_N(T) = \left[\text{erf} \left(\frac{T}{2\underline{\sigma}} \right) \right]^2 \quad (7-14)$$

and the probability of a detecting a false edge is given by

$$P_F = \int_T^\infty P_{S(x,y)}(u) du \approx 1 - \left[\text{erf} \left(\frac{T}{2\underline{\sigma}} \right) \right]^2 \quad (7-15)$$

Also, the mean value for non-boundary pixels is given by

$$\begin{aligned} \bar{U} &= \int_0^\infty u P_{S(x,y)}(u) du \\ &= 2\sqrt{\frac{2}{\pi}} \underline{\sigma} = 4\sqrt{\frac{6}{\pi}} \sigma . \end{aligned} \quad (7-16)$$

Appendix B gives the analysis for boundary pixels. It is shown there that the probability for an edge pixel being detected is given by

$$P_D = \int_T^\infty P_{S(x,y)}(u) du \quad (7-17)$$

$$= 1 - \frac{1}{4} \left[\text{erf} \left(\frac{T + 4\Delta T}{2\underline{\sigma}} \right) + \text{erf} \left(\frac{T - 4\Delta T}{2\underline{\sigma}} \right) \right]^2 \quad (7-18)$$

where the probability density function for this case is given by

$$P_{S(x, y)}(u) = \frac{1}{2\sqrt{\pi}\sigma} \left[e^{-(u+4\Delta T)^2/4\sigma^2} + e^{-(u-4\Delta T)^2/4\sigma^2} \right] \cdot \left[\operatorname{erf} \left(\frac{u+4\Delta T}{2\sigma} \right) + \operatorname{erf} \left(\frac{u-4\Delta T}{2\sigma} \right) \right] \quad (7-19)$$

Note that Equation (7-18) for P_D reduces to Equation (7-15) for P_F when $\Delta T = 0$. Similarly, the probability density function with an edge present, Equation (7-15), reduces to the no-edge distribution when $\Delta T = 0$.

Curves of the no-edge distribution and edge distribution for two signal-to-noise ratios are given in Figure 7-1. Also shown is a displaced Gaussian approximation to one of the curves. It is seen that an excellent approximation is obtained even though the signal-to-noise ratio is not extremely large. The displaced Gaussian approximation is derived in Appendix C, where it is shown that the mean intensity for an 'edge pixel' is given by (for sufficiently large ΔT)

$$\bar{S} = 4\Delta T + \sqrt{\frac{2}{\pi}} \sigma \quad (7-20)$$

with a variance given by

$$\sigma_2^2 = 2 \left(1 - \frac{1}{\pi} \right) \sigma^2 \quad (7-21)$$

as before.

The second term in Equation (7-20) shows that the presence of noise causes the average value to shift from its value $4\Delta T$ in the absence of noise. This is a consequence of the non-linearity of the Sobel operator.

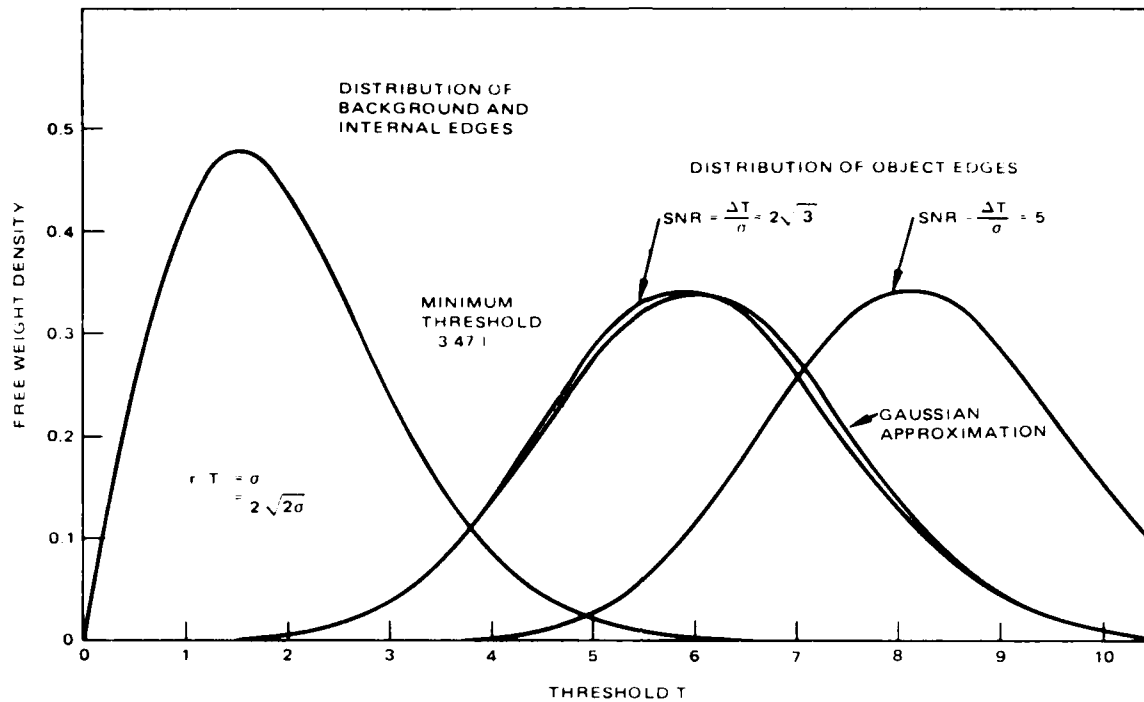


Figure 7-1. Distribution of background and object edges.

From Eq. (7-16), the mean value of the background and interior pixel is $4\sqrt{\frac{6}{\pi}} \sigma$, while from Eq. (7-20) the mean value of the edges on the object boundary is $4\Delta T + 2\sqrt{\frac{6}{\pi}} \sigma$. The Sobel operator will produce two edges for each true edge in the picture, hence the average value of the edge is

$$\bar{S} = 4\sqrt{\frac{6}{\pi}} \sigma + \frac{16m}{N^2} \left(2\Delta T - \sqrt{\frac{6}{\pi}} \sigma \right) \quad (7-22)$$

The edge threshold chosen is $K\bar{S}$ where $K = 2.25$, therefore as a minimum

$$T > 9\sqrt{\frac{6}{\pi}} \sigma \quad (7-23)$$

so that by evaluating Eq. (7-15), the probability that a background pixel is incorrectly labeled as an edge is given by

$$P_F \leq 0.022. \quad (7-24)$$

The probability P_D that a boundary pixel is correctly labeled is evaluated using Eq. (7-18) where the threshold is given by

$$T = 2.25 \bar{S} \quad (7-25)$$

P_D is plotted in Figure 7-2 for three values of target size.

In order to determine the adequacy of the Sobel operator in extracting the square boundary in the presence of noise, more needs to be known than the probability P_D that a given edge pixel is detected. Although P_D may be high, the probability P_{AD} that all edge pixels in the square are detected,

$$P_{AD} \approx (P_D)^{8m} \quad (7-26)$$

is smaller the larger the number of boundary pixels.

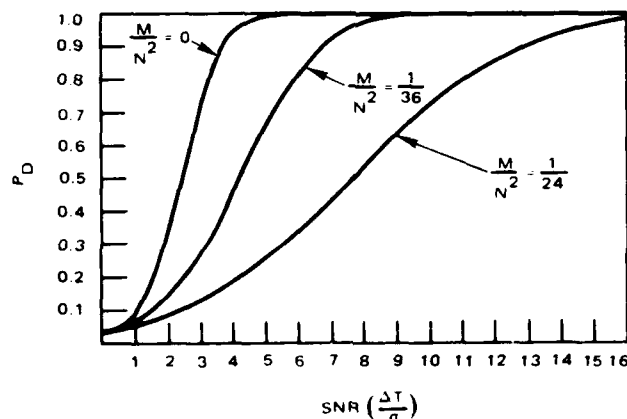


Figure 7-2. Plot of edge detection probability vs. SNR for different target sizes.

Fortunately, it is not necessary to detect all edge pixels for adequate segmentation since a later operation may still correctly separate interior and exterior pixels. Obviously the least serious case is where only a single edge pixel goes undetected, but its neighbors are detected. Examples of this are shown as A and B in Figure 7-3. (To avoid unnecessary computation, corner pixels such as C and D are excluded from the analysis since their values in the absence of noise are $6\Delta T$ and $2\Delta T$, respectively, compared with the other edge pixels whose values are $4\Delta T$. Also, the correlation with their neighbors is different for the corner pixels.)

The next most serious case is where a pair of neighboring edge pixels goes undetected. Examples of this are given in E, F, and G. The case of G must be distinguished from that of E and F since G causes a gap

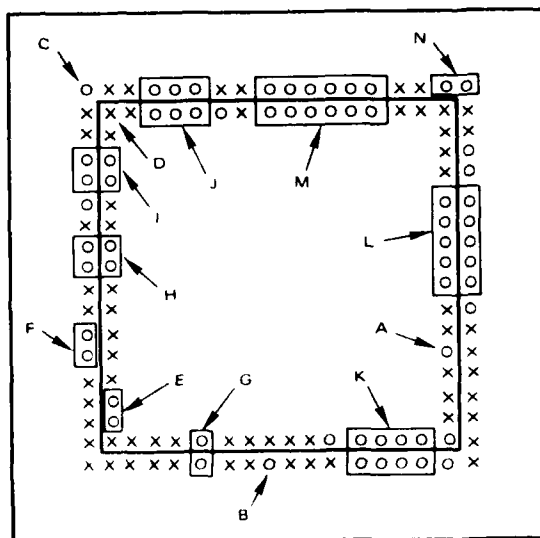


Figure 7-3. Cases of interest for gap analysis.

in the boundary while E and F don't. (Again, case N is excluded from our analysis since it involves a corner pixel.) We will call G a first-order gap.

Cases H and I are second-order gaps, while J, K, L, and M are third-, fourth-, fifth-, and sixth-order gaps, respectively. (Note that case K is not considered a fifth-order gap since the corner pixel is excluded from our analysis. Note also that a gap of given order also, in a sense, contains gaps of lower order.)

Before beginning the analysis three more terms should be defined: "point", "gap point", and "non-gap point". A point is a pair of neighboring pixels lying directly across the boundary from each other. A "gap point" is a point, both of whose pixels are below the threshold for edge detection. A non-gap point is a point which is not a gap point. An nth-order gap is then formally defined as 'n' adjacent gap points.

A key probability that is needed is the probability $P_G(n)$ of an nth order gap occurring in n specific adjacent points. By excluding corners from gaps, this probability is the same for all possible n adjacent points in the square. For a square of length m there are $4(m-n-1)$ such configurations where an nth-order gap can occur. Defining $P_D(n)$ as the probability of detecting a square not containing any nth order gaps (or larger), clearly

$$P_D(n) = (1 - P_G(n))^{4(m-n-1)} \quad (7-27)$$

The value of n to be chosen will in general depend upon the size of the square m, as well as the effectiveness of subsequent operations in the segmentation process in filling in gaps.

To obtain a formula for $P_G(n)$, define the conditional probability P_{GC} as the probability that by extending an nth-order gap to its neighboring point an $(n+1)^{th}$ -order gap occurs.

$$P_G(n+1) = P_G(n) P_{GC} . \quad (7-28)$$

In general P_{GC} also will depend upon n . However making the assumption that the correlation is small and these can be neglected, P_{GC} will be independent of n . Experimental results discussed below, as well as theoretical calculations of correlation coefficients, suggest that this is a valid assumption. In Appendix F, the Sobel operator correlation coefficient between next-nearest neighbors along the boundary is found to be only 0.18 compared with the value of 0.49 found in Appendix D for nearest neighbors. This high value for nearest neighbor enhances the likelihood of occurrence of high-order gaps over what would occur if there were no correlations.

In Appendix E, the correlation coefficient for pixels across the boundary is found to be only 0.11. Consequently, the probability of non-detection for this case is given to good approximation by Eqs. (E27) and (E28)

$$P_{2S} = P_N^2 = (1 - P_D)^2, \quad (7-29)$$

where P_N is the probability of not detecting any specified edge pixel. From its definition, P_{2S} is the probability of a first-order gap.

$$P_G(1) = P_{2S} \quad (7-30)$$

with repeated application of (7-28),

$$P_G(n) = P_{2S} (P_{GC})^{n-1} \quad n \geq 1. \quad (7-31)$$

The conditional probability P_{GC} is obtained by specializing to the case $n = 2$,

$$P_{GC} = \frac{P_G(2)}{P_{2S}} \quad (7-32)$$

Since neighboring pixels across the boundary are nearly uncorrelated, it is reasonable to assume that the same is true for boundary-parallel pairs of such pixels.

$$P_G(2) = (P_{2P})^2 \quad (7-33)$$

where P_{2P} is the probability of non-detection for a parallel-to-the-boundary pair. In Appendix D, it is shown how P_{2P} is calculated from certain graphed integrals of the bivariate normal probability function.

Substituting (7-33) and (7-29) into (7-32), one obtains

$$P_{GC} = \left(\frac{P_{2P}}{P_N} \right)^2 \quad (7-34)$$

Having calculated P_{GC} , $P_G(n)$ may be calculated from (7-28) or (7-31)

Having calculated $P_G(n)$, $P_D(n)$ may be calculated from Eq. (7-27).

Experiments were conducted to verify the analytic techniques using computer simulation.

Ten Monte Carlo experiments were run for each of two target/window sizes:

1. A 16 pixel square in a 24 pixel window,

$$M/N^2 = 16/24^2 = 1/36;$$

2. A 6 pixel square in a 12 pixel window

$$M/N^2 = 6/12^2 = 1/24.$$

Experimental averages and standard deviations obtained are tabulated in in Table 7-1. It may be seen that the agreement with theory is quite good. In all cases the difference between theory and experiment is well within the standard deviation. The standard deviations are generally larger for the $M/N^2 = 1/24$ case since fewer sample points were involved. For the same reason, the percent standard deviation becomes larger for higher gap size.

TABLE 7-1. THEORETICAL AND EXPERIMENTAL VALUES FOR SNR = 4.
EXPERIMENTAL VALUES ARE RESULTS OF 10 MONTE CARLO
SIMULATIONS RUN FOR EACH TARGET SIZE

	$M/N^2 = 1/36 (= 16/24^2)$		$M/N^2 = 1/24 (= 6/12^2)$	
	Theory	Experiment	Theory	Experiment
\bar{S}	84.68	84.04 ± 2.54	99.14	98.18 ± 5.72
T	190.53	189.0 ± 5.36	223.06	220.8 ± 12.58
P_N	0.53	0.53 ± 0.08	0.81	0.79 ± 0.06
P_{2P}	0.36	0.34 ± 0.07	0.70	0.65 ± 0.12
P_{2S}	0.28	0.26 ± 0.06	0.66	0.59 ± 0.13
$P_G(2)$	0.13	0.12 ± 0.05	0.49	0.43 ± 0.18
$P_G(3)$	0.06	0.05 ± 0.03	0.37	0.33 ± 0.21
$P_G(4)$	0.03	0.02 ± 0.03	0.27	0.23 ± 0.22
$P_G(5)$	0.01	0.01 ± 0.02	0.20	—
$P_G(6)$	0.006	0.003 ± 0.009	0.15	—

Note that the experimental averages exhibit a bias, since all of them are less than or equal to the theoretical values. The probable explanation for this behavior is that, due to chance, the average experimental intensity \bar{S} was (for both cases) smaller than the theoretical value. Since the threshold for each experiment was set at 2.25 times the average intensity for that experiment, the average threshold was also smaller than the theoretical value. (Note, however, that due to large roundoff error, due to use of integer intensities, the experimental averages and standard deviation for T do not exactly equal 2.25 times the corresponding values for \bar{S} .) Since a lower threshold increases the probability of edge detection, and thus decreases the probability of non-detection, the experimental average probabilities will be expected to be below their theoretical values. It is likely that even better agreement with theory could be obtained if the a posteriori average thresholds of Table 7-1 were used in making the theoretical calculations of probabilities.

Table 7-2 indicates the method of calculating the various probabilities using the case of the assumed edge detection of the 16 x 16 square in Figure 7-3 as an illustrative example. The interested reader may check that the number of sample points and number of occurrences is correct for each case. Note that corner pixels have been excluded from consideration.

In Table 7-3 are tabulated experimental and theoretical values of $P_D(n)$, the probability of detecting a square containing no n th-order (or higher) gap for $\text{SNR} = 4$ and object size $M/N^2 = 1/36$. The theoretical values have been calculated from Eq. (7-27), while the experimental values are based upon the 10 computer runs. The results are satisfactory in view of the small sample size. Again, the tendency of the experimental $P_D(n)$ to exceed the theoretical value is likely attributable to the bias in the threshold which caused fewer gaps of a given order to be generated, and thus increases the probability that a square would have no gap of this order.

Obviously, it would be desirable to make more computer runs to improve the statistics, and to make calculations for other SNRs of interest.

7.3 INTERIOR POINTS

The second major operation in the ATAC segmentor is the detection or assignment of object interior points. Again, the simple scene model of Figure 7-4 is used.

Assume for the object shown in Figure 7-4 that due to SNR reasons the probability of an edge point being correctly labeled is P_D and the probability for a nonedge point being incorrectly labeled is P_F . Then the probability that a point interior to the object is surrounded by edges in at least 6 out of 8 directions is bounded by

$$P_{6/8} \leq 8 P_D^7 (1 - P_D) + \binom{8}{2} P_D^6 (1 - P_D)^2 + P_D^8 \quad (7-35)$$

A plot of this function versus P_D is shown in Figure 7-5.

For the probability that a point non-interior to the surface being labeled an interior point consider the situations described in Figure 7-6.

TABLE 7-2. TABLE ILLUSTRATING CALCULATION OF PROBABILITIES
BASED UPON FIGURE 7-3

Probability Calculated	Number of Sample Points	Number of Occurrences	Result
P_N	120	60	0.5
P_{2P}	112	38	0.34
P_{2S}	56	23	0.41
$P_G(2)$	52	16	0.31
$P_G(3)$	48	10	0.21
$P_G(4)$	44	6	0.14
$P_G(5)$	40	3	0.075
$P_G(6)$	36	1	0.03

TABLE 7-3. EXPERIMENTAL AND THEORETICAL RESULTS FOR $P_D(n)$,
THE PROBABILITY OF DETECTING A SQUARE CONTAINING NO NTH-
ORDER GAP, FOR SNR = 4 AND $M/N^2 = 1/36$ (EXPERIMENTAL VALUES
BASED UPON 10 MONTE CARLO SIMULATIONS.)

n	No. of Squares Having No nth-Order Gap	$P_D(n)$	
		Experimental	Theoretical
1	0	0	10^{-10}
2	0	0	0.0007
3	2	0.2 ± 0.4	0.04
4	5	0.5 ± 0.5	0.2
5	8	0.8 ± 0.4	0.5
6	9	0.9 ± 0.3	0.7
7	10	1	0.9

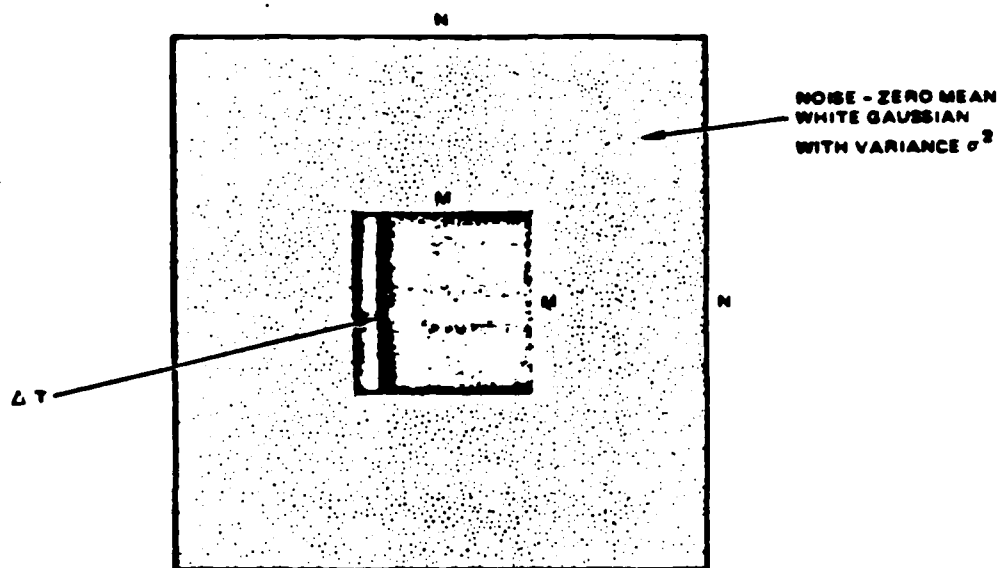


Figure 7-4. Simplified model for object in noisy background.

Case 1 – Point on the Outer Boundary of Object

In this case, the point is already surrounded by 5 directions as shown in Figure 7-6. For a 6th direction to be found one point in the remaining 3 directions must be found. This will be bounded by

$$P_{\text{CASE 1}} = 1 - (1 - P_i)^{(N/2) \times 3} \quad (7-36)$$

Using $N = 25$ and $P_i = 0.02$ from (7-6) this yields approximately 51 percent.

Case 2 – Point Outside the Outer Boundary but Closer than m Pixels to the Object

Here the pixel is surrounded in three directions, to be labeled as an interior point it must be surrounded by at least three in the remaining five directions – this is bounded by

$$P_{\text{CASE 2}} = \binom{5}{3} \alpha^3 (1 - \alpha)^2 + \binom{5}{4} \alpha^4 (1 - \alpha) + \alpha^5 \quad (7-37)$$

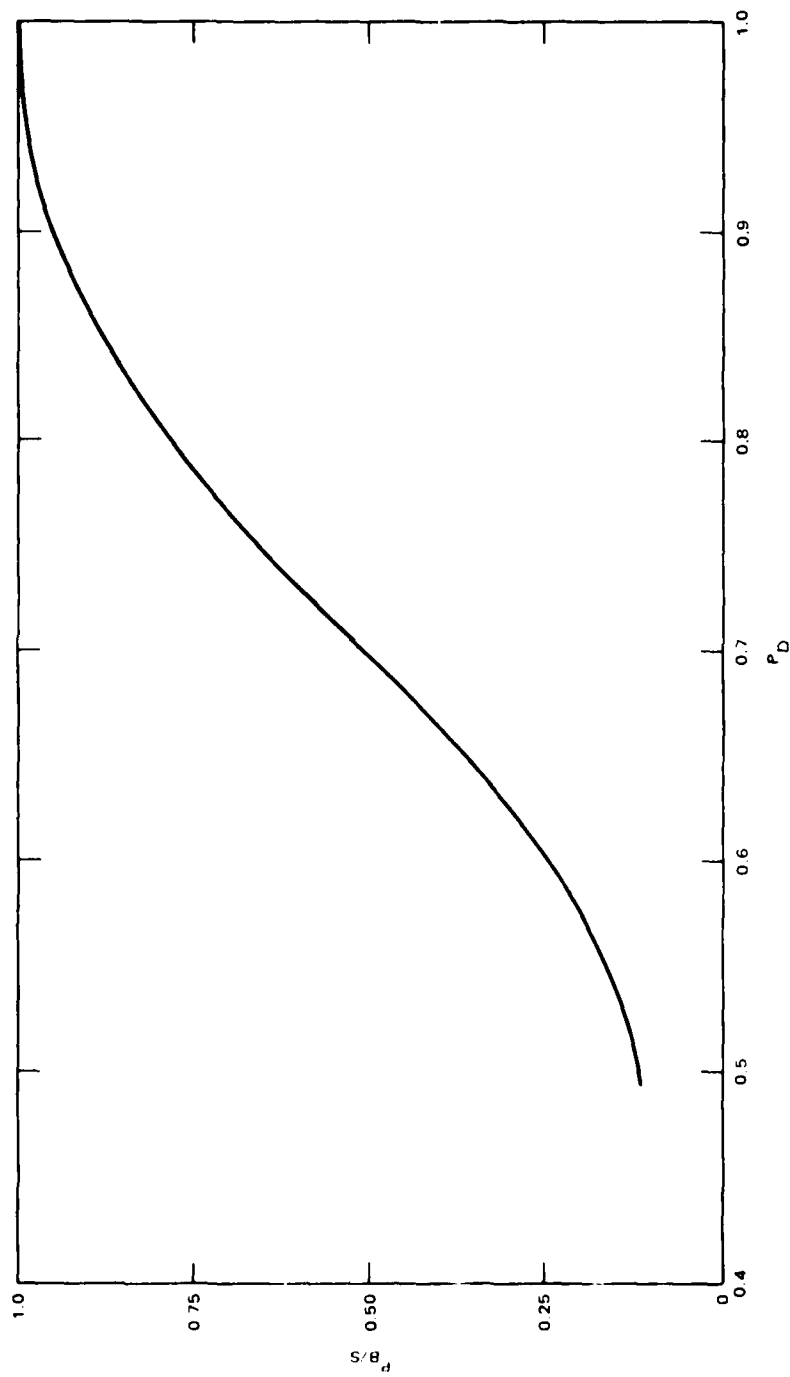


Figure 7.5. Probability of correct labeling of interior point as a function of edge detection probability.

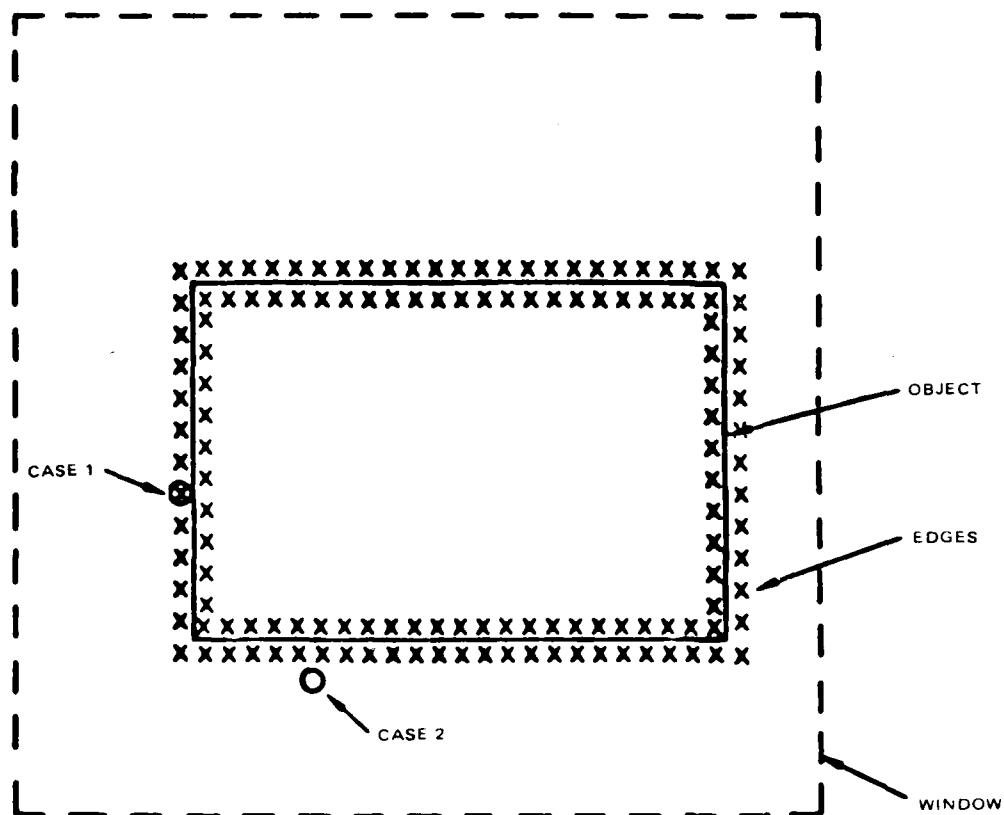


Figure 7-6. Cases of interest for interior point analysis.

where

$$\alpha = 1 - (1 - P_f)^{N/2} = 0.22 \quad (7-38)$$

Therefore (7-37) evaluates to 0.07.

Case 3 - Point Far Removed from Outer Boundary

Here point is surrounded by one direction from object and so must have edge points in five of the remaining seven directions. This is bounded by

$$P_{\text{CASE 3}} \leq \binom{7}{5} \alpha^5 (1 - \alpha)^2 + \binom{7}{6} \alpha^6 (1 - \alpha) + \alpha^7 \quad (7-39)$$

which evaluates to 0.006 for P_f given by (7-24).

The thinning operation, which requires 5/9 adjacent cells to be interior points prior to assigning an interior point will therefore remove virtually all of the misassigned points in Cases 3 and 2, and will remove the majority of the points assigned in Case 1.

Intensity Assignment

From the preceding discussion, the measured interior point average intensity will be*

$$\frac{\Delta T \times m^2 + 0 \times (4m + 4)}{(m + 2)^2} \quad (7-40)$$

$$I_{\text{INTAV}} = \Delta T \left(\frac{m}{m + 2} \right)^2 \quad (7-41)$$

The measured exterior point average will be

$$I_{\text{EXTAV}} = 0 \quad (7-42)$$

The measured exterior point standard deviation will be fairly close to

$$\sigma_{\text{EXT}} = \sigma \quad (7-43)$$

And the measured interior point standard deviation will be

$$\sigma_{\text{INT}} = \sigma \sqrt{1 + \left(\frac{m}{m + 2} \right)^2 \left[1 - \left(\frac{m}{m + 2} \right)^2 \right] \frac{\Delta T^2}{\sigma^2}} \quad (7-44)$$

* This assumes that all of the boundary points are Case 1 points and not removed by thinning.

The selected threshold will be

$$T = \frac{\sigma_{EXT} \left(\frac{m}{m+2} \right)^2}{\sigma_{INT} + \sigma_{EXT}} = \frac{\Delta T}{2} \cdot \frac{\eta}{\frac{1}{2} \left(1 + \sqrt{1 + \eta(1 - \eta) \frac{\Delta T^2}{2}} \right)} \quad (7-45)$$

where

$$\eta = \left(\frac{m}{m+2} \right)^2 \quad (7-46)$$

is a function of object size. In practice when $m < 8$, (resulting in small η), the interior points picture is selected. As $\eta \rightarrow 1$ this threshold approaches the optimal threshold of $\Delta T/2$. As the SNR ($\Delta T/\sigma$) is increased, the chosen threshold becomes increasingly tolerant (lower), allowing more weight to the inclusion of object points than to the exclusion of unwanted noise points, since these will be cleaned up in later thinning and connectivity stages.

Following the selection of the threshold, the window is passed through this threshold. Depending on SNR this threshold will determine the P_{CO} = Probability of correct assignment of object points and P_{CB} = probability of correct assignment of background points. A plot of these probabilities is shown in Figure 7-7. For a connected object to maintain its proper shape to within 5 percent, $P_{CO} > 0.95$ and $P_{CB} \geq 1 - 1/2 m$ (for few unwanted points to exist on the boundary of the extracted object) the curves of Figure 7-7 show an SNR requirement of about 5 for $T = \Delta T/2$ and $m = 10$. This requirement is consistent with the requirements on the other stages of this process.

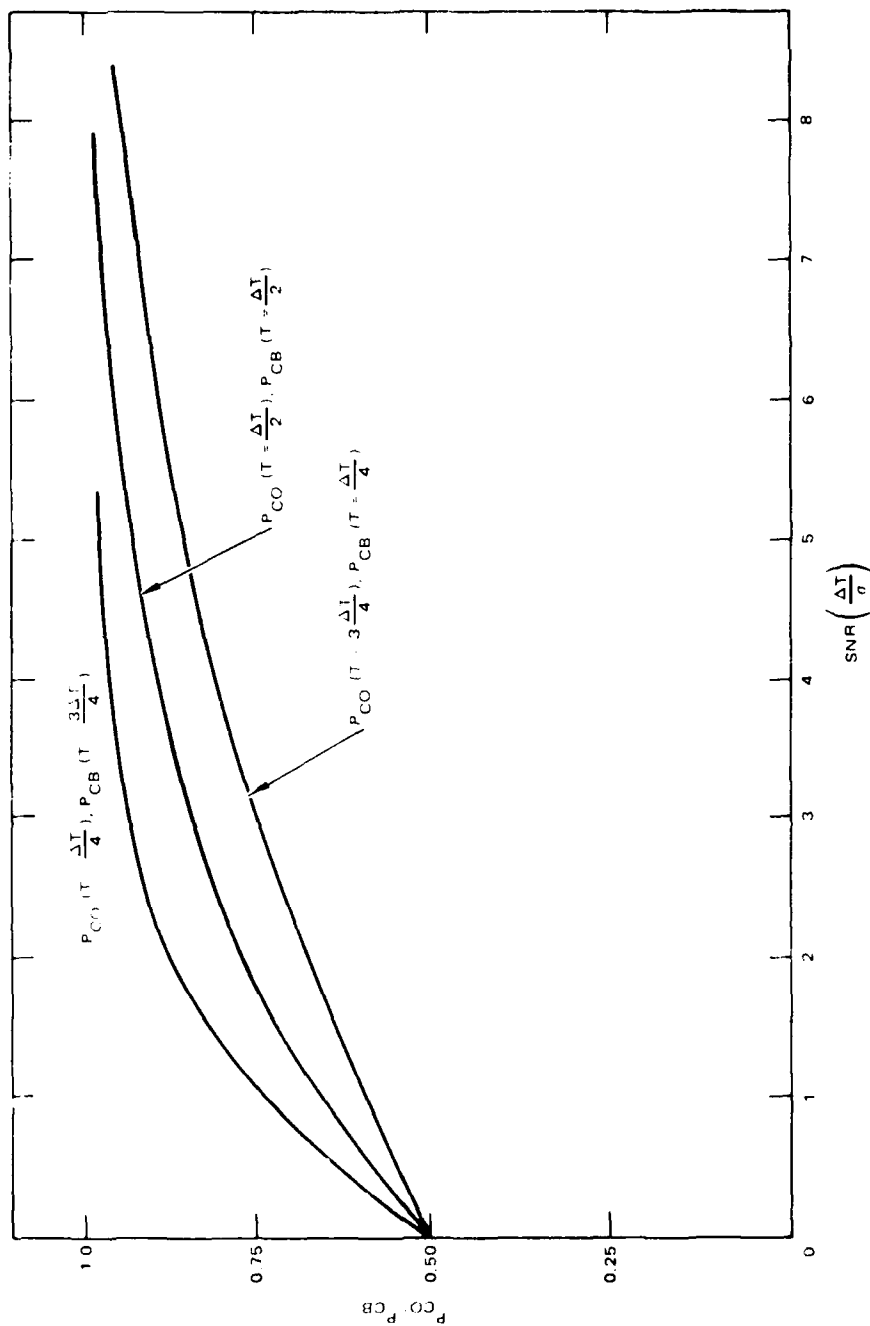


Figure 7-7. Probability of correct assignment of object points (P_{CO}) and probability of correct assignment of background points (P_{CB}) as a function of signal to noise ratio (SNR).

7.4 SUMMARY AND CONCLUSIONS

Of course, if the only problem were to extract the shapes of simple objects in idealized backgrounds such as that illustrated in Figure 7-4, there would be a number of simpler techniques which would be capable of performing an effective segmentation. The techniques described here, are, however, applicable over a wide range of circumstances encountered in actual IR images and not described by the model of Figure 7-4. It is the purpose of this analysis, however, to show in broad terms the noise sensitivity of the algorithms that are employed.

8.0 CONCLUSIONS AND RECOMMENDATIONS

An analytic modeling approach for image processing algorithms has been developed and applied to the complex object segmentation operation used for automatic target classification/recognition in FLIR images.

Starting with a simple scene model, performance bounds were defined for the segmentation operation and analytic means for evaluating these bounds were developed. A technique was developed to extend these results to more complex scenes involving more detailed target shapes and presence of simple clutter, while maintaining the tractability of the analytic evaluation of performance bounds. These results will provide the means for obtaining useful analytic results for several problems. First the performance of a specific segmentation algorithm on images with noise and simple clutter can be compared with the performance bounds to determine if that segmentor is performing as well as can be expected or is deficient in some respect, e.g., in responding to noise or the presence of clutter.

The analytic techniques can be used to extend the complexity of target and clutter description to find the degree of complexity necessary for good analytic results and the important descriptive features for the particular image processing operation considered. This approach can be used, e.g., to find a relatively simple analytic model of a particular FLIR image that can predict segmentor performance analytically, without the statistical uncertainties of testing a segmentor on a small number of images.

The use of these performance bounds also will allow the specification of maximum permissible system noise characteristics for achieving a specified segmentation performance.

In continuation of this effort it is recommended that the previous results be extended with the goal of establishing and verifying analytic models for the performance of target recognition and tracking systems.

The recommendations are divided into 5 primary tasks. Task I, denoted "Image Modeling" will extend image models to include 3-dimension effects and improve the clutter models. Task II, denoted "Tracker Modeling" will extend the models to include Target Tracking Systems. Task III, denoted "Performance Analysis" will involve derivation of improved performance bounds for target recognizers and trackers and extension of these bounds to include clutter limited performance. Task IV, denoted "Context Modeling" will develop methods for use and analysis of non-silhouetted information, e.g., wheels, treads, engines. Task V, denoted "Image System Modeling" will apply the modeling philosophy and the results of the previous tasks to specifically model a target recognizer and a target tracker.

Specifically, in Task I:

1. Derive complete 3-D target models
2. Derive improved 3-D clutter models
3. Model shape recognition for 2-D projections of 3-D objects.
4. Generate synthetic 2-D scene models for use in performance analysis.

In Task II:

1. Characterize Target Trackers
2. Develop analytic models for Target Trackers
3. Verify the models using simulation

In Task III:

1. Derive improved performance bounds for target recognizers
2. Derive performance bounds for Target Trackers
3. Extend our performance bound approach to include clutter limited (as opposed to noise limited) effects
4. Establish the limiting factors on target tracker performance
5. Develop analytical means of predicting performance of trackers and recognizers

In Task IV:

1. Derive models for typical target contextual parts: wheels, treads, engines
2. Establish a model for use of contextual information, both individually and synergistically
3. Develop performance models for the use of this information in target recognition.

In Task V:

1. Implement a target recognizer model using the image meta-model philosophy
2. Implement a target tracker with the meta-model
3. Verify the accuracy of the models implemented in (1) and (2), above.

APPENDIX A

New approach to FLIR segmentation

Lawrence M. Rubin and Richard L. Frey

Electronics Department, Hughes Aircraft Company
Culver City

Abstract

An approach to the analysis of shape extraction (segmentation) operators is presented based on maximum likelihood parameter estimation. A simple image model is presented and objective measures of segmentation quality are presented. Bounds on the noise performance of any segmentation operator are derived and these are compared with experimental results obtained on sample images.

Introduction

In systems requiring pattern recognition techniques to be applied to imagery such as that generated by Forward Looking Infra-Red (FLIR) sensors, a critical stage is often the extraction of object shapes from the scene. These shapes can then be measured and the resulting features applied to a classifier for such processes as automatic recognition of targets. A variety of algorithms have been developed to perform this shape extraction function¹⁻⁴. These algorithms usually employ such techniques as edge detection, intensity thresholding, and some type of connectivity criteria to obtain their estimate of object shape. In general these algorithms are heuristic in nature and typically their performance is judged subjectively. Factors such as noise sensitivity are usually not brought into play in the evaluation of these techniques. Useful analytic results pertaining to these algorithms are difficult to obtain, due to both the difficulty in modelling realistic scenes and the intractability of the algorithms themselves. This paper will attempt to study segmentation algorithms on a slightly more formal basis, using results obtained from maximum likelihood parameter estimation theory. A simple image model will be utilized, and the effectiveness of a segmentation procedure will be gauged in terms of its accuracy in estimating the parameters of the model. Bounds will be derived on the performance of an optimal procedure and these bounds will be compared to the performance obtained from several simulations of other segmentation procedures.

Image model

The model that we will employ to represent sample images is illustrated in Figure 1. We use continuous coordinates in both x and y directions.

$g(x, y)$ is used to represent the intensity distribution of the image

$$g(x, y) = b(x, y) + s(x, y) + n(x, y) \quad (1)$$

$$0 \leq x, y \leq R$$

where $b(x, y)$ represents the background intensity $b(x, y) = b$.

$$s(x, y) = \Delta T \cdot S_1(x) \cdot S_2(y) \quad (2)$$

$$S_1(x) = \text{rect}(x - C_x, L_x) \otimes \text{rect}(x, r) \quad (3)$$

and

$$S_2(y) = \text{rect}(y - C_y, L_y) \otimes \text{rect}(y, r) \quad (4)$$

where \otimes indicates convolution

$$\text{rect}(x, r) = \begin{cases} 0 & |x| \geq r/2 \\ 1 & |x| \leq r/2 \end{cases} \quad (5)$$

(C_x, C_y) is the center of the object rectangle and L_x, L_y is the length of the rectangle in the x and y directions respectively. r represents a spatial band limiting process applied to the image (see Figure 2). ΔT represents the intensity amplitude of the rectangle and $n(x, y)$ represents a stationary, zero mean Gaussian spatially white process such that

$$E[n(x, y), n(x + x_1, y + y_1)] = \frac{N_0}{2} \times u_0(x_1, y_1) \quad (6)$$

where $u_0(\cdot, \cdot)$ is a two dimensional impulse function.

Performance bounds

We state the segmentation problem as follows: Given an observation of $g(x, y)$, estimate the center, size, intensity and shape of the rectangle. We will treat the parameters C_x, C_y, L_x, L_y , and ΔT as non-random; that is to say with no prior known underlying probability distribution.

Under these circumstances the problem reduces to a multi-parameter estimation problem and results relating to the bounds on performance of such an estimate are well known⁷. These results will be repeated below:

Let $g(x, y) = s(x, y, \underline{F}) + n(x, y)$ (7)
 where \underline{F} is a vector of parameters $\underline{F} = [f_1, f_2, \dots, f_k]^T$ that will be referred to as the feature vector and $n(x, y)$ is as defined in (6). The f_i is considered to be non-random. Let \hat{f}_i be an unbiased estimate of f_i . Then

$$\text{variance } [f_i - \hat{f}_i] \geq E_{ii} \quad (8)$$

where E_{ii} is the i^{th} diagonal element of the matrix \underline{E} , given by equations (9) and (10).

$$\underline{E} = \underline{J}^{-1} \quad (9)$$

where \underline{J} corresponding to the Fisher information matrix is given by

$$J_{ij} = \frac{2}{N_0} \int \int_R \left[\frac{\partial s(x, y, \underline{F})}{\partial f_i} \right] \left[\frac{\partial s(x, y, \underline{F})}{\partial f_j} \right] dx dy \quad (10)$$

where R is the region of observation of $g(x, y)$

The interpretation of equations (8) - (10) is as follows: Given a scene containing an object or objects characterizable by a vector of features \underline{F} , any segmentation procedure intended to extract one or more of the intended objects will produce a shape from which the error variance of any unbiased estimate of the intended shape features is bounded by equation (8).

To show how the bound applied to the model of section (II) we note that letting

$$\underline{F} = [\Delta T, C_x, C_y, L_x, L_y]^T \quad (11)$$

$q(x, y)$ as given in equations (1) - (6), and $r \ll L_x, r \ll L_y$

$$J = \frac{2}{N_0} \begin{bmatrix} L_x L_y & 0 & 0 & \frac{1}{2} L_y \Delta T & \frac{1}{2} L_x \Delta T \\ 0 & 2 L_y \frac{\Delta T^2}{r} & 0 & 0 & 0 \\ 0 & 0 & 2 L_x \frac{\Delta T^2}{r} & 0 & 0 \\ \frac{1}{2} L_y \Delta T & 0 & 0 & \frac{1}{2} L_y \frac{\Delta T^2}{r} & \Delta T^2 \\ \frac{1}{2} L_x \Delta T & 0 & 0 & \Delta T^2 & \frac{1}{2} L_x \frac{\Delta T^2}{r} \end{bmatrix} \quad (12)$$

After inverting \underline{J} and using (8), the error bounds can be seen to be:

$$\text{var}[\hat{\Delta T} - \Delta T] \geq \frac{N_0}{2} \frac{1 - 4r^2/L_x L_y}{L_x L_y (1 - 2r^2/L_x L_y - \frac{1}{2}(\frac{1}{L_x} + \frac{1}{L_y})r)} \quad (13a)$$

$$\text{var}[\hat{C}_x - C_x] \geq \frac{N_0}{4} \frac{(r/L_y)}{\Delta T^2} \quad (13b)$$

$$\text{var}[\hat{C}_y - C_y] \geq \frac{N_0}{4} \frac{(r/L_x)}{\Delta T^2} \quad (13c)$$

$$\text{var}[\hat{L}_x - L_x] \geq \frac{N_0 r}{2\Delta T^2 L_y} \times \left[\frac{[4 - 2r/L_x]}{2 - r(1/L_x + 1/L_y) - 4\frac{r^2}{L_x L_y}} \right] \quad (13d)$$

$$\text{var}[\hat{L}_y - L_y] \geq \frac{N_0 r}{2\Delta T^2 L_x} \times \left[\frac{[4 - r/L_y]}{2 - r(1/L_x + 1/L_y) - 4\frac{r^2}{L_x L_y}} \right] \quad (13e)$$

Anomalies

The bound of equation (8) is derived from the behavior of an estimator in the neighborhood of the maximum likelihood estimate. A further consideration is the probability of anomaly, i.e., the probability that the estimate lies nowhere near the maximum likelihood estimate.

The case that will be discussed is the probability of anomaly for maximum likelihood extraction of squares. To perform the analysis a sufficient statistic for the likelihood ratio will first be derived. A bound on the probability of a given noise area having a greater likelihood than the actual square will be given, and this bound will be used to bound the overall probability of anomaly.

Following equations (1) - (5), we will set $L_x = L_y = L$ (for a square), $b = 0$ (this assumes known background) and $r < L$. To good approximation then a suitable likelihood function to use is

$$\Lambda_0(C_x, C_y, L, \Delta T) = \int_{C_y-d}^{C_y+d} \int_{C_x-d}^{C_x+d} \Delta T \left(g(s, y) - \frac{\Delta T}{2} \right) dx dy \quad (14)$$

where $d = L/2$

$$\text{Letting } G(C_x, C_y, L) = \frac{1}{L^2} \int_{C_y-d}^{C_y+d} \int_{C_x-d}^{C_x+d} g(x, y) dx dy \quad (15)$$

the value of ΔT that maximizes (14) for any choice of C_x , C_y and L is $G(C_x, C_y, L)$. Under these circumstances (14) reduces to

$$\Lambda_1(C_x, C_y, L) = \Lambda_0(C_x, C_y, L, \hat{\Delta T}) = G^2(C_x, C_y, L) \cdot L^2 \quad (16)$$

For a square centered at u, v of side 2 and offset ΔT_s imbedded in noise as defined in equation (6), the expected value of this statistic taken about the center of the square is

$$\lambda = E[G^2(u, v, 2)] \cdot 2^2 = \Delta T_s^2 2^2 + \frac{N_0}{2} \quad (17)$$

where the second term on the right of (17) is due to noise.

The probability of $G^2(C_x, C_y, L) \cdot L^2$ exceeding λ where the region $C_x - L/2 < x < C_x + L/2$, $C_y - L/2 < y < C_y + L/2$ contains only noise of spectral amplitude N_0 is

$$P(\Lambda_1(C_x, C_y, L) > \lambda) = P(|G(C_x, C_y, L)| > \sqrt{\lambda}/L) \quad (18)$$

$$= 2 \operatorname{erfc}^* \left(\frac{\sqrt{\lambda}}{L} \sqrt{\frac{2}{N_0}} L \right) \quad (18a)$$

$$= 2 \operatorname{erfc}^* \left(\sqrt{\frac{2\lambda}{N_0}} \right) \quad (18b)$$

where

$$\text{erfc}^*(x) = \int_x^\infty \frac{1}{\sqrt{2\pi}} e^{-z^2/2} dz \quad (19)$$

Note in particular that the right side of (18b) is independent of L . Therefore, the probability of any square noise region having a statistic greater than λ is independent of the size of the region. An image of area R^2 can be viewed as containing R^2/L^2 statistically independent square regions of area L^2 . Therefore, an approximation to the probability of an anomaly of size L^2 can be computed using the union bound as

$$p(\text{Anomaly of Size } L^2) \approx \frac{R^2}{L^2} \times 2 \text{erfc}^*(\sqrt{\frac{2\lambda}{N_0}}) \quad (20)$$

To estimate the total probability of anomaly these probabilities must be summed over the different sizes of squares. Before performing the summation however, the correlation of different size squares centered at the same position in the image must be taken into account. What follows relates to this correlation.

Lemma 1 - Let x_1 and x_2 be zero mean statistically independent Gaussian variables with standard deviations σ_1 and σ_2 respectively. Given $x_1 < T_1$ and $T_1 < T_2$, the probability that $x_1 + x_2 > T_2$ is bounded by

$$P(x_1 + x_2 > T_2) < \frac{\frac{\sigma_2}{\sqrt{\sigma_1^2 + \sigma_2^2}} \exp \left[-\frac{1}{2} \left[\frac{T_2^2}{\sigma_2^2} \left(1 - \frac{\sigma_1^2}{\sigma_1^2 + \sigma_2^2} \right) \right] \right] \text{erfc}^* \left[\frac{\left(\frac{\sigma_1}{\sigma_2} (T_2 - T_1) - \frac{\sigma_2}{\sigma_1} T_1 \right)}{\sqrt{\sigma_1^2 + \sigma_2^2}} \right]}{(1 - \text{erfc}^*(T_1/\sigma_1))} \quad (21)$$

Proof:

$$P(x_1 + x_2 > T_2 | x_1 < T_1) = \int_{-\infty}^{T_1} \frac{\frac{1}{\sqrt{2\pi}\sigma_1} e^{-x_1^2/2\sigma_1^2}}{(1 - \text{erfc}^*(T_1/\sigma_1))} \text{erfc}^*((T_2 - x_1)/\sigma_2) dx_1 \quad (22)$$

Now using the bound

$$\text{erfc}^*(x) < \frac{1}{2} e^{-x^2/2} \quad (23)$$

for $x > 0$, we get by substituting (23) into (22)

$$P(x_1 + x_2 > T_2 | x_1 < T_1) < \int_{-\infty}^{T_1} \frac{\frac{1}{\sqrt{2\pi}\sigma_1} e^{-x_1^2/2\sigma_1^2} \cdot \frac{1}{2} e^{-(T_2 - x_1)^2/2\sigma_2^2}}{(1 - \text{erfc}^*(T_1/\sigma_1))} dx_1 \quad (24)$$

Completing the square in the exponent of (24) obtains

$$P(x_1 + x_2 > T_2) < \frac{1}{\sqrt{2\pi}\sigma_1} \times \frac{e^{-\frac{1}{2} \left[\frac{T_2^2}{\sigma_2^2} \left(1 - \frac{\sigma_1^2}{\sigma_1^2 + \sigma_2^2} \right) \right]}}{(1 - \text{erfc}^*(T_1/\sigma_1))} \cdot \int_{-\infty}^{T_1} e^{-(x_1 - M_e)^2/\sigma_{eq}^2} dx_1 \quad (25)$$

$$\text{with } \sigma_{eq}^2 = \frac{\sigma_1^2 \sigma_2^2}{\sigma_1^2 + \sigma_2^2} \quad (25a)$$

$$\text{and } M_e = T_2 \frac{\sigma_{eq}^2}{\sigma_2^2} \quad (25b)$$

From (25) then

$$P(x_1 + x_2 > T_2) < \frac{\sqrt{2\pi} \sigma_{eq}}{\sqrt{2\pi} \sigma_1} \times \frac{1}{2} \exp \left[-\frac{1}{2} \left[\frac{T_2^2}{\sigma_2^2} \left(1 - \frac{\sigma_{eq}^2}{\sigma_2^2} \right) \right] \right] \left[\frac{\left(\operatorname{erfc}^* \left(\frac{M_e - T_1}{\sigma_e} \right) \right)}{\left(1 - \operatorname{erfc}^* (T_1/\sigma_1) \right)} \right] \quad (26)$$

Substituting (25a) and (25b) into (26) gives (21). The above lemma can be used in forming the theorem below.

Theorem 1: Given the region

$$C_x - L_2/2 < x < C_x + L_2/2$$

$$C_y - L_2/2 < y < C_y + L_2/2$$

to contain white Gaussian noise of spectral amplitude N_0 and given $L_1 < L_2$.

$$P(L_2 \cdot G(C_x, C_y, L_2) > \sqrt{\lambda} \mid L_1 \cdot G(C_x, C_y, L_1) < \sqrt{\lambda}) < \frac{1}{2} e^{-\lambda/N_0} \cdot F\left(\frac{L_2^2 - L_1^2}{L_1^2}, 2\lambda/N_0\right) \quad (27)$$

where

$$F(w, s) = \left[\sqrt{\frac{w}{1+w}} \times \frac{\left[1 - \operatorname{erfc}^* \left(s \left(\sqrt{\frac{w}{1+w}} \left(1 - \frac{1}{w} [\sqrt{1+w} - 1] \right) \right) \right) \right]}{[1 - \operatorname{erfc}^*(s)]} \right] \quad (28)$$

Proof:

$$\text{Let } x_1 = G(C_x, C_y, L_1^2) \frac{L_1^2}{L_2^2} \quad (29)$$

$$x_2 = \frac{G(C_x, C_y, L_2^2) L_2^2 - G(C_x, C_y, L_1^2) L_1^2}{L_2^2} \quad (30)$$

Then x_1 and x_2 are zero mean Gaussian random variables. Furthermore, x_1 and x_2 can be shown to be statistically independent with standard deviations

$$\begin{aligned} \sigma_1 &= \sqrt{\frac{N_0}{2}} \times \frac{L_1}{L_2} \\ \sigma_2 &= \sqrt{\frac{N_0}{2}} \frac{\sqrt{L_2^2 - L_1^2}}{L_2} \quad \text{respectively} \end{aligned} \quad (31)$$

Therefore,

$$P(L_2 \cdot G(C_x, C_y, L_2) > \sqrt{\lambda} \mid L_1 \cdot G(C_x, C_y, L_1) < \sqrt{\lambda}) = P(x_1 + x_2 > \sqrt{\lambda} \frac{1}{L_2} \mid x_1 < \sqrt{\lambda} \frac{1}{L_2}) \quad (32)$$

which from substitution into Lemma 1 and after some simplification of terms yields:

$$\sqrt{\frac{L_2^2 - L_1^2}{L_2^2}} \times \frac{1}{2} e^{-\lambda/(N_0/2)} \times \frac{\left[1 - \operatorname{erfc}^* \left(\frac{\lambda}{N_0/2} \left(\sqrt{\frac{L_2^2 - L_1^2}{L_2^2}} - \sqrt{\frac{L_1^2}{L_2^2 - L_1^2}} \left(1 - \sqrt{\frac{L_1^2}{L_2^2}} \right) \right) \right) \right]}{[1 - \operatorname{erfc}^*(\lambda/(N_0/2))]} \quad (33)$$

Making the substitution

$$w = \frac{L_2^2 - L_1^2}{L_1^2} \quad s = \lambda/(N_0/2)$$

yields

$$\frac{1}{2} e^{-s/2} \times \sqrt{\frac{w}{1+w}} \times \frac{\left[1 - \operatorname{erfc}^* \left(s \cdot \sqrt{\frac{w}{1+w}} - \frac{1}{\sqrt{w}} \left(1 - \frac{1}{\sqrt{1+w}} \right) \right) \right]}{[1 - \operatorname{erfc}^*(s)]} \quad (34)$$

or

$$4e^{-s/2} \times \left[\sqrt{\frac{w}{1+w}} \times \frac{\left[1 - \operatorname{erfc}^* \left(s \left(\sqrt{\frac{w}{1+w}} \left(1 - \frac{1}{w} [\sqrt{1+w} - 1] \right) \right) \right) \right]}{[1 - \operatorname{erfc}^*(s)]} \right] \quad (35)$$

which is the desired expression.

Note that $F(0, x) = 0$ and that $F(w, s) \rightarrow 1$ as $w \rightarrow \infty$. $F(w, s)$ is a monotonically increasing function of w representing the percentage of asymptotic probability as $L_2 \rightarrow \infty$. A plot of $F(w, s)$ for various values of s is shown in Figure 2. From this figure it can be seen that for $w = 1$ the size probabilities are relatively uncorrelated, achieving approximately .707 of their full scale value for s , (which represents total signal to noise ratio) exceeding about 2. Therefore, if $(L_2^2 - L_1^2)L_1^2 = 1$, or $L_2^2 = 2 \cdot L_1^2$, squares of size L_2^2 can be treated to have anomaly probabilities approximately independent of size L_1^2 squares on the same centers. By doubling the area of the previous sample, then, independent samples can be obtained.

Allowing the minimum size square to be r^2 and using equation (20) and the union bound:

$$P(\text{Anomaly}) \leq \frac{R^2}{r^2} \times 2 \operatorname{erfc}^* \left(\sqrt{\frac{2\lambda}{N_0}} \right) + \frac{R^2}{2r^2} \times 2 \operatorname{erfc}^* \left(\sqrt{\frac{2\lambda}{N_0}} \right) + \frac{R^2}{4r^2} \times \operatorname{erfc}^* \left(\sqrt{\frac{2\lambda}{N_0}} \right) + \dots \quad (36)$$

$$\begin{aligned} &= 2 \operatorname{erfc}^* \left(\sqrt{\frac{2\lambda}{N_0}} \right) \frac{R^2}{r^2} (1 + \frac{1}{2} + \frac{1}{4} + \dots) \\ &= 4 \frac{R^2}{r^2} \cdot \operatorname{erfc}^* \left(\sqrt{\frac{2\lambda}{N_0}} \right) \end{aligned} \quad (37)$$

Experimental results

To illustrate the bounds obtained in the previous section, two experimental image operators were applied to a series of images. Each image measured 100×100 pixels² in area and each contained a 5×5 pixel² square at its center. The images were corrupted by uncorrelated noise of a varying amplitude. Fifteen independent images were obtained at each noise level tested. The function of each operator was to estimate the position, size and intensity offset of the square in each image. A sample result of such an operator is shown in Figure 3. The errors in estimated parameters and probability of anomaly were calculated at the varying noise levels and compared to the computed bounds obtained in the previous section.

The first operator, denoted OP1, is basically an exhaustive search for the maximum likelihood square over the image. Each possible size square is tested in every possible position, and a likelihood measure similar to equation (16) is computed for each combination. The combination having the greatest value of this measure is then used to estimate the relevant parameters. The second operator, denoted OP2, operates in a similar manner, but uses an iterative 3×3 smoothing filter to estimate the average intensity of square whose effective area is a linear function of the number of smoothing iterations. The intention was to determine the performance degradation caused by replacing a global averaging process by a series of local averaging processes. The results obtained from these operators are graphed in Figure 4 which shows in general a good agreement with the bounds obtained in the previous sections.

Summary and conclusions

In general, the determination of noise sensitivity of a segmentation operator over a wide variety of imagery types is a difficult procedure. By simplifying the image model, however, bounds can be obtained for the error variances of certain shape parameters of which it is often the object of the segmentation procedure to estimate. Real image operators can be compared with these bounds to provide objective measures of performance, determine SNR degradation, and suggest potential areas for improvement. As important as the bounds on parameter estimation are the bounds on anomalous behavior, which can be used to bound the tradeoff between detection probability and false alarm rate for systems applying segmentation to functions such as automatic target acquisition. A simple image model was employed in this paper, and the derived bounds were compared with actual performance obtained from two operators. The observed data agreed well with the computed bounds. In the future, we plan on comparing the bounds with performance obtained from more realistic segmentation operators, as well as extending the range of applicability of the image model employed.

Acknowledgement

The authors are grateful for the accurate typing and patience of Sherry Gardner. This work is supported by internal research in automatic target recognition at Hughes Aircraft.

References

1. L. M. Rubin, D. Y. Tseng, "Automatic Target Cueing", Proceedings of the Fourth International Joint Conference on Pattern Recognition, November 1978.
2. "FLIR Image Analysis with the Autoscreener Computer Simulation" Vols. 1 & 2, Contract DAAG53-75-C-0246 to Night Vision Laboratory.
3. D. Milgram, "Region Extraction Using Convergent Evident", Proc.: Image Understanding Workshop, April 1977, Science Applications, Inc.
4. D. Panda, "Segmentation of FLIR Images Pixel Classification", Proc.: Image Understanding Workshop, April 1977, Science Applications, Inc.
5. M. Geokezas, R. Jennewine, and G. P. Swanlund, "A Real Time Imagery Screener", Report on work conducted on USAF Contract AFAL-TR-74-184, October 1974.
6. "Processing of FLIR Data on DICIFER", Contract DAAG53-75-C-0277 for Night Vision Laboratory, by Pattern Analysis and Recognition Corp.
7. H. L. Van Trees, Detection, Estimation, and Modulation Theory, Part I, Chapter 4, 1968, John Wiley & Sons.

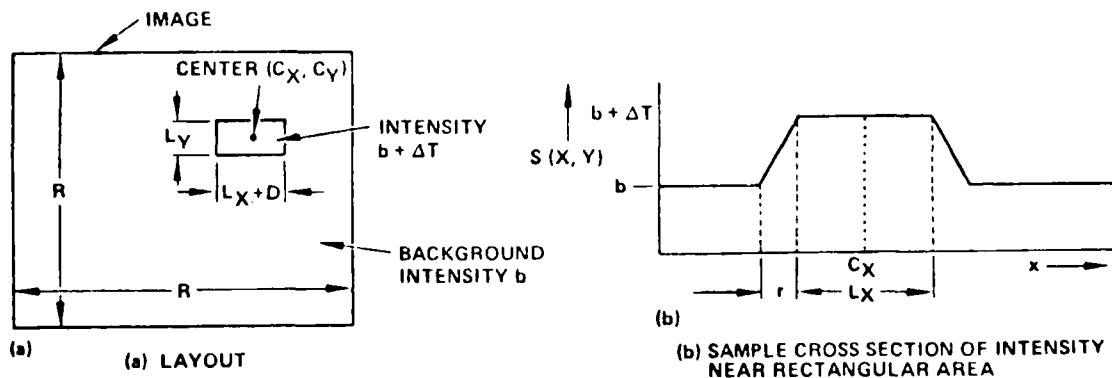


Figure 1. Image Model

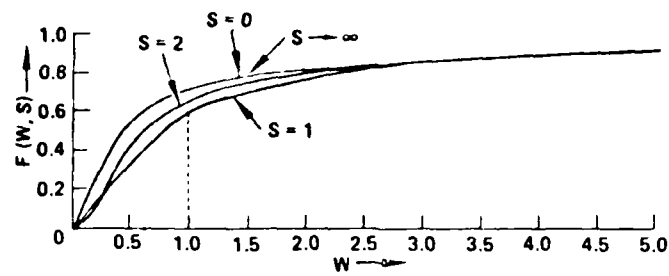


Figure 2. Plots of $F(W, S)$ for $S = 0, 1, 2$, and limit as $S \rightarrow \infty$
 Note that limiting curve and $S = 0$ curve coincide for $W > 0$.

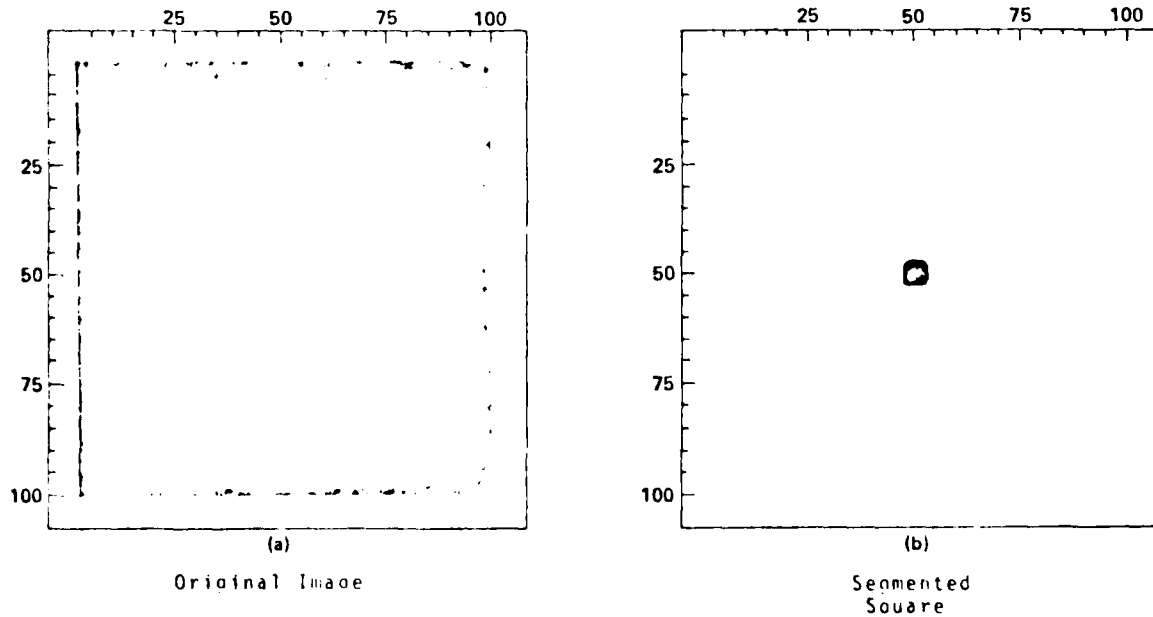


Figure 3. Sample Result of Operator (OP1) on an image with $SNR = 1.5$

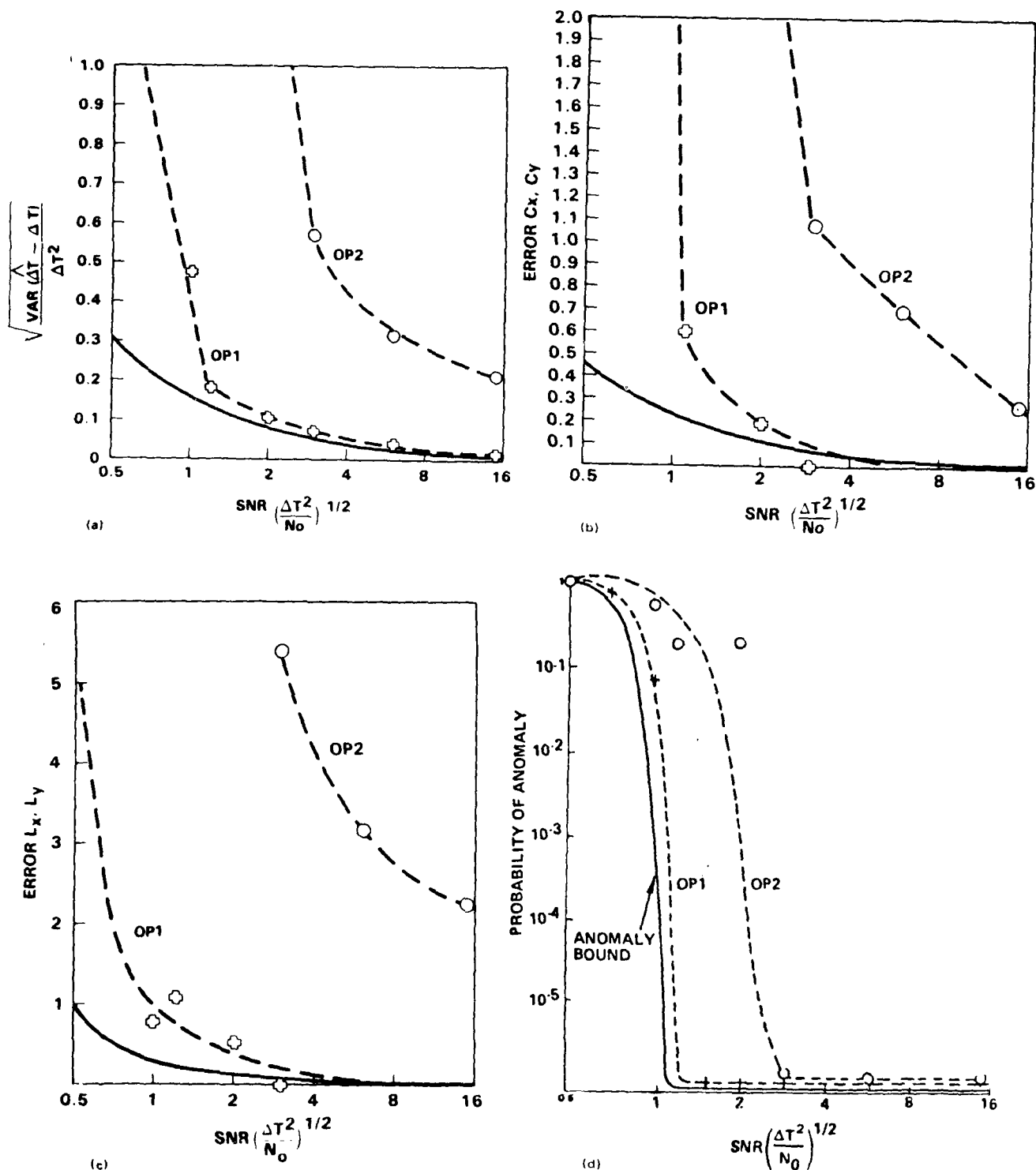


Figure 4. Comparison of performance measurements obtained from the two experimental image operators with the computed performance bounds. Fifteen images were used per operator per SNR level tested.

APPENDIX B. SOBEL OPERATOR PROBABILITY DENSITY

This appendix will derive the probability density of the Sobel edge operator defined in Eqns. (7-3) - (7-5). To compute this result it should be noted that the horizontal and vertical contributions to the Sobel operator $S_H(x, y)$ and $S_V(x, y)$ in (7-1) are uncorrelated random variables.

The probability density function $P(S)$ for the sum of the absolute values of two Gaussian independent variables with non-zero means is given by

$$P(S) = \int_{-\infty}^{\infty} dx \int_{-\infty}^{\infty} dy \delta(S - |x| - |y|) \rho_{x_0}(x) \rho_{y_0}(y), \quad (B-1)$$

where

$$\rho_{x_0}(x) = \frac{1}{\sqrt{2\pi}\sigma} e^{-(x-x_0)^2/2\sigma^2} \quad (B-2)$$

$$\rho_{y_0}(y) = \frac{1}{\sqrt{2\pi}\sigma} e^{-(y-y_0)^2/2\sigma^2} \quad (B-3)$$

It is readily verified that $P(S)$ is properly normalized

$$\int_0^{\infty} P(s) ds = 1 \quad (B-4)$$

by interchanging the order integration.

Breaking the integration in (B-1) into its contribution from the four quadrants of the x-y plane,

$$\begin{aligned}
 P(S) = & \int_0^{\infty} dx \int_0^{\infty} dy \delta(s - x - y) \rho_{x_0}(x) \rho_{y_0}(y) \\
 & + \int_{-\infty}^0 dx \int_0^{\infty} dy \delta(s + x - y) \rho_{x_0}(x) \rho_{y_0}(y) \\
 & + \int_0^{\infty} dx \int_{-\infty}^0 dy \delta(s - x + y) \rho_{x_0}(x) \rho_{y_0}(y) \\
 & + \int_{-\infty}^0 dx \int_{-\infty}^0 dy \delta(s + x + y) \rho_{x_0}(x) \rho_{y_0}(y)
 \end{aligned} \tag{B-5}$$

Changing integration variables from x to -x and y to -y as appropriate, and using the fact that

$$\rho_{x_0}(-x) = \rho_{-x_0}(x) \tag{B-6}$$

$$\rho_{y_0}(-y) = \rho_{-y_0}(y) \tag{B-7}$$

Eq. (B-5) becomes

$$\begin{aligned}
 P(S) = & \int_0^{\infty} dx \int_0^{\infty} dy \delta(s - x - y) \left[\rho_{x_0}(x) + \rho_{-x_0}(x) \right] \left[\rho_{y_0}(y) + \rho_{-y_0}(y) \right] \\
 = & \rho_{x_0 y_0}(S) + \rho_{-x_0, y_0}(S) + \rho_{x_0, -y_0}(S) + \rho_{-x_0, -y_0}(S)
 \end{aligned} \tag{B-8}$$

where

$$\rho_{x_o y_o}(S) \stackrel{d}{=} \int_0^{\infty} dx \int_0^{\infty} dy \delta(s - x - y) \rho_{x_o}(x) \rho_{y_o}(y) \quad (B-9)$$

Substituting (B-2) and (B-3) into (B-9), results in

$$\rho_{x_o y_o}(S) = \frac{1}{2\pi\sigma^2} \int_0^{\infty} dx \int_0^{\infty} dy \delta(s - x - y) e^{-\left[(x-x_o)^2 + (y-y_o)^2\right] / 2\sigma^2} \quad (B-11)$$

Changing to integration variables U and V defined by

$$U = x + y \quad (B-12a)$$

$$V = x - y \quad (B-12b)$$

or

$$X = \frac{U + V}{2} \quad (B-13a)$$

$$Y = \frac{U - V}{2} \quad (B-13b)$$

The Jacobian of the transformation is equal to 1/2, and since

$$\begin{aligned} (x - x_o)^2 + (y - y_o)^2 &= \left[\frac{1}{2} (U + V) - x_o \right]^2 + \left[\frac{1}{2} (U - V) - y_o \right]^2 \\ &= \left\{ \frac{1}{2} (U^2 + V^2) + x_o^2 + y_o^2 - U(x_o + y_o) + V(y_o - x_o) \right\} \end{aligned} \quad (B-14)$$

$$\rho_{x_o y_o}(S) = \frac{1}{4\pi\sigma^2} \int_0^u du (s - U) \int_{-u}^u dV \exp \left\{ -(B14)/2^2 \right\} \quad (B-15)$$

where B14 is the last expression in Equation B-14.

Using the NBS Handbook integral 7.4.32 yields the result

$$\begin{aligned} \int_{-U}^U dv e^{-\left[\frac{1}{2}v^2 + V(y_o - x_o)\right]/2\sigma^2} dv = \\ = \sqrt{\pi\sigma^2} e^{(y_o - x_o)^2 / 4\sigma^2} \left[\operatorname{erf} \frac{U}{2\sigma} + \frac{y - x_o}{2\sigma} + \operatorname{erf} \frac{U}{2\sigma} - \frac{y_o - x_o}{2\sigma} \right] \end{aligned} \quad (B-16)$$

Substituting (B-16) into (B-15),

$$\rho_{x_o y_o}(S) = \frac{1}{4\sqrt{\pi\sigma^2}} \left(- \left[x_o^2 + y_o^2 + S^2 \right] / 4\sigma^2 \right) \cdot F(S, x_o, y_o) \quad (B-17)$$

where $F(S, x_o, y_o)$ is defined by

$$F(S, x_o, y_o) = e^{\left[S(x_o + y_o) - x_o y_o \right] / 2\sigma^2} \left[\operatorname{erf} \left(\frac{S + y_o - x_o}{2\sigma} \right) + \operatorname{erf} \left(\frac{S - y_o + x_o}{2\sigma} \right) \right] \quad (B-18)$$

From (B-8) it then follows that the density distribution function $P(S)$ is given by

$$P(S) = \frac{1}{4\sqrt{\pi\sigma}} e^{-\left[x_o^2 + y_o^2 + S^2\right]/4\sigma^2} \left\{ F(S, x_o, y_o) + F(S, -x_o, -y_o) + F(S, x_o, -y_o) + F(S, -x_o, y_o) \right\} \quad (B-19)$$

which is the general result.

Specializing to the case of a horizontal edge pixel

$$x_o = \mathcal{E}\left[S_V(x, y)\right] = 0 \quad (B-20a)$$

$$y_o = \mathcal{E}\left[S_H(x, y)\right] = 4\Delta T \quad (B-20b)$$

Eq. (B-19) reduces to

$$P(S) = \frac{1}{2\sqrt{\pi\sigma}} e^{-\left[(4\Delta T)^2 + S^2\right]/4\sigma^2} \left[F(S, 0, 4\Delta T) + F(S, 0, -4\Delta T) \right] \quad (B-21)$$

and (B-18) reduces to

$$F(S, 0, 4\Delta T) = e^{4S\Delta T/2\sigma^2} \left[\operatorname{erf}\left(\frac{S + 4\Delta T}{2\sigma}\right) + \operatorname{erf}\left(\frac{S - 4\Delta T}{2\sigma}\right) \right] \quad (B-22)$$

Thus the probability density of a Sobel edge operation in the vicinity of an intensity discontinuity of magnitude ΔT is

$$P(S) = \frac{1}{2\sqrt{\pi}\sigma} \left[e^{-(S-4\Delta T)^2/4\sigma^2} + e^{-(S+4\Delta T)^2/4\sigma^2} \right] \cdot \left[\operatorname{erf} \left(\frac{S+4\Delta T}{2\sigma} \right) + \operatorname{erf} \left(\frac{S-4\Delta T}{2\sigma} \right) \right] \quad (\text{B-23})$$

which, aside from a change of variable, is the same as Eq. (7-19) in the main text.

From the definition of the error function, Eq. (B-23) can also be written

$$P(S) = \frac{1}{4} \frac{\partial}{\partial S} \left[\operatorname{erf} \left(\frac{S+4\Delta T}{2\sigma} \right) + \operatorname{erf} \left(\frac{S-4\Delta T}{2\sigma} \right) \right]^2 \quad (\text{B-24})$$

APPENDIX C. AVERAGE VALUE AND VARIANCE OF SOBEL EDGE OPERATOR

This appendix will calculate the mean and variance of a Sobel edge operator in the vicinity of an intensity discontinuity in an image. The definition of the Sobel operator may be rewritten

$$S = |S_H| + |S_V| \quad (C-1)$$

where S_H and S_V are the horizontal and vertical components respectively. The variance of S , σ_2^2 is defined by (cf Eqn. 7-3 - 7-5)

$$\sigma_2^2 \equiv \mathcal{E}(S^2) - (\mathcal{E}(S))^2. \quad (C-2)$$

Assume we are dealing with a vertical edge with sufficiently high SNR that

$$\mathcal{E}|S_V| \approx |\mathcal{E}(S_V)| = 4\Delta T \quad (C-3)$$

Now $\mathcal{E}|S_H|$ can be written as

$$\begin{aligned} \mathcal{E}|S_H| &= \frac{1}{\sqrt{2\pi}\sigma} \int_{-\infty}^{\infty} |x| e^{-x^2/2\sigma^2} dx \\ &= \frac{2}{\sqrt{2\pi}\sigma} \int_0^{\infty} x e^{-x^2/2\sigma^2} dx \\ &= \sqrt{\frac{2}{\pi}} \sigma \end{aligned} \quad (C-4)$$

Thus, from (C-1), (C-3), and (C-4) $\mathcal{E}(S)$ becomes

$$\mathcal{E}(S) = 4\Delta T + \sqrt{\frac{2}{\pi}} \underline{\sigma}, \quad (C-5)$$

which derives Eq. (7-16) of the main text.

Also,

$$\mathcal{E}(S^2) = \mathcal{E}|S_H|^2 + 2 \mathcal{E}(|S_H| \cdot |S_V|) + \mathcal{E}|S_V|^2 \quad (C-6)$$

Now

$$\mathcal{E}|S_H|^2 = \mathcal{E}(S_H^2) = \underline{\sigma}^2, \quad (C-7)$$

and

$$\mathcal{E}|S_V|^2 = \mathcal{E}(S_V^2) = (4\Delta T)^2 + \underline{\sigma}^2, \quad (C-8)$$

$$\mathcal{E}(|S_H| \cdot |S_V|) \approx \mathcal{E}(S_V \cdot |S_H|) = 4\Delta T \cdot \mathcal{E}|S_H| = 4\Delta T \sqrt{\frac{2}{\pi}} \underline{\sigma} \quad (C-9)$$

Hence

$$\mathcal{E}(S^2) = (4\Delta T)^2 + 2\underline{\sigma}^2 + 8\Delta T \sqrt{\frac{2}{\pi}} \underline{\sigma}. \quad (C-10)$$

Substituting (C-10) and (C-5) into (C-2) gives

$$\sigma_z^2 = 2 \left(1 - \frac{1}{\pi}\right) \underline{\sigma}^2, \quad (C-11)$$

which derives Eq. (7-21) of the main text. Note that although (C-5) and (C-11) were derived for the case of a vertical edge, a horizontal edge would give the same results.

APPENDIX D. PROBABILITY OF NON-DETECTION FOR A PARALLEL-TO-THE BOUNDARY PAIR

In this appendix we calculate the probability P_{2P} that, due to noise, a pair of neighboring edge pixels parallel to the boundary both fail to indicate edges as they should. If there were no correlation between neighbors, P_{2P} would simply equal P_N^2 , the square of the probability of non-detection of a single edge pixel. However, as we shall see, there is a positive correlation between neighbors so that

$$P_{2P} < P_N^2 \quad (D-1)$$

We specialize to neighboring pixels along the right boundary and calculate the (x, y) and $(x, y+1)$ correlations of the Sobel operator components. Rewriting Eqs. (7-4) and (7-5) in the main text for the $(x, y+1)$ pixel, we obtain the Sobel components:

$$\begin{aligned} S_{11}(x, y+1) = & I(x-1, y) + 2I(x, y) + I(x+1, y) - I(x-1, y+2) - 2I(x, y+2) \\ & - I(x+1, y+2) \end{aligned} \quad (D-2)$$

and

$$\begin{aligned} S_V(x, y+1) = & I(x-1, y) + 2I(x-1, y+1) + I(x-1, y+2) - I(x+1, y) \\ & - 2I(x+1, y+1) - I(x+1, y+2). \end{aligned} \quad (D-3)$$

Taking expectations of products of adjacent operator outputs, we find

$$\mathcal{E} \left(S_V(x, y) S_V(x, y+1) \right) = (4\Delta T)^2 + 8\sigma^2 \quad (D-4)$$

$$\mathcal{E} \left(S_H(x, y) S_H(x, y+1) \right) = 0 \quad (D-5)$$

$$\mathcal{E} \left(S_H(x, y) S_V(x, y+1) \right) = 0 \quad (D-6)$$

$$\mathcal{E} \left(S_V(x, y) S_H(x, y+1) \right) = 0 \quad (D-7)$$

Introducing a more condensed notation

$$S \equiv S(x, y) \quad , \quad W \equiv S(x, y+1) \quad (D-8)$$

$$U \equiv S_H(x, y) \quad , \quad U_+ \equiv S_U(x, y+1) \quad (D-9)$$

$$V \equiv S_V(x, y) \quad , \quad V_+ \equiv S_V(x, y+1) \quad (D-10)$$

we have

$$S = |U| + |V| \quad , \quad W = |U_+| + |V_+| \quad (D-11)$$

The pair probability we wish to calculate P_{2P} is given by

$$P_{2P} = \int_0^T dS \int_0^T dW P(S, W) \quad (D-12)$$

where $P(S, W)$ is the proper bivariate density distribution function

$$\begin{aligned}
 P(S, W) = & \int_{-\infty}^{\infty} dU \int_{-\infty}^{\infty} dU_+ \int_{-\infty}^{\infty} dV \int_{-\infty}^{\infty} dV_+ \\
 & \delta(S - |U| - |V|) \delta(W - |U_+| - |V_+|) \\
 & \cdot P(U, U_+, V, V_+)
 \end{aligned} \tag{D-13}$$

Since U, U_+, V and V_+ are linear combinations of random Gaussian variables. $P(U, U_+, V, V_+)$ is a quadra-variate Gaussian density function. In view of (D-4) - (D-7),

$$\begin{aligned}
 P(U, U_+, V, V_+) = & \frac{1}{2\pi\sigma^2} e^{-\frac{(U^2 + U_+^2)}{2\sigma^2}} \cdot \frac{1}{2\pi\sigma^2 \sqrt{1 - \rho^2}} \\
 & \cdot \exp \left[-\frac{(V - 4\Delta T)^2 - 2\rho(V - 4\Delta T)(V_+ - 4\Delta T) + (V_+ - 4\Delta T)^2}{2\sigma^2(1 - \rho^2)} \right]
 \end{aligned} \tag{D-14}$$

where

$$\sigma^2 = 12\sigma^2 \tag{D-15}$$

and the correlation coefficient

$$\rho = \frac{2}{3}. \tag{D-16}$$

Substituting (D-14) into (D-13), and (D-13) in (D-12) leads to a six-fold integration. Although it is possible to perform most of the integrations, we have not succeeded in performing them all without making unsatisfactory approximations.

Consequently, we will approximate D-13 with a bivariate Gaussian distribution:

$$P(S, W) = \frac{1}{2\pi\sigma_S^2\sqrt{1-\rho_S^2}} \exp \left[-\frac{(S-\bar{S})^2 - 2\rho_S(S-\bar{S})(W-\bar{S}) + (W-\bar{S})^2}{2\sigma_S^2(1-\rho_S^2)} \right] \quad (D-17)$$

Note, that this reduces to the ordinary Gaussian function used previously.

The average intensity \bar{S} and variance σ_S^2 have been calculated previously in Eqs. (C-5) and (C-11), respectively. The correlation coefficient ρ_S is calculated from

$$\rho_S \sigma_S^2 = \mathcal{E}(SW) - \bar{S}^2 \quad (D-18)$$

$$\mathcal{E}(SW) = \mathcal{E} \left[(|U| \cdot |U_+|) + \mathcal{E}(|U| \cdot |V_+|) + \mathcal{E}(|V| \cdot |U_+|) + \mathcal{E}(|V| \cdot |V_+|) \right] \quad (D-19)$$

Since we are assuming a sufficiently high SNR as in Appendix C, we have

$$\mathcal{E}(|U| \cdot |V_+|) \approx 4\Delta T \mathcal{E}(|U|) = 4\Delta T \sqrt{\frac{2}{\pi}} \sigma \quad (D-20)$$

$$\mathcal{E}(|V| \cdot |U_+|) \approx 4\Delta T \mathcal{E}(|U_+|) = 4\Delta T \sqrt{\frac{2}{\pi}} \sigma \quad (D-21)$$

$$\mathcal{E}(|V| \cdot |V_+|) \approx \mathcal{E}(V V_+) = (4\Delta T)^2 + \rho \sigma^2 \quad (D-22)$$

Since U and U_+ are independent variables

$$\epsilon(|U| \cdot |U_+|) = \epsilon(|U|) \cdot \epsilon(|U_+|) = \frac{2}{\pi} \sigma^2 \quad (D-23)$$

Solving Eqs. (D-14) - (D-19) for ρ_S with the aid of (C-5) and (C-11), one obtains

$$\rho_S = \rho \frac{\sigma^2}{\sigma_2^2} = \frac{\rho}{2 \left(1 - \frac{1}{\pi}\right)} = 0.73\rho \quad (D-24)$$

Since by (D-16),

$$\rho = 2/3, \quad (D-25)$$

$$\rho_S = 0.49$$

The formal approximate solution to the problem is now given by (D-12) with the lower limits extended to $-\infty$, consistent with our assumption that use of the bivariate Gaussian distribution (D-17) is justified,

$$P_{LP} = \int_{-\infty}^T dS \int_{-\infty}^T dW P(S, W) \quad (D-26)$$

Introducing new integration variables x and y defined by

$$x = \frac{\bar{S} - S}{\sigma_2} \quad (D-27)$$

$$y = \frac{\bar{S} - W}{\sigma_2} \quad (D-28)$$

one obtains

$$P_{2P} = L \left(\frac{\bar{S} - T}{\sigma_2}, \frac{\bar{S} - T}{\sigma_2}, \rho_S \right) \quad (D-29)$$

where L is the probability function defined by

$$L(h, k, \rho) = \int_h^\infty dx \int_K^\infty dy g(x, y, \rho) \quad (D-30)$$

where $g(x, y, \rho)$ is the bivariate normal probability function defined by

$$g(x, y, \rho) = \frac{1}{2\pi\sqrt{1-\rho^2}} \exp \left[-\frac{1}{2} \left(\frac{x^2 - 2\rho xy + y^2}{1-\rho^2} \right) \right]. \quad (D-31)$$

The functions $L(h, k, \rho)$ and $g(x, y, \rho)$ are defined in Section 26.3 of Abramowitz and Stegun NBS Handbook of Mathematical functions. Using another formula given there, Eq. (D-29) can be put in the form

$$P_{2P} = 2 \left[L \left(\frac{\bar{S} - T}{\sigma_2}, 0, -\sqrt{\frac{1-\rho_S}{2}} \right) \right] \quad (D-32)$$

P_{2P} is then obtained by graphical interpolation from iso-valued curves given in this reference for $L(h, 0, \rho)$ as function of h and ρ .

AD-A097 723

HUGHES AIRCRAFT CO CULVER CITY CA IMAGE PROCESSING LAB

F/G 12/1

ATAC AUTOCUER MODELING ANALYSIS.(U)

JAN 81 R L FREY, C D NEALY, L M RUBIN

DAAK70-77-C-0232

UNCLASSIFIED

HAC-FR-80-70-1325

NL

2 OF 2

AU A
OR 723A



END
DATE
FILMED
5-81
DTIC

APPENDIX E. PROBABILITY OF PAIR GAP PERPENDICULAR TO BOUNDARY

In this appendix, we calculate the probability P_{2S} that, due to noise, a pair of neighboring edge pixels perpendicular to the boundary both fail to indicate edges as they should.

The analysis proceeds as in Appendix D except that we are now dealing with correlation along the right boundary between pixels (x, y) and $(x+1, y)$. Rewriting the Sobel equations for the $(x+1, y)$ pixel, one obtains

$$\begin{aligned} S_H(x+1, y) = & I(x, y-1) + 2I(x+1, y-1) + I(x+2, y-1) - I(x, y+1) \\ & - 2I(x+1, y+1) + I(x+2, y+1) \end{aligned} \quad (E-1)$$

$$\begin{aligned} S_V(x+1, y) = & I(x, y-1) + 2I(x, y) + I(x, y+1) - I(x+2, y-1) \\ & - 2I(x+2, y) - I(x+2, y+1) \end{aligned} \quad (E-2)$$

Taking expectations of adjacent operator outputs, we find

$$\mathcal{E} \left(S_V(x, y) S_V(x+1, y) \right) = (4\Delta T)^2 \quad (E-3)$$

$$\mathcal{E} \left(S_V(x, y) S_H(x+1, y) \right) = 0 \quad (E-4)$$

$$\mathcal{E} \left(S_H(x, y) S_V(x+1, y) \right) = 0 \quad (E-5a)$$

$$\mathcal{E} \left(S_H(x, y) S_H(x+1, y) \right) = 8\sigma^2 = \rho \bar{\sigma}^2 \quad (E-5b)$$

where as in Appendix D.

$$\rho = \frac{2}{3} . \quad (\text{E-6})$$

We again assume the bivariate Gaussian distribution (D-17) with S and W given by Eqs. (D-11) with the new definitions

$$S \equiv S(x, y) , \quad W \equiv S(x+1, y) \quad (\text{E-7})$$

$$U \equiv S_H(x, y) , \quad U_+ \equiv S_H(x+1, y) \quad (\text{E-8})$$

$$V \equiv S_V(x, y) , \quad V_+ \equiv S_V(x+1, y) \quad (\text{E-9})$$

Corresponding to (D-18), the correlation coefficient ρ_s is calculated from

$$\rho_s \sigma_2^2 = \mathcal{E}(SW) - \bar{S}^2 . \quad (\text{E-10})$$

Eq. (D-19) is still valid, but the terms have to be recalculated since the definitions U_+ and V_+ are different than they were. Again assuming a sufficiently high SNR, we have

$$\mathcal{E}(|V| \cdot |V_+|) \simeq \mathcal{E}(V V_+) = (4\Delta T)^2 \quad (\text{E-11})$$

by Eq. (E-3)

$$\mathcal{E}(|V| \cdot |U_+|) \simeq 4\Delta T \mathcal{E}(|U_+|) = 4\Delta T \sqrt{\frac{2}{\pi}} \sigma \quad (\text{E-12})$$

$$\mathcal{E}(|U| \cdot |V_+|) \simeq 4\Delta T \mathcal{E}(|U|) = 4\Delta T \sqrt{\frac{2}{\pi}} \sigma \quad (\text{E-13})$$

The calculation of $\mathcal{E}(|U| \cdot |U_+|)$ is more difficult since U and U_+ are correlated, and both have zero mean so that the high SNR approximation is no help here.

We have

$$\mathcal{E}(|U| \cdot |U_+|) = \int_{-\infty}^{\infty} dU \int_{-\infty}^{\infty} dU_+ \cdot |U| \cdot |U_+| \cdot P(U, U_+, \rho) \quad (\text{E-14})$$

where $P(U, U_+, \rho)$ is the bivariate Gaussian distribution defined by

$$P(x, y, \rho) = \frac{1}{2\pi\sigma^2\sqrt{1-\rho^2}} \exp \left[-\frac{x^2 - 2\rho xy + y^2}{2(1-\rho^2)\sigma^2} \right] \quad (\text{E-15})$$

Integrating over each quadrant separately, changing some integration variables to their negatives, and combining terms, one finds

$$\begin{aligned} \mathcal{E}(|U| \cdot |U_+|) &= 2 \int_0^{\infty} dx \int_0^{\infty} dy xy P(x, y, \rho) \\ &\quad + 2 \int_0^{\infty} dx \int_0^{\infty} dy xy P(x, y, -\rho). \end{aligned} \quad (\text{E-16})$$

We integrate the first term first by converting to polar coordinates,

$$x = r \cos \theta, \quad y = r \sin \theta. \quad (\text{E-17})$$

$$2 \int_0^{\infty} dx \int_0^{\infty} dy xy P(x, y, \rho) = \frac{2}{2\pi\sigma^2\sqrt{1-\rho^2}} \int_0^{\frac{\pi}{2}} \sin 2\theta d\theta \cdot F(\theta) \quad (\text{E-18})$$

where

$$F(\theta) = \int_0^{\infty} r^3 dr \exp \left[-\frac{r^2(1-\rho \sin 2\theta)}{2(1-\rho^2)\sigma^2} \right] \quad (\text{E-19})$$

$$= 2 \left(\frac{(1-\rho^2)\sigma^2}{1-\rho \sin 2\theta} \right)^2$$

Therefore

$$\begin{aligned} \int_0^{\frac{\pi}{2}} \sin 2\theta d\theta \cdot F(\theta) &= 2(1 - \rho^2)^2 \sigma^4 \int_0^{\frac{\pi}{2}} \frac{\sin 2\theta d\theta}{(1 - \rho \sin 2\theta)^2} \\ &= 2(1 - \rho^2)^2 \sigma^4 \frac{\partial}{\partial \rho} \int_0^{\frac{\pi}{2}} \frac{d\theta}{1 - \rho \sin 2\theta} \end{aligned} \quad (E-20)$$

From integral tables, one finds

$$\int_0^{\frac{\pi}{2}} \frac{d\theta}{1 - \rho \sin 2\theta} = \frac{1}{\sqrt{1 - \rho^2}} \left[\frac{\pi}{2} + \tan^{-1} \frac{\rho}{\sqrt{1 - \rho^2}} \right]. \quad (E-21)$$

The derivative of (E-21) with respect to ρ is

$$\rho(1 - \rho^2)^{-3/2} \left[\frac{\pi}{2} + \tan^{-1} \frac{\rho}{\sqrt{1 - \rho^2}} \right] + \frac{1}{1 - \rho^2} \quad (E-22)$$

Substituting (E-22) into (E-20), and (E-20) into (E-18) one finds

$$2 \int_0^{\infty} x dx \int_0^{\infty} y dy P(x, y, \rho) = \frac{\sigma^2}{\pi} \left[\rho \left(\frac{\pi}{2} + \tan^{-1} \left(\frac{\rho}{\sqrt{1 - \rho^2}} \right) \right) + \sqrt{1 - \rho^2} \right] \quad (E-23)$$

Substituting (E-23) and a similar quantity with ρ replaced by $-\rho$ one obtains

$$\epsilon(|U| \cdot |U_+|) = \frac{2\sigma^2}{\pi} \left[\rho \tan^{-1} \left(\frac{\rho}{\sqrt{1 - \rho^2}} \right) + \sqrt{1 - \rho^2} \right] \quad (E-24)$$

Combining Eqs. (E-10), (D-19), (E-11), (E-12), (E-13), (E-24), (C-5), and (C-11), and solving for ρ_s , one obtains

$$\rho_s = \frac{\rho \tan^{-1}(\rho/(1-\rho^2)^{1/2}) + (1-\rho^2)^{1/2} - 1}{\pi - 1} \quad (\text{E-25})$$

Numerical calculation verifies that ρ_s is a monotonically increasing function of ρ as, of course, it must be. For the case of interest, $\rho = 2/3$,

$$\rho_s \approx 0.11. \quad (\text{E-26})$$

Note that for edge operators other than the Sobel, Eq. (E-25) for ρ_s and Eq. (D-24) for ρ_s will still be valid with different values of ρ .

The formal solution for P_{2S} , the probability of a pair gap perpendicular to the boundary, is the same as that given in Appendix D for P_{2P} . However, for the value of ρ_s given in (E-26), the correlation is sufficiently small that neglecting the correlation altogether introduce little error. Hence

$$P_{2S} \approx P_N^2, \quad (\text{E-27})$$

where

$$P_N = 1 - P_D \quad (\text{E-28})$$

is the probability of not detecting any specified edge pixel (excluding corners, of course).

APPENDIX F. NEXT-NEAREST-NEIGHBOR CORRELATION

In order to gain some idea of how good our neglect of next-nearest-neighbor correlation is in our theory of gaps higher than second-order, we calculate the correlation coefficient of the Sobel operator along the right boundary between pixels (x, y) and $(x, y+2)$.

Rewriting the Sobel equations for the $(x, y+2)$ pixel, one obtains

$$\begin{aligned} S_H(x, y+2) = & I(x-1, y+1) + 2I(x, y+1) + I(x+1, y+1) - I(x-1, y+3) \\ & - 2I(x, y+3) + I(x+1, y+3) \end{aligned} \quad (F-1)$$

$$\begin{aligned} S_V(x, y+2) = & I(x-1, y+1) + 2I(x-1, y+2) + I(x-1, y+3) - I(x+1, y+1) \\ & - 2I(x+1, y+2) - I(x+1, y+3) \end{aligned} \quad (F-2)$$

Taking expectations of operator outputs separated by two pixels, we find

$$\begin{aligned} \mathcal{E}(S_V(x, y) S_V(x, y+2)) &= (4\Delta T)^2 + 2\sigma^2 \\ &\equiv (4\Delta T)^2 + \rho_V \sigma^2 \end{aligned} \quad (F-3)$$

$$\mathcal{E}(S_V(x, y) S_H(x, y+2)) = 0 \quad (F-4)$$

$$\mathcal{E}(S_H(x, y) S_V(x, y+2)) = 0 \quad (F-5)$$

$$\mathcal{E}(S_H(x, y) S_H(x, y+2)) = -6\sigma^2 \equiv \rho_H \sigma^2, \quad (F-6)$$

where

$$\rho_V = 1/6 \quad (F-7)$$

and

$$\rho_H = -1/2. \quad (F-8)$$

We again assume the bivariate Gaussian distribution (D17) with S and W given by Eqs. (D-11) with ρ_S replaced by P_{NNN} , the next-nearest-neighbor correlation coefficient which we wish to calculate, and (D-8), (D-9), and (D-10) replaced by

$$S \equiv S(x, y), \quad W \equiv S(x, y+2) \quad (F-9)$$

$$U \equiv S_H(x, y), \quad U_+ \equiv S_H(x, y+2) \quad (F-10)$$

$$V \equiv S_V(x, y), \quad V_+ \equiv S_V(x, y+2) \quad (F-11)$$

Corresponding to (D-18), the correlation coefficient P_{NNN} is calculated from

$$P_{NNN} \sigma_2^2 = \mathcal{E}(SW) - \bar{S}^{-2} \quad (F-12)$$

Eq. (D-19) is still valid, but the terms have to be recalculated, since the definitions of U_+ and V_+ have changed. Again assuming a sufficiently high SNR, we have

$$\mathcal{E}(|V| \cdot |V_+|) \approx \mathcal{E}(VV_+) = (4\Delta T)^2 + \rho_V \sigma^2 \quad (F-13)$$

by Eq. (F-3).

$$\mathcal{E}(|V| \cdot |U_+|) \approx 4\Delta T \mathcal{E}(|U_+|) = 4\Delta T \sqrt{\frac{2}{\pi}} \sigma \quad (\text{F-14})$$

$$\mathcal{E}(|U| \cdot |V_+|) \approx 4\Delta T \mathcal{E}(|U|) = 4\Delta T \sqrt{\frac{2}{\pi}} \sigma \quad (\text{F-15})$$

The calculation of $\mathcal{E}(|U| \cdot |U_+|)$ is given by Eq. (E-24) with ρ replaced by ρ_H . Combining all the necessary equations as previously, one obtains

$$P_{\text{NNN}} = \frac{\rho_H \tan^{-1} \frac{\rho_H}{\sqrt{1 - \rho_H^2}} + \sqrt{1 - \rho_H^2} - 1 + \frac{\pi}{2} \rho_V}{\pi - 1} \quad (\text{F-16})$$

Applying the values for ρ_V and ρ_H given in Eqs. (F-7) and (F-8), one obtains

$$P_{\text{NNN}} = 0.18 \quad (\text{F-17})$$

This amount of correlation is still sufficiently small that it is a satisfactory approximation to neglect it.

APPENDIX G. DERIVATION OF FISHER INFORMATION MATRIX FOR GENERAL POLYGON

In this appendix the basic derivations necessary for the results of Section 4 are presented.

Since S is constant except near the boundary, the Fisher Information Matrix may be written

$$J_{ij} = \frac{2}{N_0} \sum_{n=1}^N \iint_{R_n} \frac{\partial S(x, y, f)}{\partial f_j} \frac{\partial S(x, y, f)}{\partial f_i} dx dy \quad (G-1)$$

where $\iint_{R_n} \dots$ denotes integration over a narrow strip of width δ surrounding the n th side.

In order to more conveniently perform the integration and express the function $S(x, y, f)$ near the n th side, we translate and rotate to new coordinates U and V (see figure) defined by

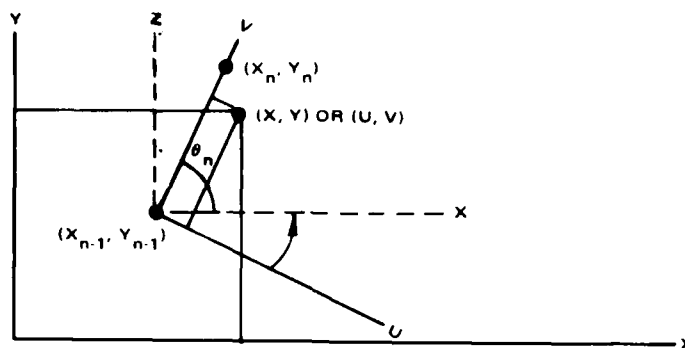
$$x = x_{n-1} + U \sin \theta_n + V \cos \theta_n \quad (G-2a)$$

$$y = y_{n-1} - U \cos \theta_n + V \sin \theta_n \quad (G-2b)$$

or

$$U = (x - x_{n-1}) \sin \theta_n - (y - y_{n-1}) \cos \theta_n \quad (G-3a)$$

$$V = (x - x_{n-1}) \cos \theta_n + (y - y_{n-1}) \sin \theta_n \quad (G-3b)$$



The condition that $S(x, y, \underline{f})$ decreases linearly to zero in the boundary regions is expressed by the equation

$$S(x, y, \underline{f}) = \Delta T \cdot \begin{cases} 1, & U < -\frac{\delta}{2} \\ 0, & U > \frac{\delta}{2} \\ \frac{1}{2} - \frac{U}{\delta}, & |U| \leq \frac{\delta}{2} \end{cases} \quad (G-4)$$

So in terms of x and y (for points in R_n)

$$S(x, y, \underline{f}) = \Delta T \left\{ \frac{1}{2} - \frac{1}{\delta} \left[(x - x_{n-1}) \sin \theta_n - (y - y_{n-1}) \cos \theta_n \right] \right\} \quad (G-5)$$

since

$$f_1 = \Delta T, \quad \frac{\partial S}{\partial f_1} = \frac{1}{2} - \frac{U}{\delta}, \quad (G-6a)$$

while for $i > 1$

$$\begin{aligned} \frac{\partial S}{\partial f_i} &= -\frac{\Delta T}{\delta} \left[-\frac{\partial x_{n-1}}{\partial f_i} \sin \theta_n + \frac{\partial y_{n-1}}{\partial f_i} \cos \theta_n + (x - x_{n-1}) \cos \theta_n \frac{\partial \theta_n}{\partial f_i} + (y - y_{n-1}) \sin \theta_n \frac{\partial \theta_n}{\partial f_i} \right] \\ &= -\frac{\Delta T}{\delta} \left[-\frac{\partial x_{n-1}}{\partial f_i} \sin \theta_n + \frac{\partial y_{n-1}}{\partial f_i} \cos \theta_n + v \frac{\partial \theta_n}{\partial f_i} \right], \end{aligned} \quad (G-6b)$$

where use was made of Eqs. (G-2).

It is straightforward to verify that

$$\frac{\partial \theta_n}{\partial f_i} = \frac{1}{L_n} \left[\cos \theta_n \frac{\partial}{\partial f_i} (y_n - y_{n-1}) - \sin \theta_n \frac{\partial}{\partial f_i} (x_n - x_{n-1}) \right] \quad (G-7a)$$

$$= L_n^{-1} \left[\cos \theta_n \frac{\partial \Delta y_n}{\partial f_i} - \sin \theta_n \frac{\partial \Delta x_n}{\partial f_i} \right] \quad (G-7b)$$

$$= L_n^{-2} \left[\Delta x_n \frac{\partial \Delta y_n}{\partial f_i} - \Delta y_n \frac{\partial \Delta x_n}{\partial f_i} \right] \quad (G-7c)$$

where

$$\Delta x_n \triangleq x_n - x_{n-1} \quad (G-8)$$

$$\Delta y_n \triangleq y_n - y_{n-1} \quad (G-9)$$

$$L_n \triangleq \left[(\Delta x_n)^2 + (\Delta y_n)^2 \right]^{1/2} \quad (G-10)$$

$$\cos \theta_n \triangleq \frac{\Delta x_n}{L_n} \quad (G-11)$$

$$\sin \theta_n \triangleq \frac{\Delta y_n}{L_n} \quad (G-12)$$

Substituting (G-7b) into (G-6), we obtain

$$\frac{\partial S}{\partial f_i} = -\frac{\Delta T}{\delta} \left\{ \begin{array}{l} -\sin \theta_n \left[\left(1 - \frac{V}{L_n}\right) \frac{\partial x_{n-1}}{\partial f_i} + \frac{V}{L_n} \frac{\partial x_n}{\partial f_i} \right] \\ + \cos \theta_n \left[\left(1 - \frac{V}{L_n}\right) \frac{\partial y_{n-1}}{\partial f_i} + \frac{V}{L_n} \frac{\partial y_n}{\partial f_i} \right] \end{array} \right\}$$

The integral in (G-1)

$$\mathcal{J} \triangleq \iint_{R_n} \frac{\partial S(x, y, \underline{f})}{\partial f_i} \frac{\partial S(x, y, \underline{f})}{\partial f_u} dx dy \quad (G-14)$$

can now be evaluated in terms of the U, V variables:

$$\mathcal{J} = \int_{-\delta/2}^{\delta/2} du \int_0^{L_n} dv \frac{\partial S}{\partial f_i} \frac{\partial S}{\partial f_j} \quad (G-15)$$

Substituting (G-13) into (G-15), the integrations are easy to carry out so to obtain

$$\mathcal{J} = \frac{L_n (\Delta T)^2}{3\delta} \left\{ \begin{aligned} & \left[-\sin \theta_n \frac{\partial x_n}{\partial f_i} + \cos \theta_n \frac{\partial y_n}{\partial f_i} \right] \left[-\sin \theta_n \frac{\partial x_n}{\partial f_j} + \cos \theta_n \frac{\partial y_n}{\partial f_j} \right] \\ & + \left[-\sin \theta_n \frac{\partial x_{n-1}}{\partial f_i} + \cos \theta_n \frac{\partial y_n}{\partial f_i} \right] \left[-\sin \theta_n \frac{\partial x_{n-1}}{\partial f_j} + \cos \theta_n \frac{\partial y_{n-1}}{\partial f_j} \right] \\ & + \frac{1}{2} \left[-\sin \theta_n \frac{\partial x_n}{\partial f_i} + \cos \theta_n \frac{\partial y_n}{\partial f_i} \right] \left[-\sin \theta_n \frac{\partial x_{n-1}}{\partial f_j} + \cos \theta_n \frac{\partial y_{n-1}}{\partial f_j} \right] \\ & + \frac{1}{2} \left[-\sin \theta_n \frac{\partial x_{n-1}}{\partial f_i} + \cos \theta_n \frac{\partial y_{n-1}}{\partial f_i} \right] \left[-\sin \theta_n \frac{\partial x_n}{\partial f_j} + \cos \theta_n \frac{\partial y_n}{\partial f_j} \right] \end{aligned} \right\} \quad (G-16)$$

Introducing the midpoint variables \bar{x}_n, \bar{y}_n ,

$$\bar{x}_n = \frac{x_{n-1} + x_n}{2} \quad (G-17)$$

$$\bar{y}_n = \frac{y_{n-1} + y_n}{2} \quad (G-18)$$

the bracketed expression in (G-16) simplifies to

$$\begin{aligned}
 & 3 \left[-\sin \theta_n \frac{\partial \bar{x}_n}{\partial f_i} + \cos \theta_n \frac{\partial \bar{y}_n}{\partial f_i} \right] \left[-\sin \theta_n \frac{\partial \bar{x}_n}{\partial f_j} + \cos \theta_n \frac{\partial \bar{y}_n}{\partial f_j} \right] \\
 & + \frac{1}{4} \left[-\sin \theta_n \frac{\partial \Delta x_n}{\partial f_i} + \cos \theta_n \frac{\partial \Delta y_n}{\partial f_i} \right] \left[-\sin \theta_n \frac{\partial \Delta x_n}{\partial f_j} + \cos \theta_n \frac{\partial \Delta y_n}{\partial f_j} \right]
 \end{aligned} \tag{G-19}$$

Combining (G-19), (G-16), (G-15), (G-14), (G-7b) and (G-1) we obtain

$$\begin{aligned}
 J_{ij} = & \frac{2(\Delta T)^2}{N\sigma} \sum_{n=1}^N \\
 & \cdot L_n \left\{ \left[-\sin \theta_n \frac{\partial \bar{x}_n}{\partial f_i} + \cos \theta_n \frac{\partial \bar{y}_n}{\partial f_i} \right] \left[-\sin \theta_n \frac{\partial \bar{x}_n}{\partial f_j} + \cos \theta_n \frac{\partial \bar{y}_n}{\partial f_j} \right] \right. \\
 & \left. + \frac{L_n^2}{12} \frac{\partial \theta_n}{\partial f_i} \frac{\partial \theta_n}{\partial f_j} \right\}
 \end{aligned} \tag{G-20}$$

The quantities J_{lj} are similarly obtained using (G-6a) and (G-13) in (G-15), to obtain

$$J_{lj} = -\frac{\Delta T}{N\sigma} \sum_{n=1}^N L_n \left(-\frac{\partial x_{n-1}}{\partial f_j} \sin \theta_n + \frac{\partial y_{n-1}}{\partial f_j} \cos \theta_n \right) + \frac{L_n^2}{2} \frac{\partial \theta_n}{\partial f_j} \tag{G-21a}$$

$$= -\frac{\Delta T}{N\sigma} \sum_{n=1}^N L_n \left[-\sin \theta_n \frac{\partial \bar{x}_n}{\partial f_j} + \cos \theta_n \frac{\partial \bar{y}_n}{\partial f_j} \right] \tag{G-21b}$$

$$= -\frac{\Delta T}{N\sigma} \sum_{n=1}^N \left[\Delta x_n \frac{\partial \bar{y}_n}{\partial f_j} - \Delta y_n \frac{\partial \bar{x}_n}{\partial f_j} \right] \tag{G-21c}$$

The quantity J_{11} is obtained directly from the original Fisher integral since $\partial S / \partial \Delta T = 1$ over most of the interior. Thus, to a good approximation, $J_{11} = 2/N_o \cdot (\text{area enclosed by boundary})$. (G-22)

APPENDIX H. EFFECT OF CLUTTER ON TARGET SEGMENTATION PROBABILITY OF ANOMALY

In this appendix, the bounds on probability of anomaly, i.e., the probability that a target segmentor will segment a candidate object nowhere near an actual target, will be derived for the case where there is a single clutter object in the scene. This extends results previously obtained in (1) for rectangular targets imbedded in white noise. The performance bounds on probability of anomaly will be derived for three cases. The first case has a target and a clutter object in the field of view, and the segmentor has been optimized as if it were a known shape clutter object in the scene, but the size and location is unknown. In the second case, the bounds will be computed where there is a target and clutter object in the field of view, but the segmentor is not optimized for the clutter, i.e., no clutter is assumed when the optimum segmentor is derived. The third case is the reverse of the second case where there is no clutter, but the target segmentor is optimized as if there were.

The first model is governed by the equation

$$I(x, y) = T_T S(x, y, \underline{F}_s) + T_c \left(1 - S(x, y, \underline{F}_s) \right) C(x, y, \underline{F}_c) + n(x, y) \quad (H-1)$$

where

- $I(x, y)$ is the observed intensity distribution
- T_T is the target's d.c. intensity offset
- T_c is the clutter object's d.c. intensity offset
- \underline{F}_s is a feature vector which specifies the size and location of the target

- \underline{F}_c is a feature vector which specifies the size and location of the clutter object
- $S(x, y, \underline{F}_s) = \begin{cases} 1 & \text{if } x, y \text{ is on the target} \\ 0 & \text{otherwise} \end{cases}$
- $C(x, y, \underline{F}_c) = \begin{cases} 1 & \text{if } x, y \text{ is on the clutter object} \\ 0 & \text{otherwise} \end{cases}$
- $n(x, y)$ is a zero-mean Gaussian process with autocovariance $N_0/2\delta(\tau_x, \tau_y)$.

The shape of the target and the clutter object are assumed known, but the size, location, and d.c., intensity offset is assumed unknown.

With these assumptions the optimal target segmentation will be obtained by the method of maximum likelihood. The log-likelihood of the observed intensity distribution is

$$\begin{aligned} \Lambda(T_s, T_c, \underline{f}_s, \underline{f}_c) = & \frac{2}{N_0} \iint S(x, y, \underline{f}_s) T_s \left(I(x, y) - \frac{T_s}{2} \right) dx dy \\ & + \frac{2}{N_0} \iint \left(1 - S(x, y, \underline{f}_s) \right) C(x, y, \underline{f}_c) \\ & \cdot T_c \left(I(x, y) - \frac{T_c}{2} \right) dx dy \end{aligned} \quad (H-2)$$

The values of T_s , T_c , \underline{f}_s and \underline{f}_c that maximize this function are the estimated parameters. Noting that the maximum likelihood estimates of T_s and T_c are

$$\hat{T}_s = \frac{\iint S(x, y, \underline{f}_s) I(x, y) dx dy}{\iint S(x, y, \underline{f}_s) dx dy} \quad (H-3a)$$

and

$$\hat{T}_C = \frac{\iint (1 - S(x, y, \underline{f}_s)) C(x, y, \underline{f}_c) I(x, y) dx dy}{\iint (1 - S(x, y, \underline{f}_s)) C(x, y, \underline{f}_c) dx dy} \quad (H-3b)$$

the result is

$$\Lambda = \Lambda(\hat{T}_S, \hat{T}_C, \underline{f}_s, \underline{f}_c) = \Lambda_1^2 + \Lambda_2^2 \quad (H-4a)$$

where

$$\Lambda_1^2 = \frac{2}{N_0} \frac{\left(\iint I(x, y) S(x, y, \underline{f}_s) dx dy \right)^2}{\iint S(x, y, \underline{f}_s) dx dy} \quad (H-4b)$$

and

$$\Lambda_2^2 = \frac{2}{N_0} \frac{\left(\iint (1 - S(x, y, \underline{f}_s)) C(x, y, \underline{f}_c) I(x, y) dx dy \right)^2}{\iint (1 - S(x, y, \underline{f}_s)) C(x, y, \underline{f}_c) dx dy} \quad (H-4c)$$

In order to compute probability of anomaly it should be noted that Λ_1 and Λ_2 have the following properties:

1. Λ_1 and Λ_2 are statistically independent

$$2. \quad E(\Lambda_1) = \sqrt{\frac{2}{N_0}} \frac{\left(T_T \iint S_T S + T_c \iint (1 - S_T) C_T S \right)}{\sqrt{\iint S}}$$

$$3. E(\Lambda_2) = \sqrt{\frac{2}{N_0}} \frac{\left(T_T \iint (1 - S) C S_T + T_c \iint (1 - S) C (1 - S_T) C_T \right)}{\sqrt{\iint (1 - S) C}}$$

$$4. \text{Var } \Lambda_1 = 1, \text{Var } \Lambda_2 = 1$$

$$5. \Lambda_1 \text{ and } \Lambda_2 \text{ are Gaussian random variables.}$$

(The notation S_T and C_T is used above to denote the functions $S(x, y, \underline{F}_s)$ and $C(x, y, \underline{F}_c)$ when \underline{F}_s and \underline{F}_c are equal to the target's and clutter's true feature vector values, and the notation S and C is used to denote the functions $S(x, y, \underline{F}_s)$ and $C(x, y, \underline{F}_c)$ with \underline{F}_s and \underline{F}_c equal to the hypothesized values of target's and clutter's feature vectors. This notation will be used throughout this appendix. All integrations are performed over the image plane.)

Using the five properties of Λ_1 and Λ_2 given above and a well known relationship between the sum of squares of Gaussian random variables, the probability distribution of $\Lambda = \Lambda_1^2 + \Lambda_2^2$ can be determined. This relationship will be stated in theorem form. Theorem: Let x_i , $i = 1, 2, 3, \dots, N$ be independent Gaussian random variables with zero mean and variance equal to 1. Then

$$Q = \sum_{i=1}^N x_i^2.$$

is a random variable having the non-central chi-square distribution, $\chi(N, \alpha)$, with N degrees of freedom and non-centrality parameter

$$\alpha = \sum_{i=1}^N \mu_i^2.$$

The cumulative distribution function (c.d.f.) of the non-central chi-square with N degrees of freedom is given by

$$P(Q \leq t) = F_{N,\alpha}(t) = \sum_{j=0}^{\infty} e^{-\alpha/2} \frac{(\alpha/t)^j}{j!} F_{N+2j,0}(t)$$

where

$$F_{N,0}(t) = \left[2^{N/2} \Gamma(N/2) \right]^{-1} \int_0^t y^{\frac{N}{2}-1} e^{-y/2} dy$$

is the c.d.f. of the central chi-square random variable.

Using the five properties of Λ_1 , and Λ_2 and the theorem that has been just stated, it is seen that

$$\Lambda = \Lambda_1^2 + \Lambda_2^2$$

has a non-central chi-square distribution with two degrees of freedom and non-centrality parameter

$$\alpha = \frac{2}{N_0} \left[\frac{\left(T_T \iint (1-S) C S_T + T_c \iint (1-S) C (1-S_T) C_T \right)^2}{\iint (1-S) C} + \frac{\left(T_T \iint S_T S + T_c \iint (1-S_T) C_T S \right)^2}{\iint S} \right] \quad (H-5)$$

For $S = S_T$ and $C = C_T$, i.e., the hypothesized target and clutter feature vectors values are equal to the true target and clutter feature vectors values,

$$\alpha = \frac{2}{N_0} \left[T_c^2 \iint (1 - S_T) C_T + T_T^2 \iint S_T \right] \quad (H-6)$$

As done in reference 1, we will define the "anomaly threshold" as

$$\lambda = E \left(\Lambda \mid S = S_T, C = C_T \right) \quad (H-7)$$

and so

$$\begin{aligned} \lambda &= E \left(\chi^2(2, \alpha) \right) = 2 + \alpha \\ &= 2 \left[1 + \frac{1}{N_0} \left(T_c^2 \iint (1 - S_T) C_T + T_T^2 \iint S_T \right) \right] \end{aligned}$$

By definition, an anomaly has occurred if $\Lambda > \lambda$ for $\iint SS_T = 0$, that is, an anomaly has occurred if $\Lambda > \lambda$ for a hypothesized target region which does not intersect the true target region. To compute the probability of this occurrence, we return to H-5 and note that for $\iint SS_T = 0$

$$\alpha = \frac{2}{N_0} \left[\frac{\left(T_T \iint CS_T + T_c \iint (1 - S_T) C_T C - T_c \iint SCC_T \right)^2}{\iint (1 - S) C} + T_c^2 \frac{\left(\iint C_T S \right)^2}{\iint S} \right] \quad (H-8)$$

If it is further assumed that the clutter is not masked by the target and that this information is available to the target/clutter detector, then:

$$\iint S_T C_T = \iint SC = 0.$$

Hence, Eq. (H-8) reduces to

$$\alpha = \frac{2}{N_o} \left[\frac{\left(T_T \iint CS_T + T_c \iint C_T C \right)^2}{\iint C} + T_c^2 \frac{\left(\iint C_T S \right)^2}{\iint S} \right] \quad (H-9)$$

There are five cases that the hypothesized target and clutter feature vectors, \underline{f}_s and \underline{f}_c , will be considered to be in that may result in an anomaly. Case (1) is defined such that the hypothesized target and clutter regions are contained in the region which contains only noise. That is, for case (1)

$$\iint SS_T = \iint SC_T = \iint S_T C = \iint CC_T = 0.$$

For any $\underline{f}_s, \underline{f}_c$ in case (1) $\alpha = \alpha_1 = 0$. Hence the probability of an anomaly for a fixed $\underline{f}_s, \underline{f}_c$ in case (1) is given by

$$P\left(\chi^2(2, 0) \geq \lambda\right)$$

For all hypothesized target regions of area $A(S)$ and hypothesized clutter regions of area $A(C)$ the probability of anomaly due to region (1) can be approximated by

$$\left(1 - F_{2, 0}(\lambda)\right) \left(\frac{R^2}{A(S) + A(C)} \right) \quad (H-15)$$

where the scene is assumed to have dimension, $R \times R$.

A bound on probability of anomaly for all sizes of hypothesized target and clutter regions can be obtained by applying the argument following Theorem 1 in reference [1]. The probability of anomaly due to region (1) is then seen to be bounded by

$$\sum_{K=0}^{\infty} \frac{R^2}{2^K (A(S_{\min}) + A(C_{\min}))} \left(1 - F_{2,0}(\lambda)\right) \quad (\text{H-16})$$

or, equivalently,

$$\frac{2R^2}{A(S_{\min}) + A(C_{\min})} \left(1 - F_{2,0}(\lambda)\right) \quad (\text{H-17})$$

where $A(S_{\min})$ and $A(C_{\min})$ are the smallest hypothesized target and clutter areas allowed.

Case (2) is defined such that the hypothesized target region does not intersect the true clutter region and that the hypothesized clutter region is contained in the true clutter region. For \underline{f}_s and \underline{f}_c in case (2) Eq. (H-9) reduces to

$$\alpha = \alpha_2 = \frac{2}{N_0} \left[\frac{\left(T_c \iint C_T C \right)^2}{\iint C} \right] \quad (\text{H-18})$$

where $C \leq C_T$. We will assume that if an anomaly occurs in region (2) it will be due to some $C \leq C_T$ such that

$$\frac{\left(\iint C C_T \right)^2}{\iint C}$$

is maximum.

and so

$$\alpha_2 = \frac{2}{N_o} T_c^2 \iint_{C_T} C_T \quad (H-19)$$

Since there is only one way to choose $0 \leq C \leq C_T$, such that

$$\frac{\left(\iint_{C_T} C \right)^2}{\iint_C C}$$

is maximum, the probability of anomaly due to region (2) is approximated by

$$1 \cdot P \left(\chi^2(2, \alpha_2) \geq \lambda \right) = \left(1 - F_{2, \alpha_2}(\lambda) \right) \cdot 1 \quad (H-20)$$

where

$$\alpha_2 = \frac{2}{N_o} \cdot T_c^2 \iint_{C_T} C_T$$

Case (3) is defined such that the hypothesized clutter region is contained in the true target region and the hypothesize target region is contained in the region which contains only noise. From Eq. (H-9),

$$\alpha = \alpha_3 = \frac{2}{N_o} \left[\frac{T_T^2 \left(\iint_{C_S} C_S \right)^2}{\iint_C C} \right]$$

where $0 \leq C \leq S_T$. Then for fixed $\underline{f}_s, \underline{f}_c$ in region (3) the probability of anomaly is given by

$$1 - F_{2, \alpha_2}(\lambda)$$

Assume that if an anomaly occurs in region (3) it is due to some $C \leq S_T$ such that

$$\frac{\left(\iint_{CS_T} \right)^2}{\iint_C} \quad (H-22)$$

is maximum.

Using the notation C_* to denote a C such that (H-22) is maximum, the probability of anomaly due to some $\underline{f}_s, \underline{f}_c$ in region (3) is approximated by

$$N_3 \cdot \left(1 - F_{2, \alpha_3}(\lambda) \right) \quad (H-23)$$

where

$$N_3 = \frac{\iint S_T}{\iint C_*}$$

and

$$\alpha_3 = \frac{2}{N_0} \frac{\left[T_T^2 \left(\iint C_* S_T \right)^2 \right]}{\iint C_*}$$

Case (4) is defined such that the hypothesized target region is contained in the true clutter region and the hypothesized clutter region is contained in the region which contains only noise. For Eq. (H-9),

$$\alpha = \alpha_4 = \frac{2}{N_0} \left[\frac{T_c^2 \left(\iiint C_T S \right)^2}{\iiint S} \right]$$

where $0 \leq S \leq C_T$. Then for any fixed f_s, f_c in case (4) the probability of anomaly is given by

$$1 - F_{2, \alpha_4}(\lambda)$$

where

$$\alpha_4 = \frac{2}{N_0} \left[\frac{T_c^2 \left(\iiint C_T S \right)^2}{\iiint S} \right]$$

$S \leq C_T$. Assuming that if an anomaly occurs due to region (4) is due to some $S \leq C_T$ such that

$$\frac{\left(\iiint C_T S \right)^2}{\iiint S}$$

is maximum, approximation of the probability of anomaly due to region (4) is given by

$$\left(1 - F_{2, \alpha_4}(\lambda)\right) \quad (\text{H-24})$$

where

$$\alpha_4 = \frac{2}{N_o} \frac{\left(\iiint C_T S_*\right)^2 T_c^2}{\iint S_*}$$

and

$$N_4 = \frac{\left(\iint C_T\right)}{\left(\iint S_*\right)}.$$

Case (5) is defined such that the hypothesized clutter region is contained in the true target region and the hypothesized target region is contained in the true clutter region. For fixed \underline{f}_s , \underline{f}_c in case (5) the probability of anomaly is given by

$$1 - F_{2, \alpha_5}(\lambda)$$

where

$$\alpha_5 = \frac{2}{N_o} \frac{\left[T_T \iint C S_T\right]^2}{\iint C} + T_c^2 \frac{\left(\iint C_T S\right)^2}{\iint S}$$

Using the results from cases (3) and (4), the approximate probability of anomaly due to case (5) is given by

$$\max(N_3, N_4) \cdot \left(1 - F_{2, \alpha_2 + \alpha_3}(\lambda)\right) \quad (\text{H-25})$$

Combining equations (H-17), (H-20), (H-23), (H-24) and (H-25) the bound on probability of anomaly is seen to be

$$\begin{aligned} P(\text{anomaly}) \leq & \left(\frac{2 R^2}{A(S_{\min}) + A(C_{\min})} \right) \left(1 - F_{2, 0}(\lambda)\right) \\ & + \left(1 - F_{2, \alpha_2}(\lambda)\right) + N_3 \left(1 - F_{2, \alpha_3}(\lambda)\right) \\ & + N_4 \left(1 - F_{2, \alpha_4}(\lambda)\right) + \left(1 - F_{2, \alpha_3 + \alpha_4}(\lambda)\right) \end{aligned} \quad (\text{H-26})$$

where

$$a_2 = \frac{2}{N_0} T_c^2 \iint C_T = 2 \cdot \text{CNR}^2 \cdot \iint C_T$$

CNR is the "clutter to noise ratio"

$$\alpha_3 = \frac{\frac{2}{N_0} \left[T_T^2 \left(\iint C_* S_T \right)^2 \right]}{\iint C_*}$$

$$= 2 \cdot \text{SNR}^2 \cdot \frac{\left(\iint C_* S_T \right)^2}{\iint C_*}$$

SNR is the "signal to noise ratio"

$$N_3 = \frac{\iint S_T}{\iint C_*}$$

$$\alpha_4 = \frac{2}{N_o} T_c^2 \frac{\left(\iint C_T S_* \right)^2}{\iint S_*} = 2 \cdot \text{CNR}^2 \cdot \frac{\iint C_T S_*}{\iint S_*}$$

$$N_4 = \frac{\iint C_T}{\iint S_*}$$

Now consider the case where there is a target and a clutter object and the segmentator has been optimized for only a target. The likelihood for this case is

$$\Lambda = \frac{\left(\iiint I(x, y) S(x, y) \, dx dy \right)^2}{\iint S(x, y) \, dx dy} \quad (\text{H-26b})$$

From Eq. (H-26) the "anomaly threshold" is seen to be

$$\lambda = \epsilon(\Lambda | S = S_T) = \frac{N_o}{2} + T_T^2 \iint S_T$$

There are two ways that an anomaly can occur. The target detector could lock onto noise, or the target detector can lock on to the clutter object. The probability that the target detector locks onto noise is obtained directly from reference 1:

$$\begin{aligned} \text{P(anomaly due to target)} \\ \text{detector locking onto} \\ \text{noise} &\leq \frac{4 R^2}{A(S_{\min})} \operatorname{erfc}_* \left(\sqrt{\frac{2}{N_o}} \right) \\ &= \frac{4 R^2}{A(S_{\min})} \operatorname{erfc}_* \left(\sqrt{2 \cdot \text{SNR}^2 \cdot A(S_T) +} \right) \end{aligned}$$

The probability that the target detector locks onto the clutter object can be approximated by

$$\begin{aligned} \left[\frac{\iint C_T}{\iint S_*} \right] P(\Lambda > \lambda | S = S_*) &= \left[\frac{\iint C_T}{\iint S_*} \right] \\ &\cdot \left(1 - \operatorname{erfc}_* \left(-\text{SNR}^2 - \frac{1}{2A(S_*)} - 2\text{CNR}^2 \right) \right. \\ &\quad \left. + \operatorname{erfc}_* \left(\text{SNR}^2 + \frac{1}{2A(S_*)} - 2\text{CNR}^2 \right) \right) \end{aligned}$$

Then probability of anomaly is

$$\frac{4 R^2}{A(S_{\min})} \operatorname{erfc}_* \left(\sqrt{2 \cdot \operatorname{SNR}^2 \cdot A(S_T) + 1} \right) + \left[\frac{\iint C_T}{\iint S_*} \right] P(\Lambda > \lambda \mid S = S_*)$$

(H-27)

Now consider the case where the segmentor has been optimized for a target and a clutter object, when there is no clutter. Probability of anomaly for this case can be approximated by setting $T_c = 0$, $C_T = 0$ in Eq. (H-26). The probability of anomaly is then seen to be

$$\begin{aligned} & \left(\frac{2 R^2}{A(S_{\min}) + A(C_{\min})} \right) (1 - F_{2,0}(\lambda)) + (1 - F_{2,0}(\lambda)) \\ & + N_3 (1 - F_{2,\alpha_3}(\lambda)) + N_4 (1 - F_{2,0}(\lambda)) \\ & + \max(N_3, N_4) (1 - F_{2,\alpha_3}(\lambda)) \end{aligned}$$

where

$$\begin{aligned} \lambda &= 2 \left(1 + \frac{T_T^2}{N_o} \iint S_T \right), \\ \alpha_3 &= 2 \cdot \operatorname{SNR}^2 \frac{\iint C_* S_T}{\iint C_*}, \\ N_3 &= \frac{\iint S_T}{\iint C_*}, \quad N_4 = \frac{\iint C_T}{\iint S_*}. \end{aligned}$$

REFERENCES

1. Rubin, L. M., Frey, R. L., "New Approach to FLIR Segmentation", Image Understanding Systems II, SPIE Volume 205, 1979. (Enclosed as Appendix A.)
2. H. L. Van Trees, Detection, Estimation, and Modulation Theory, Part I, 1968, John Wiley & Sons.
H. L. Van Trees, Detection, Estimation, and Modulation Theory, Part III, 1971, John Wiley & Sons.

DATE
FILMED
-8